A measurement of E-mode polarisation spectrum of the cosmic microwave background with the POLARBEAR experiment

by

Anh Thi Phuong Pham

ORCID: 0000-0001-9396-8915

Doctor of Philosophy

July 2020

in the

School of Physics

THE UNIVERSITY OF MELBOURNE

This thesis submitted in partial fulfillment for the degree of Doctor of Philosophy

THE UNIVERSITY OF MELBOURNE

Abstract

School of Physics

Doctor of Philosophy

by Anh Thi Phuong Pham
ORCID: 0000-0001-9396-8915

The cosmic microwave background (CMB) stands as one of the most interesting subjects of astronomical surveys. The CMB light carries information about the history and the origin of the universe. Polarisation of the CMB can be decomposed and transformed in to E-mode and B-mode polarisation.

My thesis focuses on the measurement of E-mode polarisation power spectrum of the cosmic microwave background using 150 Ghz data taken from July 2014 to December 2016 with the POLARBEAR experiment. POLARBEAR is an on-going cosmic microwave background experiment that began taking data in 2012. The target area of observation for the data in this thesis is a large patch of sky of over 600 deg^2. A continuously rotating half wave plate was installed in the POLARBEAR telescope and heavily influences the overall data analysis.

This thesis is outlined as followed. Chapter 1 reviews the standard model of cosmology, and explain the physics of the CMB and CMB polarisation. Chapter 2 describes the POLARBEAR experiment. Chapter 3 gives a brief review of the continuously rotating half wave plate and its impacts on recorded data. Chapter 4 describes the calibration of the recorded data. Chapter 5 describes the pipeline to process the recorded data. Chapter 6 details on the validation of the established power spectrum pipeline, the data selected following Chapter 5, and the estimation of systematics in POLARBEAR data. Chapter 7 details on the E-mode power spectrum estimated from the selected data. I use the measured E-mode power spectrum in combination with other data sets: Planck 2018, ACTPol, SPT-SZ, and BAO data to constrain cosmological parameters. The combined data set is consistent with the standard Lambda Cold Dark Matter model of cosmology. I also consider extensions to the standard model, and present improved constraints on these extensions. Chapter 8 summaries preceding chapters and gives an outlook on the Simons Array, the successor of the POLARBEAR experiment.

Declaration of Authorship

I, Anh Thi Phuong Pham, declare that this thesis titled, 'A measurement of E-mode polarisation spectrum of the cosmic microwave background with the POLARBEAR experiment' and the work presented in it are my own. I confirm that:

- This work was done wholly or mainly while in candidature for a research degree at this University.
- Where any part of this thesis has previously been submitted for a degree or any other qualification at this University or any other institution, this has been clearly stated.
- Where I have consulted the published work of others, this is always clearly attributed.
- Where I have quoted from the work of others, the source is always given. With the exception of such quotations, this thesis is entirely my own work.
- I have acknowledged all main sources of help.
- Where the thesis is based on work done by myself jointly with others, I have made clear exactly what was done by others and what I have contributed myself.
- The number of words is under the limit of 100000 words for a thesis submitted as a requirement of Doctor of Philosophy degree.

Signed: Anh T. P. Pham

Date:Feb/12/2020

*"Leck mich im a***"*

Wolfgang Amadeus Mozart

Acknowledgements

This thesis could not have been done without people I have met at my university and on my CMB journey. I owe my previous supervisor, Chris Chantler, a big thanks for picking me to Melbourne, and later accepting my request to change my supervisor. Thanks to Joni for her suggestion on reconsidering my true interest for a PhD. Of course, I cannot forget to thank my supervisor, Christian Reichardt, for his acceptance to supervise me, his super patience while guiding me, and his low-key supporting my other endeavors.

Thanks to the PIs, Adrian, Kam Arnold, Brian Keating, and Masashi Hazumi, for letting me join the POLARBEAR experiment. Neil was like my earliest mentor when I just began the analysis tasks. His suggestions have been useful along my journey. Thanks to Satoru for putting understandable contents on wiki and in the Analysis Backend. Thanks to Federico for his explanation of lensing, which I tend to forget without him, and other other stuffs. Thanks to Yuji and Akito for having been checking and suggesting tasks that I can do to improve. Thanks to Kolen for being in charge of the null tests early on. I learn a few things about coding from you and quite like your persistence actually. Thanks to Dominic for being there. Thanks to David, Tucker, Greg for taking up the calibration tasks with me. A big thanks to all people who have been working on the data collection and maintenance or hardware of the telescope: Dave Boettger, Darcy Barron, Praween Siritanasak, and many more that I apologise for not remembering/ knowing.

Back in Melbourne, my PhD committee chairs, Martin Sevior and Michele Trenti, have been important in helping me to keep my pace. Many thanks to my school mates for the occasional fun: Sanjay, Suk Yee, Maddie, and many more.

Thanks to my parents for somehow preparing me to be headstrong enough for this journey.

Contents

List of Tables

List of Figures

Abbreviations

CMB	**C**osmic **M**icrowave **B**ackground
CES	**C**onstant **E**levation **S**can
CRHWP	**C**ontinuously **R**otating **H**alf **W**ave **P**late
HWP	**H**alf **W**ave **P**late
PSD	**P**ower **S**pectral **D**ensity
TOD	**T**ime-**O**rdered **D**ata

Physical Constants

Speed of Light $c = 2.997\ 924\ 58 \times 10^8\ \mathrm{ms}^{-\mathrm{S}}$ (exact)

Symbols

a	distance	m
P	power	W (Js^{-1})
ω	angular frequency	$rads^{-1}$

To my parents, and my old men . . .

Chapter 1

Introduction

The development of the general theory of relativity [18] coupled with the discovery that the universe is expanding has shifted our intuitions about cosmology from a static eternal universe to an expanding one of finite age. Observational works further tested physical theories about the history and structure of the universe. By the end of the twentieth century, observations had driven the development of the Lambda-Cold Dark Matter ΛCDM model, which is now regarded as the standard model of cosmology. In the last two decades, ΛCDM model has survived increasingly strenuous observational tests employing a variety of measurement techniques and covering a range of cosmic distance scales. Measurements of the cosmic microwave background (CMB) are prominent among the tests of ΛCDM. To see how the CMB experiments play their roles, the foundation of cosmology is first revisited.

1.1 Pillars of the Standard Model

The Standard Model of Cosmology is the best fitting parametrisation of the Hot Big Bang model. The Hot Big Bang model states that our Universe started from a hot dense state around 14 billion years ago and has been expanding ever since. One pillar of the Standard model is the Cosmological Principle: the universe is the same everywhere (homogeneous) and isotropic on large scales (for a comoving observer), which is to say that there is no preferred position or direction in the Universe. This hypothesis is supported by astronomical observations.

In a homogeneous, expanding universe, the frame of the Universe is expanding. The coordinates of this frame are fixed (constant) and are said to be comoving. The physical distance d_{phys} evolves with time and relates to the comoving distance $d_{comoving}$ via

Hubble-Lemaître law:

$$d_{phys} = a(t)d_{comoving} \tag{1.1}$$

Here, $a(t)$ is the scale factor which is 1 today and was smaller in earlier times. The time t is the cosmic time, or the proper time of comoving observers.

The first work supporting an expanding Universe is Edwin Hubble's study of Cepheid variables [1]. The study finds that galaxies seem to be driving back away from us in all directions of observation, at a rate ($\sim v$) proportional to their distance ($\sim r$).

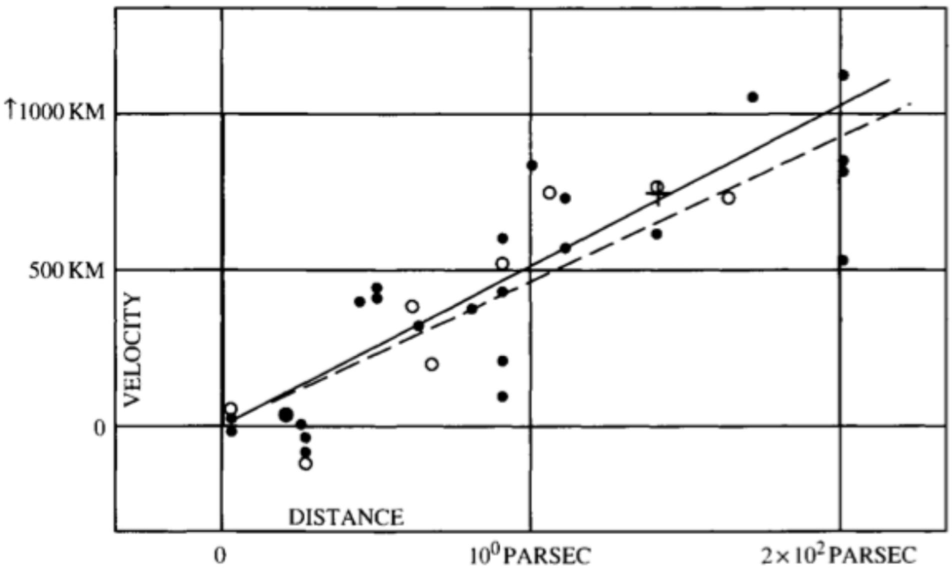

FIGURE 1.1: Velocity-Distance Relation among Extra-Galactic Nebulae. [Picture from [1]]. Open dots correspond to original measurements and are best fitted with dashed line. Filled dots correspond to original measurements corrected for the sun's motion and are best fitted with the solid line.

In honor of Hubble, we still call the rate of expansion of the Universe the Hubble constant. Of course, the expansion rate changes with time (or redshift), and can be expressed in terms of the scale factor as:

$$H(t) \equiv \frac{1}{a}\frac{da}{dt}$$

The Hubble time and Hubble radius, also called horizon, are defined as: $H(t)^{-1}$ and $cH(t)^{-1}$., where c denotes the speed of light. While not exact, these quantities are approximately related to the age of the Universe and the size of the observable horizon. Light has not had enough time at time t to cross distances larger than the horizon, and thus larger scales are not causally connected.

Of course, the Universe's expansion also affects photons as they travel, stretching their wavelength. This effect is known as redshift, and the redshift z can be written as the ratio of the observed to emitted wavelength:

$$1 + z \equiv \frac{\lambda_{observed}}{\lambda_{emitted}} \tag{1.2}$$

where λ is the wavelength. The standard Doppler formula relates low redshifts to small recession velocity v via $z \simeq v/c$. One of the result of redshift is that the CMB shows up at much longer wavelengths than the ultraviolet which one might naively expect from the CMB hydrogen recombination energy, which we will return later in Section 1.3.

Back to the Universe in the Standard Model, Figure 1.2 illustrates the implementation of cosmological principle concerning the isotropy of the Universe on the scales of redshift. Higher redshifts correspond to further distances away from us. On small scales, the Universe is clumpy, but on larger scales, $\geq 10Mpc$, the Universe is homogeneous as the distribution of galaxies appears more uniform.

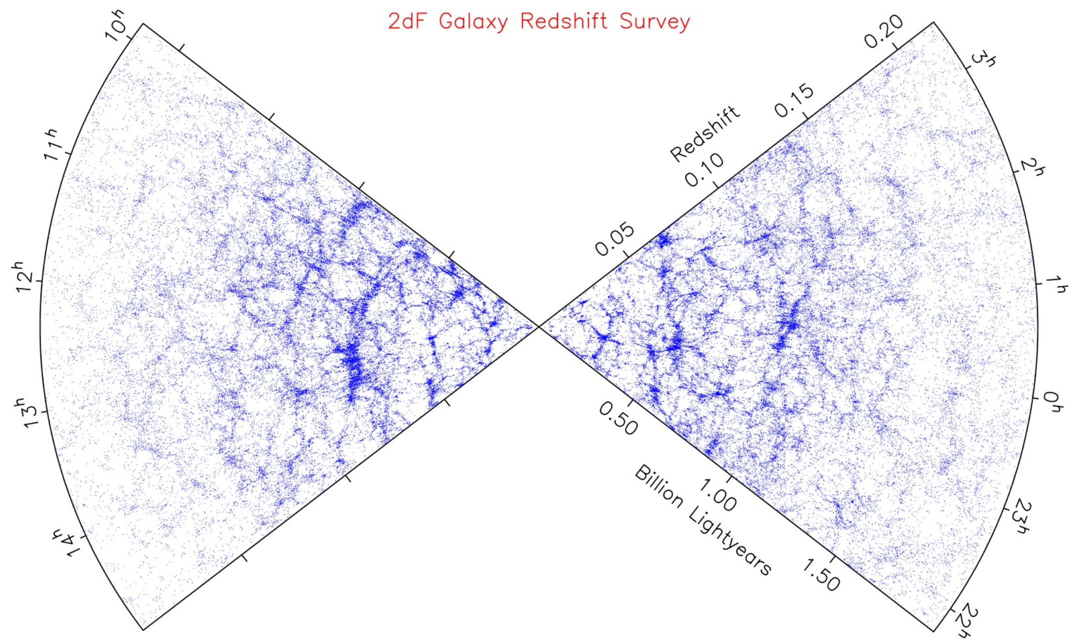

FIGURE 1.2: The distribution of galaxies is clumpy on small scales, but becomes more uniform on large scales and early times. [Picture credit: The 2dF Galaxy Redshift Survey team [2]]

To understand the expansion of the Universe, we turn to Einsteins theory of General Relativity that describes the relation between the geometry of space-time and matter [18].

1.2 General Relativity

General Relativity is the theory published by Einstein in 1915 that describes the relation between geometry and gravitation. While General Relativity has several far-reaching implications in astrophysics, we will only visit its two main culminations: the General Covariance and Einstein's field equations. The metric and equations thus-derived for a homogeneous expanding Universe will also be presented.

1.2.1 The General Covariance and metric

Let us be reminded that the key idea behind General Relativity is the **Equivalence Principle**, which asserts the equivalence of gravitational and inertial mass. This means that when no external forces affect an object, the trajectory of said object follows a geodesic, the shortest path between 2 points in space. In curved space-time or non-uniform gravitational field, we can consider a small region of space-time where the field difference is approximately canceled out. The Equivalence Principle can then be stated as: For every point P in an arbitrary gravitational field in space-time, it is possible to choose a locally inertial coordinate system such that, within a sufficient small region of P, the laws of nature take the same form as they would in the absence of gravitation.

The second behind General Relativity is General Covariance: the idea that the physical laws can be written in a form invariant under coordinate transformations. Tensor fields are normally used for this purpose. In cosmology, we tend to focus on the most fundamental tensor: the metric describing the distance between two points. Recall that the scale factor relates the coordinate distance to the physical distance, so relating the metrics in different models to observations is important to quantify predictions in an expanding Universe. At a point P in space-time, we can derive the metric considering the path between P and an infinitesimally close point Q in a set of coordinates x^μ:

$$p \equiv x^\mu; Q \equiv x^\mu + dx^\mu.$$

Taking in the Equivalence Principle, we can find a locally inertial frame $\xi^\mu(x)$ in P such that:

$$\begin{cases} x^\mu \mapsto \xi^\mu(x) \\ x^\mu + dx^\mu \mapsto \xi^\mu(x+dx) = \xi^\mu(x) + \partial_\alpha \xi^\mu dx^\alpha \end{cases}$$

on notating $\partial_\alpha \equiv \partial/\partial x^\alpha$. The infinitestimal distance between P and Q is

$$d\xi^\mu \equiv \xi^\mu(x+dx) - \xi^\mu(x) = dx^\alpha \partial_\alpha \xi^\mu$$

We can apply Special Relativity in $\xi^\mu(x)$ coordinate frame to get distance between P and Q defined by the line element:

$$ds^2 = d\xi^\alpha d\xi^\beta \eta_{\alpha\beta}.$$

where $\eta_{\alpha\beta} = diag(-1; 1; 1; 1)$ is the Minkowski metric. Returning to the coordinates x^μ, the distance takes the final form:

$$ds^2 = dx^\mu \partial_\mu \xi^\alpha dx^\nu \partial_\nu \xi^\beta \eta_{\alpha\beta} = dx^\mu dx^\nu g_{\mu\nu}(x),$$

with $g_{\mu\nu}(x) = \partial_\mu \xi^\alpha \partial_\nu \xi^\beta \eta_{\alpha\beta}$, the metric in x. Symmetric in its 2 indices, $g_{\mu\nu}$ comes with its inverse $g^{\mu\nu}$ satisfying $g_{\mu\alpha} g^{\alpha\nu} = \delta^\mu_\nu$ and does not depend on the chosen locally inertial frame.

1.2.2 Friedmann-Lemaître-Robertson-Walker (FLRW) metric

The metric for the Universe we live in can be derived from its most important properties: homogeneous distribution of energy (and thus space) and isotropy on large scales. It is known as the Friedmann-Lemaître-Robertson-Walker (FLRW) metric:

$$ds^2 = -dt^2 + a^2(t) \frac{dx^2 + dy^2 + dz^2}{[1 + \frac{\kappa}{4a^2(t)}(x^2 + y^2 + z^2)]^2} \tag{1.3}$$

Here, t is the proper time of an observer comoving with the Universe expansion, (x, y, z) are comoving coordinates, $a(t)$ is the scale factor. The increment $-dt^2$ is basically $-c^2 dt^2$ where the natural unit $c = 1$ is adopted from here and onward. The parameter κ is set by the spatial curvature of the Universe:

$\kappa = 1$ for a closed universe

$\kappa = -1$ for an open universe

$\kappa = 0$ for a flat universe

As a set of comoving coordinates, (x, y, x) have units of length. This means the scale factor $a(t)$ is dimension-less, and so is κ. .

1.2.3 Einstein Equations

General Relativity makes concrete predictions for the local structure of space-time by between the spatial curvature and energy (density) denoted by ρ of the species that fill the Universe. The energy parts, relativistic and non-relativistic, are wrapped in the

Energy-Momentum Tensor $T^{\mu\nu}$. Consider the total action $I[\phi, g]$

$$I[\phi, g] = I_M[\phi, g] + I_{E.H}[g],$$

in which I_M accounts for the action for the matter component, and the Einstein-Hilbert action$I_{E.H}$ accounts the geometry of the spacetime. The square brackets are to denote that these actions are functionals that can vary with the metric g and/or the physical field ϕ. By using the functional derivative, the Energy-Momentum tensor is defined as:

$$T^{\mu\nu}(x) \equiv \frac{2}{\sqrt{g(x)}} \frac{\delta I_M}{\delta g_{\mu\nu}(x)}$$

and admits these properties: $T^{\mu\nu}(x) = T^{\nu\mu}(x)$ and $D_\mu T^{\mu\nu}(x) = 0$ (D_μ being the covariant derivative operator) . The Einstein-Hilbert action can be written explicitly as

$$I_{E.H}[g] = \frac{1}{16\pi G} \int d^4x \sqrt{g} R,$$

with G being the gravitational constant, R the curvature scalar built from the Riemann curvature tensor which is the standard way to define the curvature of minimally curving manifolds, and $g \equiv -detg_{\mu\nu}$ showing the consideration of the General Relativity context. Imposing the variational principle $\delta I = 0$, we retrieve the Einstein Equations

$$G_{\mu\nu} = R_{\mu\nu} - \frac{1}{2} g_{\mu\nu} R = 8\pi G T_{\mu\nu} \tag{1.4}$$

where $G_{\mu\nu}$ is the Einstein Tensor, symmetrical in the two indices. The equations balance the geometry of space-time on the left-hand side with the physical properties of constituents on the right-hand side.

The Einstein-Hilbert action corrected for the case of cosmological constant is:

$$I_{E.H}[g] = \frac{1}{16\pi G} \int d^4x \sqrt{g} (R + 2\Lambda).$$

Since this term is a scalar like R, it does not change the validity of initial assumptions used to obtain the Einstein Equations. Equation 1.4 then becomes:

$$\begin{gathered} R_{\mu\nu} - \frac{1}{2} g_{\mu\nu} R - \Lambda g_{\mu\nu} = 8\pi G T_{\mu\nu} \\ \Updownarrow \\ R_{\mu\nu} - \frac{1}{2} g_{\mu\nu} R = 8\pi G (T_{\mu\nu} + \frac{\Lambda}{8\pi G} g_{\mu\nu}) \equiv 8\pi G \tilde{T}_{\mu\nu} \end{gathered} \tag{1.5}$$

The top line in equation 1.5 takes the view that Λ is a fundamental constant of nature, while the bottom line instead casts it as a source. As a practical matter, the two views are indistinguishable.

The Energy-Momentum tensor, containing information about both the relativistic and non-relativistic properties of matter density, is written as:

$$T^{\mu\nu} = (p + \rho)u^\mu u^\nu - pg^{\mu\nu} \tag{1.6}$$

for a general metric $g_{\mu\nu}$. Here $u^\mu = (1, \vec{v})/\sqrt{1 - v^2}$ is the 4-velocity of a particle in the fluid. Relativistic scalars ρ and p are respectively the proper energy density and the isotropic pressure and are related by the *equation of state*:

$$w_i = \frac{p_i}{\rho_i} \tag{1.7}$$

for a particular species i.

It can be proven that ordinary matter has $w \in [0, \frac{1}{3}]$ depending on its temperature. In the upper and lower limits respectively, we have:

For ultra-relativistic particles: $v_r \approx 1 \to p = \frac{1}{3}\rho$,

For non-relativistic particles: $v_r \ll 1 \to p \ll \rho$

In case Λ is considered as a source for gravitational field, the Energy-Momentum tensor for the cosmological constant is written as:

$$T^{\mu\nu}_\Lambda = \frac{\Lambda}{8\pi G} g_{\mu\nu} = (p_\Lambda + \rho_\Lambda)u^\mu u^\nu - p_\Lambda g^{\mu\nu} \tag{1.8}$$

where we have combined the two expressions for $T^{\mu\nu}$ from equations 1.5 and 1.6. The total Energy-Momentum tensor is the sum across all particle species including the cosmological constant: $\tilde{T}^{\mu\nu} = T^{\mu\nu} + T^{\mu\nu}_\Lambda$. We define the pressure and density from the cosmological constant as:

$$\begin{cases} p_\Lambda = -\frac{\Lambda}{8\pi G} < 0 \\ \rho_\Lambda = -p_\Lambda = \frac{\Lambda}{8\pi G} > 0 \end{cases}$$

since $\Lambda > 0$. This leads to an intuition of an unknown inordinary species sourced by Λ and having the equation of state $w_\Lambda = -1$. Notice that a positive $\Lambda > 0$ leads to a negative pressure $P < 0$ and as a result, a positive cosmological constant resists the Universes gravitational collapse, and if large enough, can even accelerate the cosmic expansion.

1.2.4 Friedmann Equations

The Friedmann equations were derived by Alexander A. Friedmann for the expansion of space for a homogeneous and isotropic Universe [19]. The detailed derivation can be found in textbooks, such as [20], and in brief is done by plugging in 1.4 or 1.5 the FLRW metric 1.3 and the Energy-Momentum tensor of a perfect fluid 1.6. The final Friedmann Equations for the evolution of the scale factor are:

$$H^2 = (\frac{\dot{a}}{a})^2 = \frac{8\pi G}{3}\rho - \frac{\kappa}{a^2} + \frac{\Lambda}{3} \tag{1.9}$$

$$\frac{\ddot{a}}{a} = (\dot{H}) + H^2 = -\frac{4\pi G}{3}(\rho + 3p) + \frac{\Lambda}{3} \tag{1.10}$$

where the dots represent time derivatives. Scalar factor a, energy density ρ and pressure p are functions of time. The set of Einstein equations (originally with 10 equations) have been simplified to 2 equations basing on the homogeneity and isotropy of the Universe. These two equations can be manipulated to give the third Friedmann equation, also known as the Continuity Equation:

$$\dot{\rho} + 3H(\rho + p) = 0 \tag{1.11}$$

which can also be obtained from the conservation of the stress-energy tensor (1.5) through the Bianchi Idensity $D_\mu G^{\mu\nu} = D_\mu T^{\mu\nu} = 0$. Note that ρ and p are related by the equation of state 1.7. Since we want to consider how the dynamics of the scale factor depend on the densities, we rewrite the Friedmann equations as:

$$(\frac{\dot{a}}{a})^2 = \frac{8\pi G}{3}(\rho - \rho_\kappa + \rho_\Lambda) \tag{1.12}$$

with $\rho_\kappa = -3\kappa/(8\pi G a^2)$ the energy density from the curvature. The density ρ consists of ultra-relativistic and non-relativistic parts, $\rho = \rho_m + \rho_r$. The critical density defined by $\rho_{cr}(t) \equiv \frac{3H^2(t)}{8\pi G}$ is the matter density of a spatially flat Universe ($\kappa = 0$) with no cosmological constant ($\Lambda = 0$). We then have:

$\rho > \rho_{cr}$ for a closed universe

$\rho < \rho_{cr}$ for an open universe

$\rho = \rho_{cr}$ for a flat universe

It's convenient then to consider the densities in terms of the critical density, so we introduce the *density parameter* Ω_i:

$$\Omega_i = \frac{\rho_i}{\rho_c} \tag{1.13}$$

then 1.9 becomes:

$$(\frac{\dot{a}}{a})^2 = H^2(\Omega_m + \Omega_r + \Omega_\kappa + \Omega_\Lambda) \tag{1.14}$$

As the densities scale with the expansion of the Universe, they are naturally expressed as functions of redshift. We define Ω_i at a particular redshift with respect to the present density parameters $\Omega_{0,i}$ by:

Radiation density:$\Omega_r = \Omega_{0,r}(1+z)^4$
Matter density: $\Omega_m = \Omega_{0,m}(1+z)^3$
Spatial curvature density: $\Omega_\kappa = \Omega_{0,\kappa}(1+z)^2$
Cosmological constant density: $\Omega_\Lambda = \Omega_{0,\Lambda}(1+z)^0 = \Omega_{0,\Lambda}$

Equation 1.9 then becomes:

$$H^2(t) = (\frac{\dot{a}}{a})^2 = H_0\sqrt{\Omega_{0,r}(1+z)^4 + \Omega_{0,m}(1+z)^3 + \Omega_{0,\kappa}(1+z)^2 + \Omega_{0,\Lambda}} \tag{1.15}$$

where H_0 is the current Hubble rate. The total density parameter is defined as:

$$\Omega_{tot} = \Omega_m + \Omega_r + \Omega_\Lambda = 1 - \Omega_\kappa$$

To get the evolution of the scale factor, we first derive the dependence of the densities on the scale factor by combining the equation of state and the continuity equation. From then on, solving equation (1.15) is difficult in the general case (involving a transcendental integral), but is simple when the Universes density is dominated by a single species. Three epochs are particularly interesting given the actual composition of our Universe: an early radiation-dominated phase, an intermediate matter-dominated period, and most recently a cosmological constant dominated universe. Without derivation, the resulting dependencies of the densities on the scale factor and the evolution of the scale factor in these three epochs are:

$\rho_r \propto a^{-4} \rightarrow a(t) \propto t^{\frac{1}{2}}$ for radiation-dominated era
$\rho_m \propto a^{-3} \rightarrow a(t) \propto t^{\frac{2}{3}}$ for matter-dominated era
$\rho_\Lambda \propto a^0 \rightarrow a(t) \propto e^{Ht}$ for cosmological-constant-dominated era

The case where the curvature dominates is different with $a(t) \propto t$ for an open universe. It does not appear our Universe has ever (nor will it) gone through a curvature dominated phase. The evolution of the scale factor and densities show that the energy density of the radiation drops most quickly. The era where radiation dominated last until the matter-radiation equality where the non-relativistic matter started changing the scenario. Notice that, since the energy density sourced by the cosmological constant does not change with the scale factor, this density will surpass the other two densities eventually. If we come back to equation 1.14, we will have $\ddot{a} > 0$, which agrees with the current observation that our Universe is undergoing an accelerated expansion. It appears that the dominant contribution to the energy density today is Dark Energy or a cosmological constant.

Up to now, we have looked into the geometry of the Universe and the evolution of the Universe with respect to populating species. Part of the evidence for these theoretical implications is presented in the existence of the Cosmic Microwave Background, which is the foremost interest of this thesis.

1.3 The Cosmic Microwave Background

The Cosmic Microwave Background is the remnant electromagnetic radiation from the very early Universe in the Standard Cosmological Model. While the cosmic inventory offers a variety of subjects like photons, baryons, cold dark matter, neutrinos, and dark energy, this description of the CMB will mainly involve photons as they compose the CMB radiation. Before that, it is interesting to know how the CMB was discovered.

Early research of Big Bang Nucleosynthesis by Gamow, Alpher, and Herman contained the first prediction of an energy density of CMB radiation [21, 22] although the spectral characteristics were not seriously considered. Early in 1964, Russian physicists Doroshkevich and Novikov predicted the CMB to be detectable and have a black body spectrum [23]. In 1965, American scientists Penzias and Wilson accidentally found the CMB radiation in the course of some experiments for radio astronomy and satellite communications [24], for which they were both rewarded with a Nobel Prize. The unaccountable excess in temperature of $\sim 3.5K$ in their antenna was eventually recognised due to the microwave background radiation.

Following the evidence of the existing CMB, the prospect of imaging the early Universe tantalised cosmologists, and drove a series of ever-improving experiments to realise this goal. It took over 20 years until the first result in 1992, when the Cosmic Background Explorer (COBE) Differential Microwave Radiometer experiment first captured the cosmological anisotropies in the CMB temperature field [25]. The FIRAS instrument on the COBE satellite later measured from the CMB an almost perfect blackbody spectrum at $T_0 = 2.725 \pm 0.001K$ [26, 27]

$$I_\nu = \frac{2h\nu^3}{c^2}\frac{1}{e^{\frac{h\nu}{k_B T_0}} - 1} \tag{1.16}$$

The fractional deviation from black-body stayed at $\Delta I_\nu / I_\nu \simeq 10^{-5}$.

The microwave background radiation was understood to have been created in the early hot and dense universe [28]. Initially, the matter in the universe was kept in an ionized state due to high photon energies and number densities. The ionization eventually ended as the universe expanded and cooled, leading to the "recombination" of electrons with protons to form neutral hydrogen. Photons were left to free-stream; their mean free paths subsequently exceeded the horizon of the universe. The background where the recombination happened is called the Last Scattering Surface (LSS). In addition, the radiation was described by Penzias and Wilson to be isotropic, which supports our choice of using the FLRW metric to depict the Universe. However, we also observe in the modern Universe the large structures which are created by gravitational instability correlated to some variations in density. Density variation can be shown to cause the anisotropies in the observed temperature [29]. The assumption of a universe originally almost homogeneous and isotropic is useful for further understanding of complex observables. We will now look into the evolution of anisotropies in the CMB today.

1.3.1 Perturbation evolution

The small inhomogeneities in the CMB are sourced by the quantum perturbations during inflation. The inflationary period affects how the perturbations contribute to the evolution of the anisotropies as depicted in Figure 1.3. The anisotropies are denoted $\Theta = \delta T/T$ in following discussions. Due to rapid expansion, the perturbations are driven outside of the horizon of causal contact and only re-enter therein during the radiation- or matter-dominated eras. The modes re-enter the horizon at a different time which is affected by their comoving size (k^{-1}). Large-scale perturbations whose wavelengths are greater than the horizon size do not evolve much - they are frozen into their initial conditions. Smaller perturbations with wavelengths smaller than the horizon scale re-enter the horizon sooner; their initial states are changed due to causal physics prior to recombination. Note that the Universe always expands, and the temperature decreases. The matter gradually takes over the radiation during CMB recombination, which releases the photons. Those traveling to us carry information about the anisotropies (observed in the temperature variation ΔT as in the Figure 1.3), from which we can create a power spectrum.

We can directly probe the primordial anisotropies sourced by inflation by looking at very large scales, larger than the horizon size at recombination. While these modes have not yet entered causal contact and begun evolving, they still leave an imprint on the CMB through their perturbation to the gravitation potential. This causes two effects: 1) Photons climbing out of the potential well will leave a gravitational redshift imprint $\Theta = \Psi$, and 2) The plasma recombination is dilated by the potential well that delays the time with an offset term of $\Theta = \frac{2}{3}\Psi$ [29]. The net perturbation in today temperature field is a result known as the Sachs-Wolfe effect [29]:

$$\frac{\delta T}{T} = \Theta = \frac{\Psi}{3} \tag{1.17}$$

and these large scales are known as the Sachs-Wolfe plateau. Smaller perturbations are changed due to causal physics prior to recombination. Before recombination at redshift

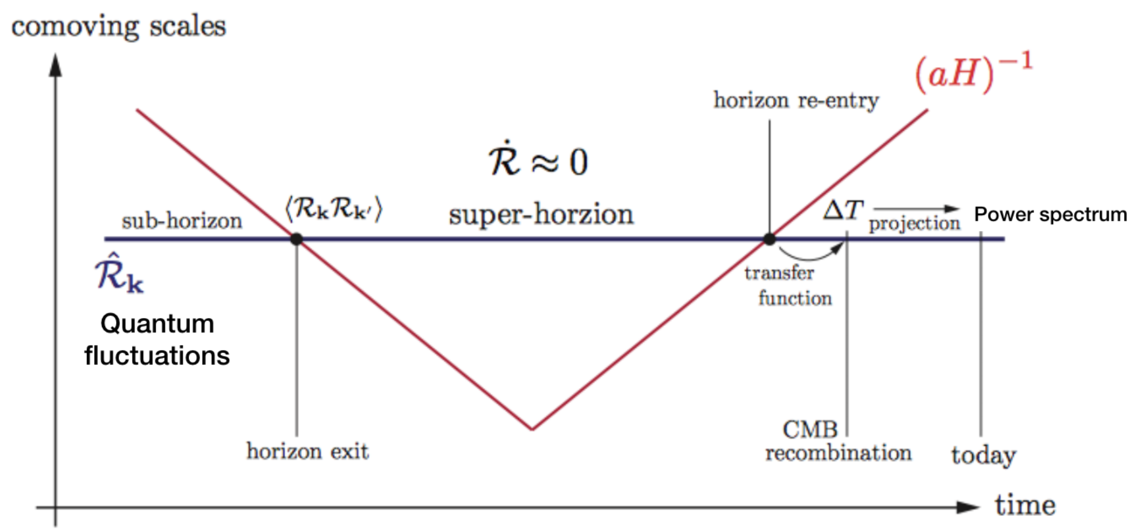

FIGURE 1.3: Perturbation evolution during and after the inflation. The comoving horizon $(aH)^{-1}$ changes, while comoving scales k^{-1} remain constant. At early time, the perturbations exit to the super-horizon where they don't evolve. The correlation function $\langle R_k E_{k'} \rangle$ at early horizon exit thus translates into CMB observables at late times after convolution with the transfer function. [Figure adapted from [3]].

$z \sim 1000$, due to abundant Compton scattering off electrons, photons are strongly coupled to baryons, forming a photon-baryon fluid [30]. The photon pressure resists the gravitational infall caused by a non-baryonic matter called dark matter, triggering the acoustic oscillations.

In Fourier expansion, the perturbations can be written as a sum of oscillating acoustic waves. For simplicity, amplitudes of these oscillations behave like functions $\cos[kr_s(\eta)]$ and $\sin[kr_s(\eta)]$. Here, η is the conformal time defined by

$$\eta = \int_0^t \frac{dt'}{a(t')}$$

with scalar factor $a(t')$ introduced in 1.2.4. We can choose between $\cos[kr_s(\eta)]$ and $\sin[kr_s(\eta)]$ depending on initial conditions of the models. In simplified adiabatic initial conditions, only the *cosine* part of the Fourier modes remains with non-zero amplitudes [31]. The sound horizon r_s can be written as:

$$r_s(\eta) \equiv \int_0^\eta d\eta' c_s(\eta') \tag{1.18}$$

where c_s is the speed of sound which depends on the photon-to-baryon density ratio. These wave oscillations continue until photons decouple from baryons during recombination [30]. The oscillating plane waves typically have maxima or minima at certain k values i.e $k = n\pi/r_s, n = 1; 2; ..$ for cosine mode. Anisotropies should be strengthened at those k-scales, and the extrema represent the temperature crests or troughs [32].

After recombination, the baryon can freely fall in potential wells by dark matter. This leads to the formation of large-scale structures like cluster of galaxies and galaxies that we observe today. The photons however can escape from the potential wells and free-stream to us, carrying information about the recombination through the temperature anisotropies we measure today. Paradoxical as it may sound, given that we observe temperature differences between regions, the photon-baryon fluid actually has the same temperature at recombination. However, recombination happens earlier for low-density, cold regions, so the photons decoupled earlier and have been redshifted to lower temperatures. Conversely, hotter regions recombined later and are observed to be at a higher temperature due to being less redshifted [33].

As we have reviewed the evolution of early perturbations, it may be of interest to know how anisotropies at any point of time can be calculated from these perturbations.

1.3.2 Calculation of CMB anisotropy and perturbation

The small inhomogeneities in the CMB are sourced by the quantum perturbations during inflation. The evolution of these inhomogeneities can be calculated by injecting perturbation terms into the FLRW metric 1.3:

$$ds^2(t,\vec{r}) = (1 + 2\Psi(t,\vec{r}))dt^2 + a^2(t)(1 + 2\Phi(t,\vec{r}))(dx^2 + dy^2 + dz^2) \tag{1.19}$$

where we have assumed a flat Universe. $\Psi(t,\vec{r})$ and $\Phi(t,\vec{r})$ are respectively perturbations to the Newtonian gravitational potential and perturbations to the spatial curvature. The evolution of these perturbation can be determined using Einsteins' equations.

Since the deviations are small, we will only consider linear order perturbations in Ψ and Φ. To start, we can write the initial conditions $\Phi(t_0,\vec{r})$ and $\Psi(t_0,\vec{r})$ as sums of complete basis functions that evolve with time [34]. As for the case of spatial curvature:

$$\begin{aligned}\Phi(t_0,\vec{r}) &= \textstyle\sum_k \phi_k f_k(\vec{r})\\ \Phi(t,\vec{r}) &= \textstyle\sum_k \phi_k F_k(\vec{r})\end{aligned} \tag{1.20}$$

where F_k and f_k are solutions and $F_k(t_0;\vec{r}) = f_k(\vec{r})$. One popular choice of basis functions is the Fourier expansion, which is convenient because k is independent of the coordinate system. We then have k as the Fourier mode and ϕ_k is called the Fourier coefficient. The time dependence and space dependence can be separated as:

$$F_{\vec{k}}(t, \vec{r}) = T_k(t) f_{\vec{k}}(\vec{r}) \tag{1.21}$$

with T_k called the transfer function. The change of the initial perturbations with time now rests in $T_{\vec{k}}(t)$. Using the above relation simplifies the Einstein equations to linear order equations [35, 36].

The perturbations to the total density and momentum fields $\delta\rho$ and δp, contain perturbations to all the different species i populating the universe: $\delta\rho = \sum_i \delta\rho_i$ and $\delta p = \sum_i \delta p_i$. The nature of the species decide how the perturbations interact with each other and with the metric. For Λ_{CDM}, the Universe is populated with photons, normal matter (ions and electrons), cold dark matter, and neutrinos [36]. We are interested in the evolution of photon perturbation since that is what we observe. Consider the small perturbations of the temperature field $T + \delta T$. The photon perturbation field can be described as $\Theta(\eta, \vec{x}, \vec{n}) \equiv \frac{\delta T}{T}(\eta, \vec{x}, \vec{n})$ in the direction $\vec{n}$, where the temperature at conformal time η is $T + \delta T$. The notion $\vec{x}$ means that we initially present the perturbation in generic coordinates. Again, going to Fourier space

$$\Theta(\eta, \vec{x}, \vec{n}) = \int \frac{d^3k}{(2\pi)^3} e^{i\vec{k}\cdot\vec{x}} \Theta(\eta, \vec{k}, \vec{n}) \tag{1.22}$$

is convenient since the interactions do not couple different Fourier modes: Thomson scattering between photons and electrons, metric perturbations changing photon energies. As these interactions happen simultaneously, we solve for the Θ at some point in time through systems of (differential) Boltzmann equations for the phase space distribution evolutions. Detailed equations and accurate numerical solution techniques are presented in [34, 35, 36] .

Thus, a full picture of the CMB sky today can be given if we have a precise initial inhomogeneity distribution. However, for an isotropic Universe, the phase information is not physically significant, and we contemplate the initial inhomogeneities to be Gaussian random fluctuations. Thus we are generally only interested in the power spectrum, which will be introduced now.

1.3.3 CMB temperature Power Spectra

Models that describe the origin of the anisotropies like in section 1.3.1 only give the statistical properties of the anisotropies. We thus focus on two-point correlation functions because any case for an even number of points can be simplified to a two-point correlation, while an odd number of points results in zero following Wick's theorem.

Again, as the CMB spectrum can be considered a blackbody [26] of a nearly constant temperature T across the field of sky, we can consider the statistics through the temperature fluctuation in the CMB temperature field $\Theta(\vec{n}) = \delta T(\vec{n})/T$. The direction $\vec{n}$ for every point on the sky is given by two angular coordinates (θ, ϕ). We thus transform the full sky anisotropies to the spherical harmonic basis:

$$\Theta(\vec{n}) = \sum_{l=1}^{\infty} \sum_{m=-l}^{l} a_{lm}^{T} Y_{lm}(\theta, \phi) \tag{1.23}$$

with superscript T meaning temperature, $Y_{lm}(\theta, \phi)$ being the spherical harmonics functions which satisfy the normalisation relations:

$$\int d\Omega Y_{lm}(\theta, \phi) Y_{lm}^{*}(\theta, \phi) = \delta_{ll'} \delta_{mm'} \tag{1.24}$$

And l is angular frequency, and m, running from $-l$ to l, carries the orientation and phase with respect to the sphere. The multipole moments

$$a_{lm} = \int d\Omega Y_{lm}^{*}(\theta, \phi) \Theta(\theta, \phi)$$

give the strength of the anisotropy for a particular Y_{lm}. As we expect the anisotropies to be Gaussian-distributed, we expect the mean of all a_{lm} to be zero and the variance for a_{lm}, denoted by C_l, to be non-zero:

$$\langle a_{lm} \rangle = 0; \langle a_{lm} a_{lm}^{*} \rangle = \delta_{ll'} \delta_{mm'} C_l \tag{1.25}$$

The quantity C_l is known as the *power spectrum*. In practice, we do not calculate the power spectrum with equation 1.25 because it implies we need to take the mean of harmonic coefficients from an infinite set of realisations of the Universe, while our current Universe is just one realisation from stochastic processes that source initial perturbations. So instead, we build an estimator $\hat{C}_l$ by taking the mean on $2l + 1$ m modes for each multipole l:

$$\hat{C}_l = \frac{1}{2l+1} \sum_{m=-l}^{l} a_{lm} a_{lm}^{*} = \langle a_{lm} a_{lm}^{*} \rangle \tag{1.26}$$

which gives the expectation value measured across the sphere. Note that on small regions of sky, the spherical harmonic transform can be approximated by a Fourier transform. In this approximation, the multipole moment a_{lm} becomes the Fourier coefficient, with $l = k$. Given the sky coverage of the data used in this thesis, we will use the flat-sky approximation and Fourier transforms.

CMB temperature power spectra have been well-measured with several experiments carried out since the prediction of the existence of the CMB. Three prominent experiments are COBE [25], WMAP [37] and Planck [38], all of which give full sky pictures. The measurement of the temperature anisotropy power spectrum C_l^{TT} from Planck Collaboration is shown in Figure 1.4.

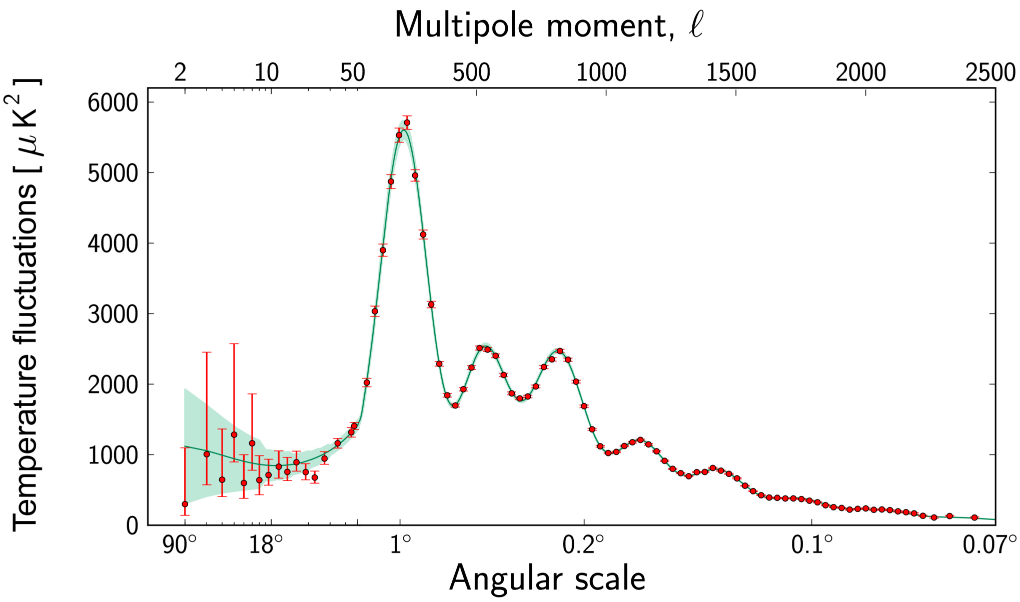

FIGURE 1.4: The green curve shown in the graph represents the best fit of the 'standard model of cosmology' - currently the most widely accepted scenario for the origin and evolution of the Universe - to the Planck data. The pale green area around the curve shows the predictions of all the variations of the standard model that best agree with the data. The red dots correspond to measurements made with Planck; these are shown with error bars.[Picture and description from ESA]

It is conventional to plot the power spectra with the multiplicative factor $l(l+1)/2\pi$ like in the figure to make features of the spectrum more distinguishable. At multipoles below the first prominent peak localised at $l \simeq 220$, the seemingly flat spectrum is the Sachs-Wolfe plateau and preserves the primordial spectrum from inflation. The entire first peak and around was not well-measured until the BOOMERang experiment [39] and MAXIMA experiment [40]. Multiple peaks of the spectrum correspond to the maxima and minima of the oscillating acoustic waves. If there was no change in the physics, we would have peaks at exactly the same height! The heights of the peaks are decided by the baryon-photon ratio, and the matter radiation ratio [32]. The heights of peaks hint at the matter density contents because the interplay between photon pressure and dark matter potential well (and thus the acoustic oscillations) changes with respect to the dark matter density. The spectrum part starting at around $l = 1000$ to higher l is called the damping tail as the peaks clearly are vanishing. Note that CMB photons random walk until they bounce with baryons during recombination. As the decoupling between baryons and photons increases, their mean free path grows. Hence, on the angular scales smaller than the mean free path, the anisotropies are less enhanced, and the temperature fluctuations are damped, showing the damping tail.

A final comment is that results from C_l^{TT} power spectrum measurements have been supporting ΛCDM as the best fitting model of the Universe. In 2013, Planck collaboration reported the model constraints with standard deviations of under 5% for 5 parameters in their 6-parameter ΛCDM model using temperature data alone [41]. Overview of parameters in cosmological models will be presented later in 1.5.

1.4 Polarisation of the CMB

In addition to the temperature anisotropy, it is also worth studying the anisotropies of the CMB polarisation. The CMB polarisation anisotropies are particularly interesting probes of new physics during recombination (when polarisation is sourced) and also promise a new window into the inflationary epoch. We will first revisit the definition of polarisation.

1.4.1 Basics of polarisation

CMB light is an electromagnetic wave. An electromagnetic wave propagating in the $\hat{z}$ direction is the sum of its electric field along 2 axes x and y:

$$\vec{E} = E_x \hat{x} + E_y \hat{y} \tag{1.27}$$

Here,

$$\begin{aligned} E_x &= E_{x0} e^{i(kz - wt)} \\ E_y &= E_{y0} e^{i(kz - wt + \phi)} \end{aligned} \tag{1.28}$$

where ϕ is the relative phase between the two components and can depend on time. The physical field is essentially the real part of E. The Stokes parameters are defined as [42]:

$$\begin{aligned} I &= \langle E_{x0}^2 + E_{y0}^2 \rangle \\ Q &= \langle E_{x0}^2 - E_{y0}^2 \rangle \\ U &= 2\langle E_{x0} E_{y0} \cos(\phi_x - \phi_y) \rangle \\ V &= 2\langle E_{x0} E_{y0} \sin(\phi_x - \phi_y) \rangle \end{aligned} \tag{1.29}$$

where the bracket means a time average. The axis of polarisation is defined as the angle $\alpha \equiv \frac{1}{2} \arctan \frac{U}{Q}$.

Under rotations of the axes in xy plane, Q and U respective orientations are changed while I and V stay unchanged. A rotation of $\hat{x} - \hat{y}$ axes with an angle θ changes the Stokes parameters as:

$$\begin{aligned} Q' &= Q\cos(2\theta) + U\sin(2\theta) \\ U' &= -Q\sin(2\theta) + U\cos(2\theta) \end{aligned} \tag{1.30}$$

The magnitude of polarisation is:

$$P = \sqrt{Q^2 + U^2 + V^2}$$

although the circular polarisation V is typically not measured by CMB experiments because V polarisation is not generated in the Standard Cosmological Model. The polarisation fraction is P/I.

1.4.2 How CMB is polarised

Thomson scattering partially polarises the CMB. Light coming to an electron from one single direction will create only one linear polarisation state. If light also comes from a direction perpendicular to the first direction with the same intensity, as in the case of a dipole, the net polarisation will be canceled. The scattered light from a radiation dipole or quadrupole is shown in Figure 1.5. Thomson scattering results in a net CMB linear polarisation only if there is a local radiation quadrupole.

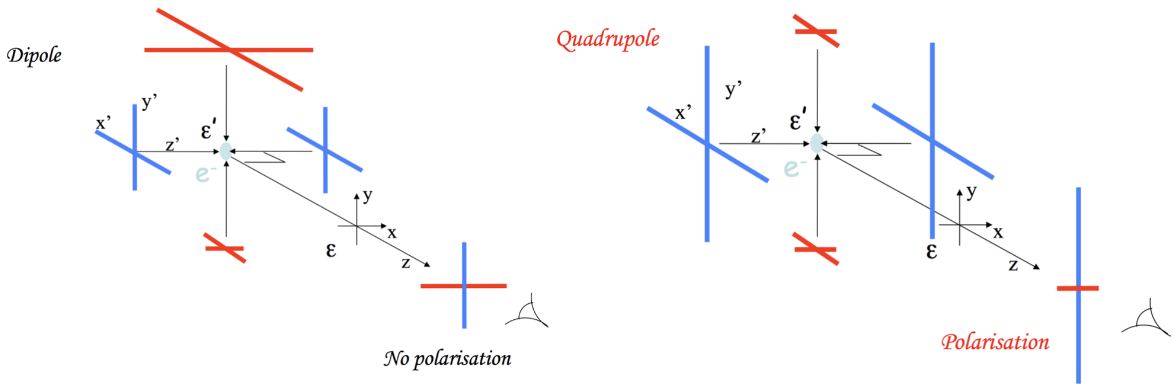

FIGURE 1.5: Thomson scattering of radiation. Only a quadrupole anisotropy generates linear polarisation. [Figure made using images from [4]].

These can also be proved mathematically. Following the treatment detailed in [43], the main calculations can start with Thomson scattering cross-section for incident and outgoing radiations with polarizations $\hat{\epsilon}', \hat{\epsilon}$ given by:

$$\frac{d\sigma}{d\Omega} = (\frac{3\sigma_T}{8\pi})^2 |\hat{\epsilon} \cdot \hat{\epsilon\prime}|^2 \tag{1.31}$$

where σ_T is the Thomson cross section. The integration of this quantity over all directions gives the radiation fields I, Q, U. They can be decomposed into spherical harmonics like the temperature field; for example:

$$I(\theta, \phi) = \sum_{l=1}^{\infty} \sum_{m=-l}^{l} a_{lm}^T Y_{lm}(\theta, \phi) \tag{1.32}$$

The resulting outgoing Stokes parameters are:

$$I = \frac{3\sigma_T}{16\pi\sigma_b} \Big[\frac{8}{3}\sqrt{\pi} a_{00} + \frac{4}{3}\sqrt{\frac{\pi}{5}} a_{20}\Big] \tag{1.33}$$

$$Q = \frac{3\sigma_T}{4\pi\sigma_b} \frac{2\pi}{15} Re(a_{22}) \tag{1.34}$$

$$U = -\frac{3\sigma_T}{4\pi\sigma_b} \frac{2\pi}{15} Im(a_{22}) \tag{1.35}$$

These 3 equations show that Thomson scattering can only create polarisation if the incoming radiation has a non-zero a_{22} quadrupole moment. When tightly coupled to the baryons, quadrupoles are suppressed. However as the photon mean free path begins to grow during recombination, local quadrupoles begin to grow.

Quadruple anisotropies originate from three types of perturbations, corresponding to three different physical sources. Scalar perturbation due to density fluctuations creates matter over-densities and under-densities. Due to these inhomogeneities, photons free-streaming at recombination induce anisotropic incoming radiation containing quadrupoles. Vector perturbations correspond to vortical motions of the matter. Quadrupole pattern is generated by the Doppler effect on the velocity (of the vortical motions) perpendicular to the light propagating direction. Velocity and thus vorticity decays with the Universes expansion, so inflation models generically predict zero vector perturbations. Tensor perturbation refers to perturbations to the metric i.e gravitational waves. The distortion of space-time by the gravitational waves induces local quadrupole moments that then produce polarisation. We focus on the scalar and tensor perturbations, given that vector perturbations vanish in inflation.

1.4.3 E and B decomposition

CMB polarisation can be quantified by the scalar fields Q and U measured at every point on the sky. However, since Q and U are defined relative to a given coordinate system, their values depend on the coordinates. Instead, we would like to use coordinate-independent quantities to record the polarisation properties of the CMB.

Notice that 2D Fourier transforming $Q(\vec{x})$ and $U(\vec{x})$ gives Q and U in the frame of the wave vector $Q(\vec{l})$ and $U(\vec{l})$. Since CMB light can come to observers from all directions, calculating $Q(\vec{x})$ and $U(\vec{x})$ requires taking in a rotation to align the direction of propagation with the direction of observation $\vec{x}$. It is thus convenient to simply choose the direction of propagation $\vec{l}$ as the coordinate frame. This leads to construction of polarisation quantities with orientations parallel or perpendicular to the wave vector $\vec{l}$, and those with orientations aligned at $\pm 45°$ relative to the wave vector. These are called respectively E-modes and B-modes. This representation is independent of 1 fixed coordinate system.

Explicit expressions of $E(\vec{l})$ and $B(\vec{l})$ through $Q(\vec{l})$ and $U(\vec{l})$ are:

$$\begin{aligned} E(\vec{l}) &= Q(\vec{l})\cos(2\vartheta_{\vec{l}}) + U(\vec{l})\sin(2\vartheta_{\vec{l}}) \\ B(\vec{l}) &= -Q(\vec{l})\sin(2\vartheta_{\vec{l}}) + U(\vec{l})\cos(2\vartheta_{\vec{l}}) \end{aligned} \tag{1.36}$$

Here, $\vartheta_{\vec{l}}$ denotes the angle between the orientation of Q in the original cooridinate system and the orientation of the wave vector. Orientations of E and B are shown in Figure 1.6, from which E-mode appears to have even parity while B-mode has odd parity.

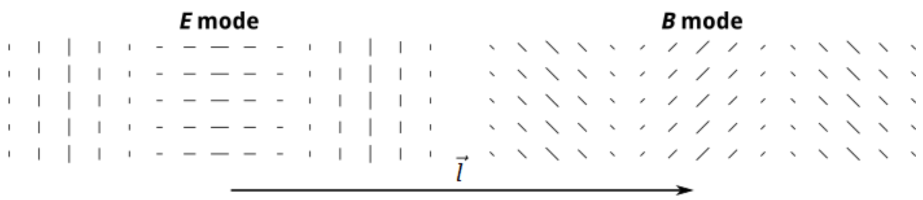

FIGURE 1.6: Polarisation patterns from an E-mode or B-mode wave traveling in $\vec{l}$ direction of propagation. [Picture adapted from the site of [5]]

As E and B depend on the direction of the wave vectors which can align all over, measurement of polarisation at one single point cannot be assigned E or B. They are converted from Q and U measured in 1 portion of sky. The power spectra C_l^{EE} and C_l^{BB} can retrieved by taking average of $E(\vec{l})$ and $B(\vec{l})$ field similar to C_l^{TT}.

$$C_l^{XY} = \frac{1}{2l+1} \sum_{m=-l}^{l} a_{lm}^{XY} a_{lm}^{*XY} \tag{1.37}$$

where X and Y can refer to T,E, or B. Due to the difference of their symmetries, the TB and EB are expected to be zero.

1.4.4 E-mode and B-mode generation

As previously discussed, CMB polarisation is produced by electrons viewing quadrupole patterns. These quadrupoles may be sourced by either scalar or tensor perturbations. Photons entering a scalar over-density have their energy increased by the Doppler effect along their directions $\vec{k}$ only. This leads to linear polarisation perpendicular to the propagation direction, $\vec{k}$. Photons entering a scalar under-density have energy decreased along a direction parallel to $\vec{k}$. The resulting polarisation is parallel to $\vec{k}$. In both cases, the parity is reserved, so scalar perturbations source only E-mode polarisation. Since temperature fluctuations and E-mode polarisation are both generated by the same density fluctuations, we also expect the acoustic peaks to be present in C_l^{EE}, and the T and E fields to be correlated. The first detection of C_l^{EE} and C_l^{TE} was in 2002 [44], and these two spectra have been well-characterized in the last decade.

Generation of B-mode polarisation is to be expected from gravitational waves or gravitational lensing of CMB photons traveling from LSS to reach us today [45, 46]. These two mechanisms happen at different angular scales. Gravitational wave is the tensor perturbation described earlier that breaks the even parity around the direction of propagation, changing E-modes to B-modes.

While not the main subject of this thesis, it can be added measuring B-mode signal from primordial gravitational waves is an incredible challenge. In March 2014, BICEP2 Collaboration reported a discovery of B-mode pattern [47]. However, subsequent analyses using data from the Planck satellite have shown that those B-modes are sourced instead from Galactic foregrounds (specifically dust)[48]. POLARBEAR is targeting primordial B-modes with its survey of large area and its future upgrade to the Simons Array with 3 telescopes.

1.4.5 Current status of E-mode measurement

Measuring the EE power spectrum is the first important milestone in the study of CMB polarisation. Generations of experiments have taken up this endeavor, starting as early as with DASI [44] and MAXIPOL [49]. Experiments Planck [15], ACTPOL [16], and SPTpol [6] all advance the range of the angular scale of the spectrum, with SPTpol exploring the angular scale of up to $l = 8000$. The resulting EE spectrum from SPTpol is shown in Figure 1.7.

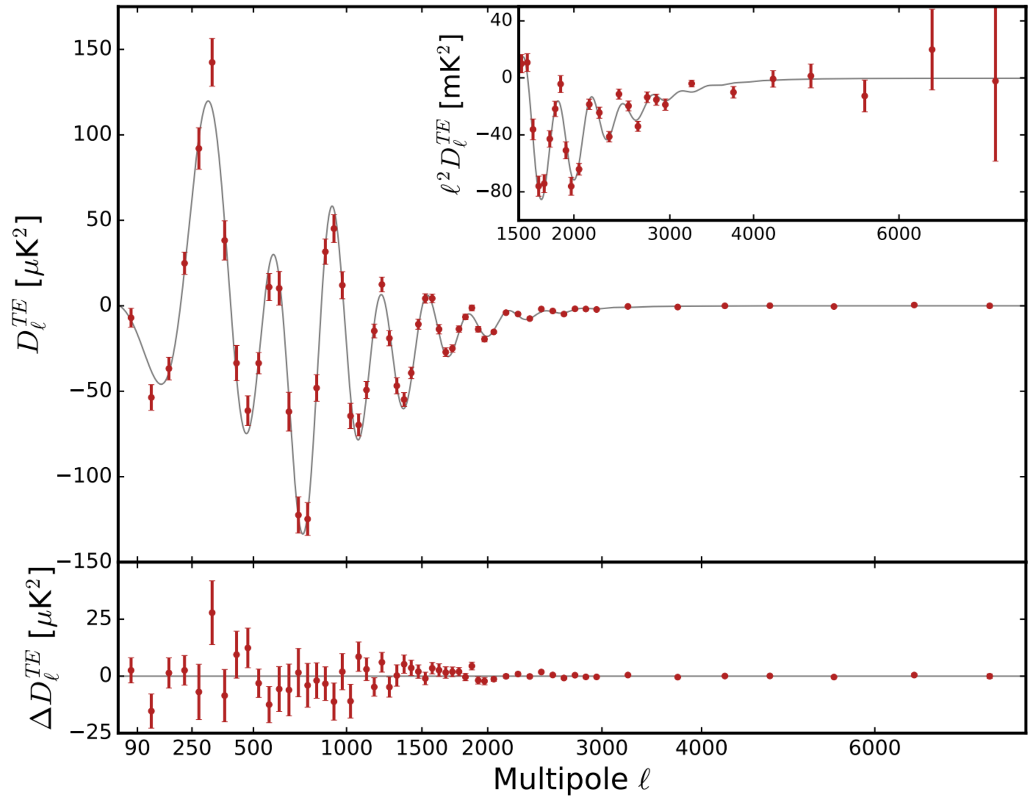

FIGURE 1.7: EE auto-correlation angular power spectrum measured by SPTpol. The red crosses are data; the solid gray lines are the best-fit ΛCDM model to the plikHM TT lowTEB dataset.[Figure from [6]].

Still these measurements are by no means cosmic variance limited, and further improvements are possible. Precise measurements of the EE spectrum have the potential to more than double the information content of the temperature power spectrum since extragalactic foregrounds are less significant at high l in polarisation than temperature. Additionally, adding the EE power spectrum information breaks degeneracies between different extensions to the standard cosmological mode. For instance, changing the primordial Helium abundance or the number of relativistic species both lead to degenerate effects (extra Silk damping) on the temperature spectrum [50], but this degeneracy can be brokwn broken once C_l^{EE} is measured as well. Exploring cosmological model parameters with an EE spectrum measured by POLARBEAR is the main goal of this thesis.

1.4.6 Lensing of the CMB

As CMB photons propagate from the LSS to us, they encounter large scale density fluctuations, inducing random deflections. The deflection angle $\nabla\phi$ is related to the projected surface density or, equivalently, the projected gravitational potential. The remapped primordial unlensed CMB field by two-dimensional vector field in the sky is called the deflection field and is given by [51]:

$$T(\hat{\mathbf{n}}) = T(\hat{\mathbf{n}} + \nabla\phi(\hat{\mathbf{n}}))\ (Q \pm iU)(\hat{\mathbf{n}}) = (Q \pm iU)(\hat{\mathbf{n}} + \nabla\phi(\hat{\mathbf{n}})) \tag{1.38}$$

Note that $\phi(\hat{\mathbf{n}})$ is the CMB lensing potential:

$$\phi(\hat{\mathbf{n}}) = -2\int_0^{z_{rec}} \frac{dz}{H(z)}\Psi(z, D(z)\hat{\mathbf{n}})\left(\frac{D(z_{rec}) - D(z)}{D(z_{rec})D(z)}\right) \tag{1.39}$$

Here, $D(z)$ is the comoving distance to redshift z in the assumed flat cosmology, $D(z_{rec})$ is the comoving distance to the LSS at $z_{rec} = 1100$. $D(z)\hat{\mathbf{n}}$ gives the photon path, $H(z)$ is the Hubble factor at redshift z, and $\Psi(z, D(z)\hat{\mathbf{n}})$ is the three-dimensional gravitational potential. Equations show that these subtle deflections shifts the polarisation on the sky but do not rotate it. This is equivalent to changing the direction of the wave-vector of a mode while keeping its polarisation, which makes sense how gravitational lensing can induce B-mode polarisation from primordial E-mode polarisation. In explicit expression, a primordial E-mode $E(\vec{l}) = \delta(\vec{l} - \vec{l}')$ is translated into observable E- and B- modes as:

$$\Delta E(\vec{l}) = \frac{\cos(2\vartheta_{\vec{l}\vec{l}'})}{(2\pi)^2}W(\vec{l}, \vec{l} - \vec{l}');\ \Delta B(\vec{l}) = \frac{\sin(2\vartheta_{\vec{l}\vec{l}'})}{(2\pi)^2}W(\vec{l}, \vec{l} - \vec{l}'), \tag{1.40}$$

where

$$W(\vec{l}, \vec{l} - \vec{l}') = -[\vec{l} \cdot (\vec{l} - \vec{l}')]\phi(\vec{l} - \vec{l}'), \tag{1.41}$$

and $\vartheta_{\vec{l}\vec{l}'} \equiv \vartheta_{\vec{l}} - \vartheta_{\vec{l}'}$. Integration of multiple E modes using equation 1.40 gives the final ΔE and ΔB.

While B-modes from gravitational waves are Gaussian-featured, the B-modes from gravitational lensing show non-Gaussianity due to the variation of the correlation between E and B across Fourier space scales.The power spectrum of $\phi(\hat{\mathbf{n}})$ in the Limber approximation [52] is:

$$C_l^{\phi\phi} = \frac{8\pi^2}{l^3}\int_0^{z_{rec}} \frac{dz}{H(z)}\Psi(z, D(z)\hat{\mathbf{n}})\left(\frac{D(z_{rec}) - D(z)}{D(z_{rec})D(z)}\right)^2 .P_\Psi(z, k = l/D(z)) \tag{1.42}$$

where $P_\Psi(z, k)$ is the matter power spectrum.

Due to low correlation between the structures as described by the gravitational potential Ψ on large scales, the gravitational lensing effect appears non-trivial only at small angular scales in the CMB. CMB lensing has been conclusively detected in multiple CMB experiments. The first measurements were indirectly done via cross-correlations

Table 1.1: Parameters in the ΛCDM model and and their definitions

Parameter	Definitions
$\boldsymbol{\Omega_b h^2}$	Physical baryon density
$\boldsymbol{\Omega_c h^2}$	Physical dark matter density
$\boldsymbol{100\theta_{MC}}$	100 times of angular size of sound horizon at scattering
$\boldsymbol{\tau}$	Optical depth due to reionisation
$\boldsymbol{\ln(10^{10}A_s)}$	Log of scalar amplitude
$\boldsymbol{n_s}$	Scalar spectral index
$\boldsymbol{dn_s/dlnk}$	The running of the scalar spectral index
$\boldsymbol{N_{eff}}$	Effective number of relativistic species
$\boldsymbol{Y_{He}}$	Primordial helium fraction

with large-scale structures detected by galaxy surveys [53, 54, 55, 56]. Detection of lensing using CMB data alone were rendered possible by recent CMB instruments with higher sensitivity and resolution, such as the Atacama Cosmology Telescope (ACT), the South Pole Telescope (SPT), and Planck ([57, 58, 59]). The study of CMB lensing potential is important for extraction of true primordial gravitational wave B-modes from systematics.

Having introduced the spectra that we can measure with CMB experiments, I will now give a review of the cosmological parameters that the information from the spectra might shed light on.

1.5 Review of parameters

Cosmological models for parameter constraints can be the original 6 parameter ΛCDM model and the ΛCDM model extended by varying additional parameters. The name of ΛCDM suggests our focus on the cosmological constant Λ and cold dark matter (CDM). As introduced in 1.2.4, these two can be learned about via estimations of the radiation energy density, which is dominated by photons and neutrinos, and the baryonic matter density, which relates to visible matter in the known Standard Model (SM) particles.

Cosmological data in this work have been fit to models with 6-8 parameters described in Table 1.1:

The scalar amplitude A_s and the spectral index n_s characterise the initial conditions through the approximately scale-invariant spectrum of primordial curvature:

$$\mathbf{P}_{\zeta}(k) = A_s(\frac{k}{k_0})^{n_s-1} \tag{1.43}$$

which is typically pivoted at $k_0 = 0.05 Mpc^{-1}$. A nearly scale-invariant primodial spectrum is a generic prediction of inflationary models [3]. Most realistic inflationary models allow the variation of the spectral index with regards to the wave-number k [60]. Since the range of k can extend to scales below the accessible range of CMB measurements, it is reasonable to speculate n_s can evolve with respect on the scales where it is measured. This dependence is presented by the running of n_s, which is quantified by $dn_s/dlnk$.

The optical depth τ impacts on the overall amplitude of the spectrum as $A_s e^{-2\tau}$. The reason is reionisation of neutral hydrogen by the ultraviolet radiation from formation of galaxies and first stars causes the optical depth to increase and damp the scales below the horizon by a factor of $e^{-2\tau}$ [61]. Delensing power spectra for more precise measurements of the acoustic peaks can partially help break the degeneracy between A_s and τ (see e.g [62],[63]). There is also small degeneracy between the spectral index and the optical depth in the temperature power spectrum, but this is expected to be resolved with information from the low-ℓ range of the polarisation spectrum [61].

The baryon, dark matter, and massive neutrino densities contribute to the total matter density introduced in Chapter 1 following $\Omega_m = \Omega_b + \Omega_c + \Omega_\nu$. These densities are timed with the reduced Hubble constant $h \equiv H_0/100kms^{-1}Mpc^{-1}$. Used in place of the Hubble constant, the angular size of the horizon at scattering is $\theta_s \equiv r_s/D_A$, where both the physical sound horizon r_s and the angular diameter distances are estimated at the redshift of last scattering. This parameter is an immediate measure of the location of the peaks in the CMB spectrum due to its relation with the distance to last-scattering. The peak locations are indirect measurements of the Hubble parameter H_0 and the physical matter density Ω_m, both of which are important to the expansion history. As introduced in Chapter 1, the peak heights compared to the large-scale plateau of the spectrum can reveal on Ω_m because they relate to the amplitude of the cosmic sound waves, which vary with the time of matter-radiation equality driven by the radiation. Small-scales modes that got in the horizon during the radiation-dominated era are amplified compared to those that entered in the matter era. In addition, the peak heights relative to each other are affected by the baryon density Ω_b due to baryon loading.

The effective number of relativistic species and the primordial helium fraction can be probed with the damping tail of the spectrum. The effective number of relativistic species N_{eff} can impact on the radiation density, which is relevant to the early expansion history. From Chapter 1, the early universe is also populated with massive neutrinos, which account for a significant fraction of the total radiation density at that time, while today's universe is abundant with massless neutrinos. Therefore, the gravitational effects of neutrinos are expected to leave distinct imprints in the CMB and BAO spectra that reveal about the past universe (see [61],[64]) although they don't contribute majorly to the present total energy density.

At early times, SM particles stay in thermal equilibrium until the interaction rate of a species drops below the Hubble rate, leading to these particles losing thermal contact with other species and decoupling from the primordial plasma. As the most weakly interacting SM particles, neutrinos decouple first mainly via electron-position pair conversions and neutrino scattering off leptons. In the limit where decoupling is instantaneous, we would expect the number of relativistic species to be $N_{eff} = 3$ or 3 neutrino species. In reality, neutrinos have not fully decoupled during electrons and positrons annihilation. Accounting this effect and correcting for quantum electrodynamics, flavour oscillations in plasma, the effective number of neutrinos is found to be $N_{eff} = 3.046$ in the Standard Model [65]. Deviation from this number can mean non-standard characteristics of neutrinos or a different thermal history with different total radiation density components.

Varying the radiation density in the early universe can impact the CMB power spectrum through several ways, which have been examined in [50]. Impacts due to neutrinos are expected to result in phase shifts in CMB spectra. The reason is these phase shifts can be caused when the speed of sound in the photon-baryon fluid is exceeded by the speed of fluctuations in the gravitational potential, and these fluctuations can be affected by neutrinos decoupling [61, 66]. The E-mode power spectrum has been estimated to see the same phase shifts as the temperature power spectrum [61]. With more precise measurements of the polarisation spectrum, the sensitivity to this effect should be improved.

The constraint of the effective number of neutrinos N_{eff} and the primordial helium fraction Y_{He} can be correlated with each other due to the additional degeneracy between Y_{He} and the expansion rate H pointed out in [66]. An increase in Y_{He} at a fixed baryon density would lead to more damping because the helium binding energy is larger than that of hydrogen, which means a reduced number of free electrons during hydrogen recombination. The degeneracy between N_{eff} and Y_{He} is expected to be weakened with the inclusion of Big Bang nucleosynthesis (BBN) data due to that N_{eff} affects the radiation density around the time of recombination while Y_{He} reveals on the total radiation density at BBN's time [61], although BBN data are not used in this work.

Chapter 2

The POLARBEAR experiment

POLARBEAR is a multiple-stage CMB experiment focusing on measurements of CMB polarisation, specifically the B-modes induced by primordial gravitational waves and gravitational lensing. The first phase, POLARBEAR-1, commenced in early 2012, and is the main focus of my thesis work. An upgrade to the instrument, the Simons Array, saw the first light in 2019. Situated in the James Ax Observatory site in Chile, POLARBEAR-1 consists of a cryogenic receiver with a focal plane mounted on the Huan Tran Telescope. This overview of the POLARBEAR experiment will introduce the observation site, the telescope, the receiver, then will come to the observation strategy.

2.1 Observation site

FIGURE 2.1: POLARBEAR looking at the sky at Jamex Ax Observatory in Chile.

The James Ax Observatory is located in the Atacama Desert in Chile at latitude $-22.958°$, longitude $292.214°$, and an elevation of over 5,200 meters. The location is near the the ALMA observatory and is one of the best observation sites in the world. Near 150 GHz i.e the observing frequency of POLARBEAR, atmospheric absorption and emission from oxygen and water molecules degrades the sensitivity of ground-based instruments to the microwave radiation from the CMB . Hence, sites with high altitude and dry weather like the Atacama Desert are ideal for millimeter-wave observations. The typical precipitable water vapour (PWV) column depth of the site is an extremely low $1mm$ [67]. The atmosphere temperature at $PWV = 1mm$ is $\sim 18°C$. In addition, the Southern Hemisphere location is advantageous since the southern sky covers a larger area of low galactic foreground contamination than the northern sky, and a number of up-coming large surveys such as LSST and SKA are located in the Southern hemisphere, opening the potential for cross-correlation studies.

2.2 The Huan Tran Telescope

The Huan Tran Telescope (HTT), on which POLARBEAR-1 is mounted, is a two-mirror off-axis Gregorian system (more specifically a Gregorian-Dragone system). Figure 2.2 shows the telescope and the ray tracing of the optics. The HTT precision primary mirror has the diameter of 2.5 meters and a surface of 53 μm RMS accuracy [7]. The guard ring is 3.5 meters in diameter, created with lower precision and constructed from eight individual panels. As such, the main beam of the instrument is constructed with only the precision primary reflector surface; the guard ring plays roles in redirecting any spillover to the cold sky rather than the ground. The resulting beam is approximately Gaussian with FWHM $\simeq$ 3.5 arcminute at 150 GHz. The beam smooths out angular scales at $l > 2500$. Other visible components are the co-moving ground shield, prime focus baffle, and secondary mirror enclosure. The reimaging and detector components are hidden inside of the cryostat.

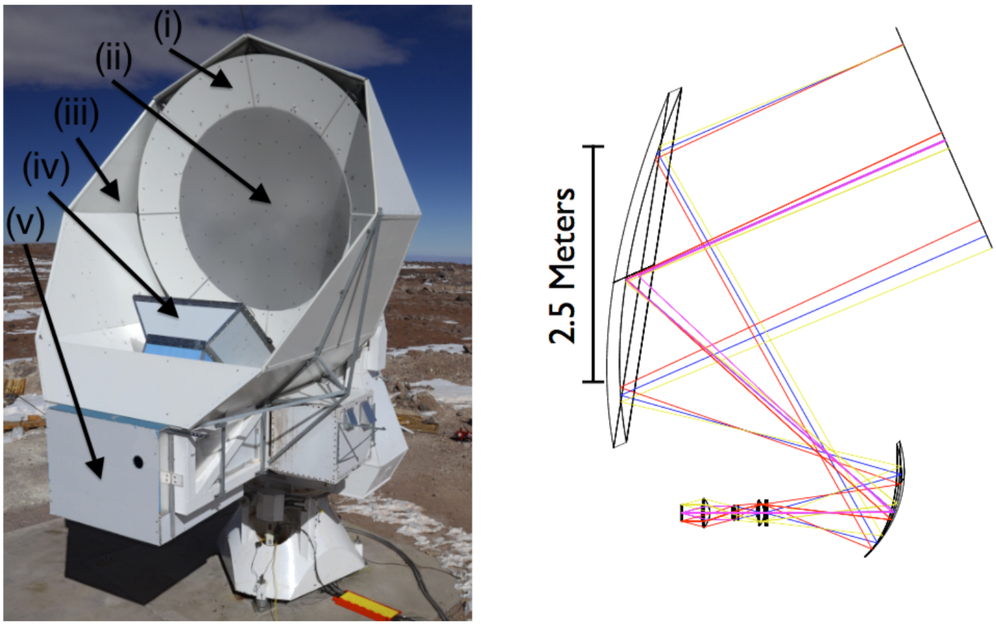

FIGURE 2.2: Left: The Huan Tran Telescope with: (i) the primary guard ring, (ii) the primary mirror, (iii) the co-moving ground shield, (iv) the prime focus baffle, and (v) the secondary mirror enclosure. Right: Ray-tracing showing the optical path through the telescope and cold lenses in the focal plane. [Figure borrowed from [7]]

The off-axis Gregorian mirrors of HTT are designed to satisfy the Mizuguchi-Dragone condition [68, 69] which sets the tilt of the symmetry axes of the conics for both mirrors in order to maximally mitigate cross-polarization over a broad field of view with limited diffraction. An off-axis design has an unobstructed aperture, which is beneficial as the secondary mirror support structures for an on-axis telescope can scatter or diffract light, and introduce potentially polarised sidelobes.

The Gregorian-Dragone design, along with the crossed-Dragone, are two popular off-axis dual-reflector designs for CMB experiments. In Gregorian setting, the secondary mirror is smaller than that of the crossed design, and thus demands less on the baffles needed to limit far sidelobes caused by stray light at the receiver window, and helps to simplify the mechanical structure design. One setback in Gregorian design is that it has a smaller field of view than the equivalent crossed design. As a result, it has more limited diffraction in comparison to the equivalent alternative [70]. As an aside, the Gregorian-Dragone design is being supplanted by crossed-Dragone designs in future experiments. The Gregorian designs have been more popular to dates since the smaller secondary mirror means a cheaper telescope and simplifies the sidelobe baffling. However, crossed-Dragone designs have larger fields of view, which is crucial to fitting in large focal planes of future experiments.

2.3 The POLARBEAR cryostat

The fundamental limit to a CMB detectors sensitivity is the quantum fluctuations in the photon arrival rate [71]. To reach this fundamental limit, the detectors must be cooled to cryogenic temperatures to minimise thermal noise. In addition, notice that the photon noise scales with the total optical signal which includes both the CMB and optical emission from the atmosphere and elements in the optical chain. We thus want to minimize in-band optical emission from elements of the optical chain. Since emission increases with temperature, it is desirable to cool optical components. This is achieved using a cryogenic environment as the container of the detectors and readout electronics.

For POLARBEAR, the challenge lies in creating a compact cryogenic system of multiple components taking into consideration of aligning the cold optical chain with the reflective Gregorian-Dragone optics. The resulting design is the cryostat providing 3 main stages of cooling. A single pulse tube cooler (PTC) provides the 50K and 4K stages, while a He sorption fridge mounted off the 4K stage provides 0.25 K [10]. The enclosed optical elements are cooled to 50 K to meet the requirement that the optical chain contribution is minor compared to the power from the atmosphere in Chile [10]. The second stage cools the superconducting quantum interference device (SQUID) ammeters used for readout. In the final stage, a closed cycle three stage Helium sorption refrigerator cools the focal plane of detectors to under 0.25 K. Figure 2.3 shows the cross-section of POLARBEAR cryostat. In the following subsections, the main components will be introduced in the order that light, which enters the cryostat from the right, hits each one.

2.3.1 Filters and vacuum window

Light reflected from the secondary mirror enters the cold optical chain though the vacuum window of the cryostat. This window is made of zotefoam with a radius of 30cm. Zotefoam is an excellent thermal insulator, which has the advantage that the inner side of the zotefoam window is much colder than the outside (and emits less as a result). The achieved temperature of the window is approximately 150K, equivalent to a loading of $\sim 2W$. The loading is further reduced by a series of dielectric absorbers. A Mupor, which is a porous expanded teflon, reduces the temperature by 50K by absorbing the infrared radiation and transporting it out to the aluminum shell. Then, to reject photons outside the desired signal band, POLARBEAR uses polypropylene-substrated hot-pressed filters, commonly known as 'metal-mesh' filters, developed by the Cardiff group [72]. These filters can have metal grid structure patterns that can be used for high pass filters, low pass filters or band pass cases. In order to minimize the power requirements on the colder cryogenic stages, POLARBEAR uses a series of these filters

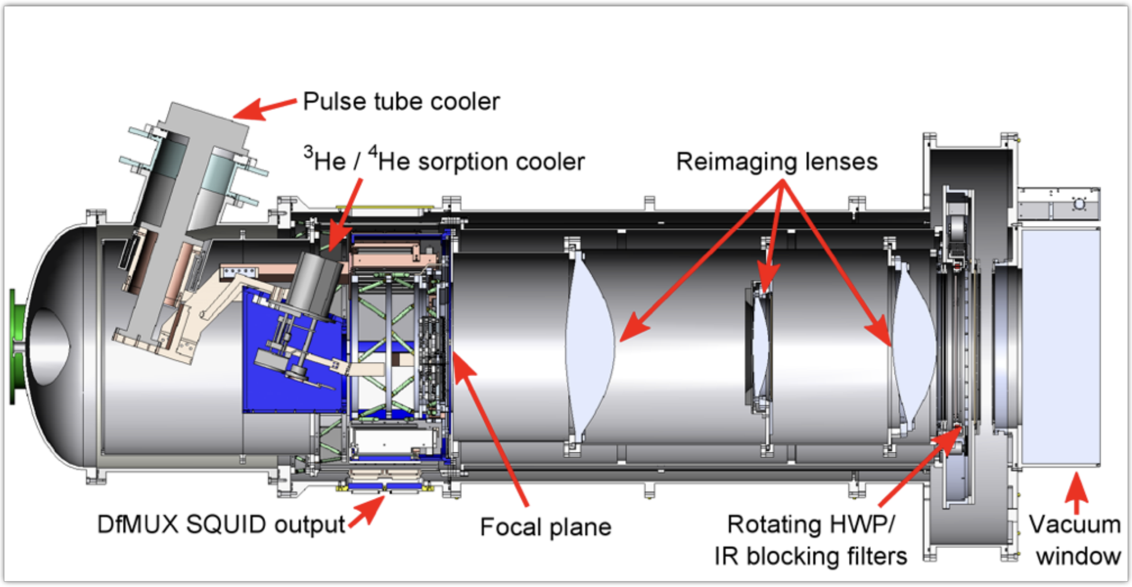

FIGURE 2.3: The cross-section of POLARBEAR cryostat. Light enters through the vacuum window on the right, traveling leftwards through the cryogenic re-imaging lenses to the focal plane. The pulse tube cooler provides cold heads at 50K and 4K. The focal plane is cooled to 250 mK using a He sorption cooler mounted off the 4K head. [Figure taken from [7]].

such that each blocks IR radiation from warmer stages. One 12 inverse centimeter (icm) filter is placed at the 50 Kelvin stage, one 15 icm at the entrance to the 4K optics tube, and 8.7 icm filter at the aperture stop skyward of the aperture lens [10]. The icm numbers specify the cutoff wavenumbers of the filters. The filter cutoffs are varied between each stage to prevent harmonic leaks. A final 5.7 icm filter is mounted before the focal plane cooled to 350 mK, reducing the loading to under the cooling capacity of $1\mu W$ of the subKelvin He sorption cooler [11].

2.3.2 Half wave plate

Half wave plate is an optical device that introduces a π phase delay between the two linear polarisations of light. This is typically done using birefringent material. POLARBEAR uses an anti-reflection coated single crystal sapphire HWP with a thickness of 3.1 mm [7]. This HWP is adapted to rotations in steps of 11.25 degrees in the cryostat. Over the POLARBEAR survey, two incarnations of the HWP have been used. Initially a stepped cryogenic HWP was used. While this stepped HWP achieved one goal of a HWP, mitigating instrumental polarisation systematics by rotating the polarisation direction of the sky signal relative to the instrument, it did not allow the signal band to be shifted out of the low-frequency noise. On the other hand, a continuously rotating half-wave plate can shift the polarisation signals to higher frequencies as an attempt to separate the signals from the 1/f noise dominating at low frequencies. This is important given that POLARBEAR 's goal is to observe a large sky area for large angular scales B-modes. As the engineering challenge of a cryogenic, continuously-rotating HWP was not solved in time, in 2014 a warm rotating HWP was installed between the secondary and primary mirrors. The cryogenic HWP is still kept stationary in the original place during the entire collection of data used for this thesis. Characteristics of the HWP and its main impacts on data modulation will be described in Chapter 3.

2.3.3 Reimaging optics

The reimaging optics consist of a cold aperture, and collimating lenses to direct the curved light path from the telescope to the focal plane. With this setting, the telescope gets a 2.3° diffraction-limited field of view for a 19cm focal plane. The lenses are wholly anti-reflection surface-coated with a single layer of porous polytetrafluoroethylene using a vacuum hot-press process and are cooled to $\simeq 6$ Kelvin to lessen their in-band emission [7].

2.3.4 Focal plane

Finally, the photons reach the focal plane. The POLARBEAR-1 focal plane consists of 1,274 transition edge sensor (TES) bolometers divided into seven wafers. The fabrication of focal plane components is done at the UC Berkeley Marvell Nanolab. A pair of bolometers is coupled to each slot-dipole antenna (one bolometer per polarisation). We will refer to each such pair as a focal plane pixel. For higher directivity, a hemispherical dielectric lenslet is attached to each antenna, thereby effectively augmenting the effective size of the antenna and improving the optical coupling to the telescope [73]. Lenslets are small lenses made of silicon of size $\sim 1cm$. The focal plane and elements for POLARBEAR-1 is shown in Figure 2.4.

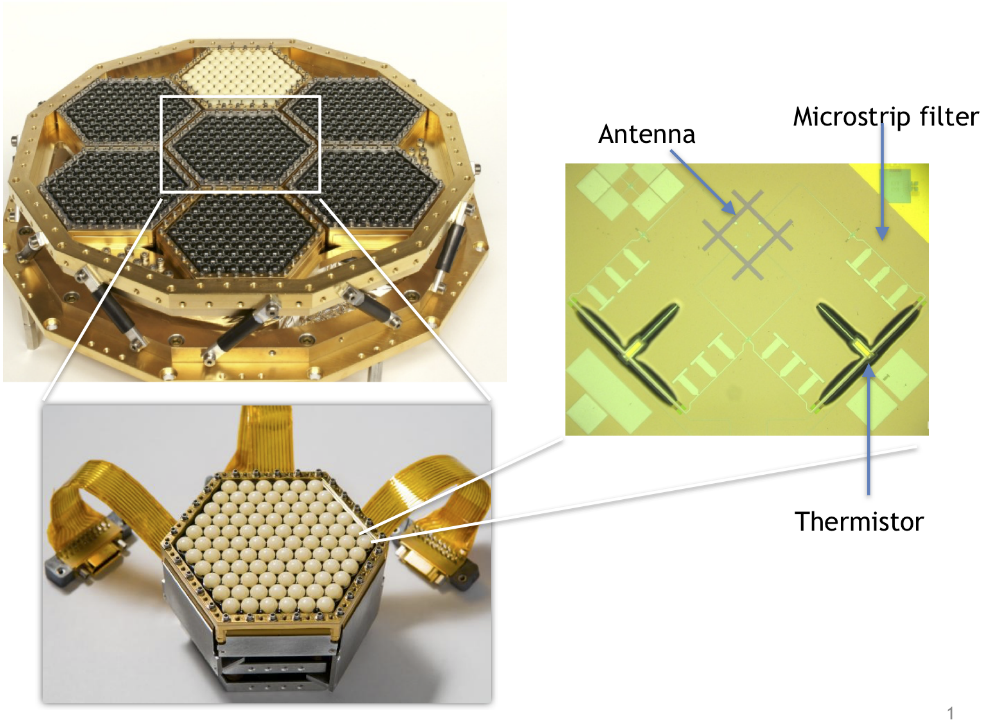

FIGURE 2.4: The focal plane, single wafer and single bolometer for POLARBEAR [7] The focal plane has 7 wafers. The hemisphere lenslets are visible on the wafers. Under each lenslet, one antenna is connected to 2 black thermistors via microstrip filter.

2.3.5 TES bolometers

Bolometers receive the optical power directed by the lenslet-coupled antennas. The respective current through the bolometer is read out to be used for data processing. A generic bolometer is a thermistor connected to a heat bath through a weak thermal link, as sketched in Figure 2.5. In this case, the thermistor is a voltage-biased superconductor, whose responsivity is roughly constant when the superconductor is tuned to a point close to the transition.

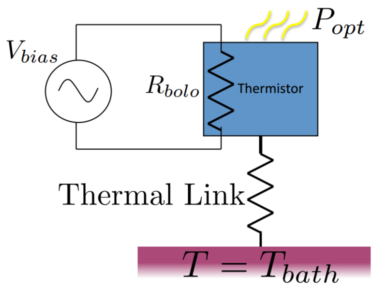

FIGURE 2.5: Simplified schematic for a bolometer. The bolometer is weakly coupled to a thermal bath (in the case of POLARBEAR, at 250 mK). Incoming power, whether optical (due to P_0) or electrical (due to V_{bias}), heats up the bolometer. The temperature of the bolometer is read out via the thermistor; for POLARBEAR the thermistor is a transition edge sensor (TES).

How a TES thermistor functions can be understood through a simplified model. The total heat power in the thermistor is comprised of the sky optical power P_0 and electrical bias power P_e. To maintain its responsivity at thermal equilibrium, heat is dissipated through a the thermal link to the bath as denoted by P_t. The energy balance equation for this is:

$$\frac{dE}{dt} = P_0 + P_e - P_t \tag{2.1}$$

with E - the bolometer energy. With the initial thermistor resistance R_0, and bias voltage V, the electrical power is

$$P_e = \frac{V^2}{R} \approx P_{e0} + \delta P_e = \frac{V^2}{R_0} - \frac{V^2}{R_0^2}\delta R \tag{2.2}$$

where δR is the change in the resistance which is positive with respect to temperature rise. Figure 2.6 shows an example of the response of a TES with respect to change of temperature.

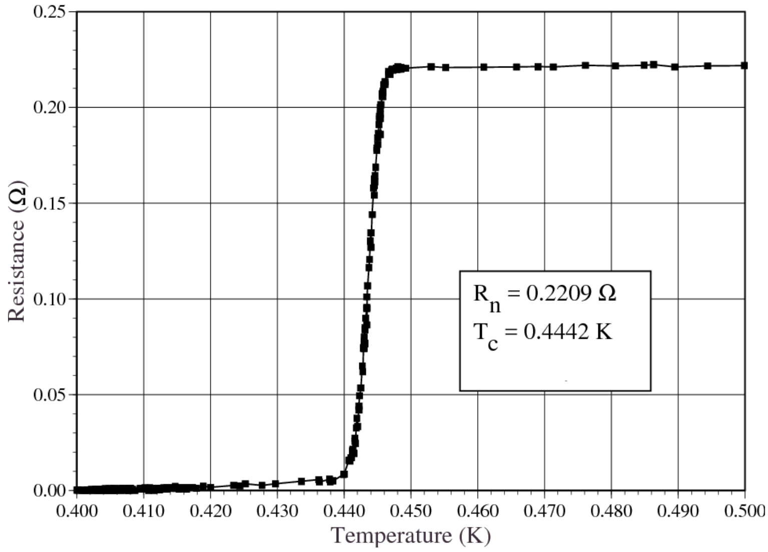

FIGURE 2.6: Example of the depence of the resistance of a TES on temperature. The resistance is approximately constant then undergoes a steep change in the transition width between temperatures 0.43K and 0.448K. After the transition, the TES resistance is approximately constant again. Figure is adapted from [8].

Equation 2.2 shows that the bolometer temperature is to be stabilised at close to the transition temperature T_c thanks to the negative feedback presented by the minus sign term. When the thermistor gains optical power, it is heated up, increasing the resistance and decreasing the bias power. This compensation thus keeps the total power and the temperature of bolometer constant. The negative feedback mechanism also sets the bias power to zero when a bolometer reaches the maximum detectable optical power threshold. This is important to prevent a system breakdown due to thermal loading exceeding the limit of the bolometers. The electrical current needed to maintain each TES at a fixed resistance is monitored through a SQUID.

2.3.6 Multiplexing

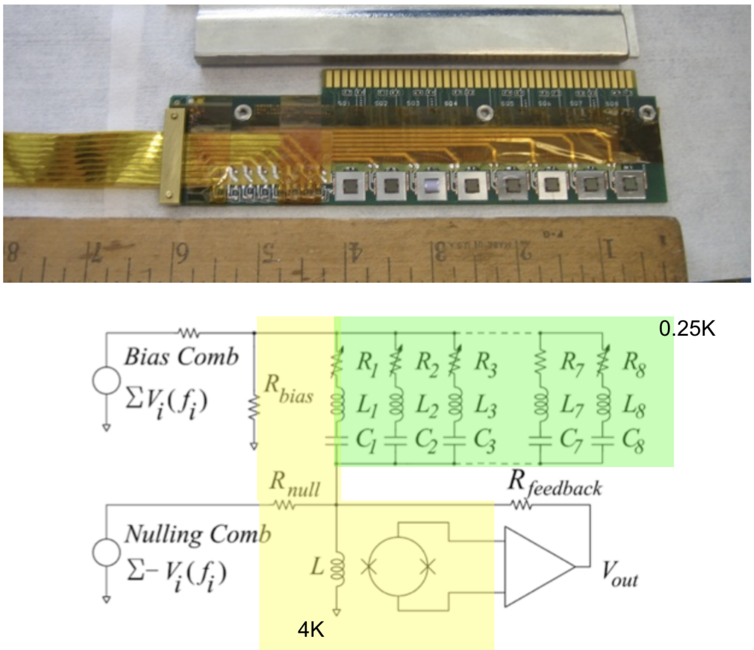

FIGURE 2.7: An eight-channel readout multiplexer: real fabrication and outlining. **Top panel:** A real fMUX board used in the POLARBEAR experiment. **Bottom panel:** A simplified circuit diagram illustrating the key aspects of the frequency-multiplexing (fMux) system. The fMUX system is based on sending a bias comb through a set of TES bolometers, mounted in parallel. An LC filter in series with the TES bolometer rejects bias current, except at the resonance of the LC circuit. Each LC filter is tuned to a different resonant frequency. This allows us to independently bias each TES bolometer by setting the current at its specific resonant frequency. The nulling comb serves to remove residual carrier signals before the current is amplified by a SQUID.

Running thousands of wires to the 250 mK stage to read out each bolometer would introduce a substantial heat load. Instead POLARBEAR uses an 8-fold multiplexing scheme to reduce the number of wires. POLARBEAR, like another experiment SPTpol, employs the frequency domain multiplexing (fMux) architecture developed at Berkeley. Alternative multiplexing technologies include time-domain multiplexing which has been developed by other research groups [74]. The actual Digital Frequency-Domain Multiplexing boards are designed by Polarbear collaborators at McGill University in Montreal [75]. Design using fMux is opted for POLARBEAR because each multiplexed set of detectors needs only one single cold SQUID array amplifier in this scheme. This helps to reduce cost and complexity as compared to time-domain technologies in which each detector uses a SQUID and each multiplexed set of detectors uses a SQUID array amplifier. The major disadvantages of the fMUX system are i) the complications and instabilities due to high frequency bias currents and stray impedances within the system and ii) instabilities due to bandwidth limitations. An outline of an eight-channel readout multiplexer is shown in Figure 2.7. In the fMUX scheme, each bolometer is biased at a different carrier frequency. As shown in Figure 2.7, each bias frequency is tied to its associated bolometer using the resonance of an LC circuit in series with the TES. The narrowness of this resonance sets how closely the bias carrier frequencies can be packed. A single SQUID can then read out a number of bolometers at once, with their signals separated in frequency space. Higher bias causes the SQUID response to be more sinusoidal. The corresponding harmonic distortion is partially offset with the negative feedback bias loop. A nulling comb is added to mitigate residual carrier signals via destructive interference [75]. This serves to counter the limited dynamic range of the SQUID.

2.4 Observation strategy

2.4.1 Observation regions

POLARBEAR has observed from 2012 to today, a total of five seasons so far. Observations in the first and second season from 2012 to early 2014 targeted lensing B-modes. Three sky patches each with an area of 9 square degrees each were observed. The patches are called RA23, RA12 and RA4p5 after their right ascension positions. All 3 patches need to be separated in RA so that they are observable at different times of the day. The locations of patches were chosen to overlap with previous experiments: RA23 and RA12 overlap with patches of the Herschel ATLAS survey at submillimeter wavelengths while RA4p5 matches with one of the QUIET survey fields. The patch overlapping the H-ATLAS field has already been used in a cross-correlation analysis between the Herschel maps and POLARBEARs CMB lensing reconstruction maps. In July 2014, POLARBEAR shifted to a large survey area, optimised to detect primordial B-mode signal at large angular scales instead of simply detecting B-mode power. This larger survey region also enables the E-mode power spectrum measurement of this thesis. The observed large patch is centered at (RA, DEC)=(0,-57.5) degrees with an area of over $600\,\mathrm{deg}^2$. This larger survey region is also important as the larger area significantly reduces the sample variance on the E-mode power spectrum measurement of this thesis.

The location of the patches on the sky are roughly noted in Figure 2.8. All patches are intended to lie in sky regions with significantly low dust - the reference for the dust map is produced by [9]. The declination of the patches were appointed to have maximal time of observation for the patches. To sufficiently minimise airmass and subsequently atmospheric contamination, observations are done when patches rise well above the horizon . In parallel, the patches cannot be observed when too high in elevation because sky scan speed would exceed the maximum azimuth speed of the telescope.

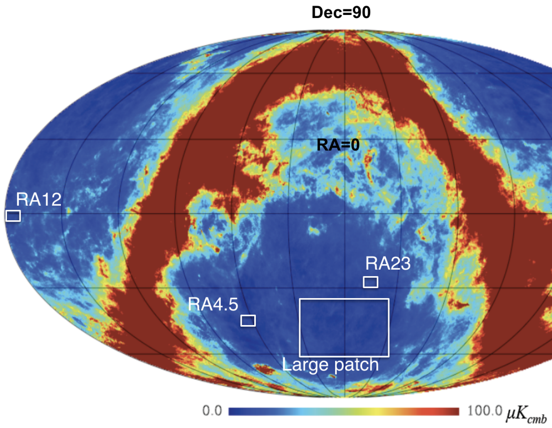

FIGURE 2.8: The POLARBEAR patches (white boxes) are overplotted on a map of the galactic dust emission at 100 μm from Schlegel et al. [9]. By design, the POLARBEAR survey regions avoid the galactic plan and focus on regions of extremely low dust emission.

2.4.2 Constant Elevation Scans

Constant Elevation Scans (CES) are employed by POLARBEAR to observe the CMB. At constant elevation, the telescope scans back and forth between left or right directions with a constant velocity in about 15 minutes such that the telescope can observe the entire targeted region of a patch before it moves away. For small patches, the targeted region can be the entire patch. The large patch is, however, divided into 4 small targeted regions with about 7.5 degrees in right acsension. Each sweep is defined as a subscan, and one CES consists of 100-200 subscans for small patch and about 71 for large patch. Data taken when the telescope accelerates and reverses its direction are removed from analysis because those movements introduce spikes and glitches in the data.

Scan-synchronous noise sources or ground pickup will be fixed in the Az-el plane. Scan synchronous signals are separated from true CMB signals by the rotation of the earth, which effectively rotates sky signals in the AZ-EL plane. An exception is if CMB polarisation modes appear constant in the right ascension direction, they cannot be differentiated from scan synchronous signals. These modes are rejected in data analysis. In addition, the latitude of the site leads to the rotation of orientation of the patches with respect to the telescope as the patches rise and set. This allows the telescope to scan across sky patches from different angles through the length an observation, helping to average out systematic effects that would otherwise cause greater contamination in the data. The orientations of scan synchronous signals and true CMB signals are illustrated in Figure 2.9, which also shows how the sky rotation helps to suppress the pickups.

POLARBEAR is pushed towards faster scan speeds by the desire to shift the CMB signal to higher frequencies that are less affected by 1/f instrumental noise. The scan

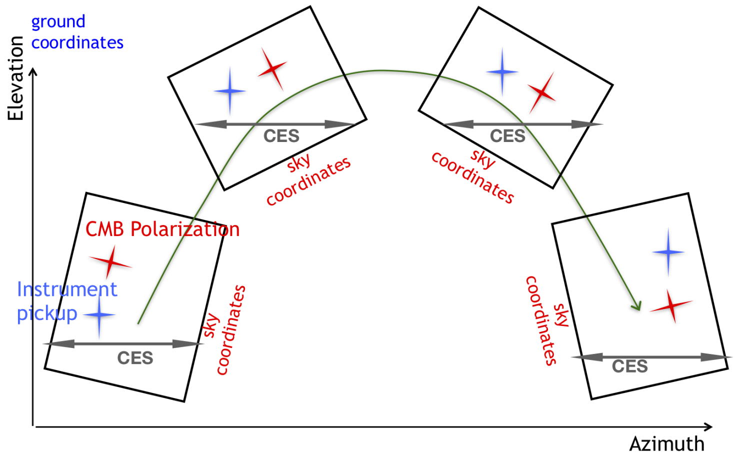

FIGURE 2.9: An illustration of the POLARBEAR scan strategy, and how sky rotation can help disentangle instrumental and CMB polarization. The black arrows show the constant elevation scans (CESes) used by POLARBEAR as the field drifts (clockwise) past. Once the field has moved out of sight, the telescope elevation is adjusted to track the field, and a new CES is started. Over the course of time, instrumental polarization effects (blue crosses) will remain fixed in ground coordinates, while the true CMB polarization which is fixed in sky coordinates, will rotate with respect to the ground coordinates.

speed is however limited by the turnaround time, which is in turn subjected to both the maximum acceleration of the HTT, and the response time of the controlling servo. In experience, too high speed can spike the turnaround, causing undesired jerking motion of the telescope, leading to unwanted noise. The telescope is set to have a constant velocity of $0.4°/s$, the span is 20° for the low elevation and 35° for the low elevation. The lowest elevation of CES observations is chosen to be 30°. One hour long CES only covers a fraction of the targeted sky patch, and 10 days of observation are needed to cover the whole patch. Data selection described in 5.2 can remove observations and reduce the achieved coverage of 10 days of observation.

2.4.3 Overall scan planning

For POLARBEAR, a science observation is constituted of continuous blocks of scans observing one patch for the day. One observation course lasts typically eight hours to take advantage of the duration a patch rises and stays above the 30° horizon and under the 80° elevation.

Each one-hour scan block consists of a series of critical scans, starting with detector tuning, then observations for calibration, constant elevation scans, then observations for calibration again. The scans for calibration include stares of a hot calibration source and elevation nodding scans where the telescope nods up and down. These 2 types of scans are called stimulator scans and elnod scans respectively. Both of these are meant to interpolate linearly individual detector gains across the hour and will be described in 4.5.

Other observed astrophysical objects are the Crab Nebula, Saturn and Jupiter in all 5 seasons, and additionally Mars and Venus in the first 2 seasons. Scans of the Crab Nebula are used for the calibration of the relative polarisation angle of the detectors. Scans of the planets are mainly for detector gains, with Jupiter for beam calibration in addition. Calibration of beam, detector gain and polarisation angle will be discussed in Chapter 3.

Chapter 3

Continuously rotating Half-wave Plate

This chapter describes an important element in the optical chain, the continuously rotating half wave plate, and some related effects that are most present in later stages of the analysis done for this thesis. As mentioned in Chapter 2, for all observations of the sky patch of over $600\,\mathrm{deg}^2$, POLABEAR has a continuously rotating half wave plate (CRHWP) installed at the prime focus between the primary mirror and the secondary mirror. The sketch of the position of this CRHWP can be found in [76]. The CRHWP modulates the polarisation signal received by the detectors, shifting the signal to higher frequencies less affected by low frequency noise. We thus look into basic properties of the half wave plate and its effects on the data models.

3.1 Half wave plates

A half wave plate (HWP) is an optical component made of birefringent material that rotates the polarisation components of light passing through it. By using materials with different indices of refraction along 2 axes in the plate plane, the HWP can induce phase difference ϕ for the electric field components along those axes as shown in Figure 3.1. The phase delay is $\phi = \pi$ for an ideal half wave plate:

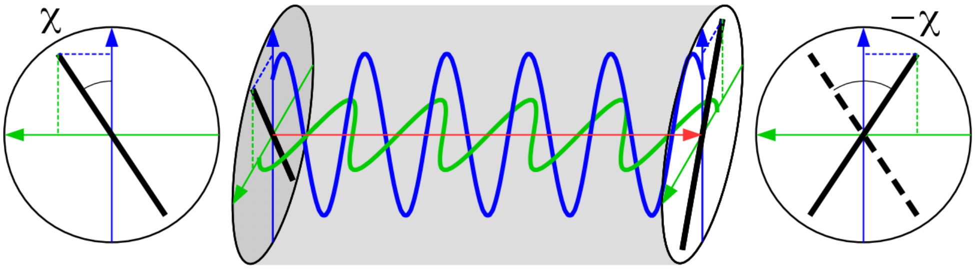

FIGURE 3.1: The signal, denoted by the black vector is rotated by an angle ϕ after passing through the HWP. The green and blue axes are respectively the horizontal axis and vertical axis of the HWP. The dash vector on the right hand side denotes the original signal orientation. The χ and $-\chi$ denotes the amplitude of the signal mirrored with respect to the vertical axis.

The effects of HWP on Stokes components are shown in Figure 3.2. Picture credit: Satoru Takakura.

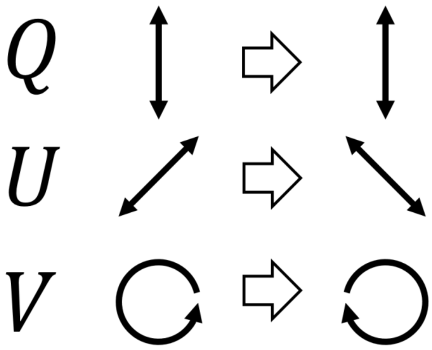

FIGURE 3.2: How a HWP changes the Stokes parameters I, Q, and U. Picture credit: Satoru Takakura

As shown in Figure 3.1, the polarisation orientation is mirrored about the axis, hence:

$$\begin{aligned} E_x &= E_x \\ E_y &= -E_y \end{aligned} \tag{3.1}$$

Using this with Equation 1.29, and expressing the effect of the HWP through Mueller matrix action on Stokes vectors $S_{out} = MS_{in}$, we have for an ideal HWP:

$$M_{HWP} = \begin{pmatrix} 1 & 0 & 0 & 0 \\ 0 & 1 & 0 & 0 \\ 0 & 0 & -1 & 0 \\ 0 & 0 & 0 & -1 \end{pmatrix} \tag{3.2}$$

If we now rotate the HWP as a function of time, polarisation signals will be modulated. Combining 3.2 with Equation 1.30, we have the matrix for coordinate rotation:

$$R = \begin{pmatrix} 1 & 0 & 0 & 0 \\ 0 & cos(2\theta_{HWP}) & -sin(2\theta_{HWP}) & 0 \\ 0 & sin(2\theta_{HWP}) & cos(2\theta_{HWP}) & 0 \\ 0 & 0 & 0 & 1 \end{pmatrix} \tag{3.3}$$

where θ_{HWP} is the angle of rotation in the plane of the HWP. The complete Mueller matrix of a rotating ideal HWP whose birefringent axes form θ_{HWP} with respect to the coordinate system used to define light is:

$$M_{rotHWP} = R(-\theta_{HWP})M_{HWP}R(\theta_{HWP}) = \begin{pmatrix} 1 & 0 & 0 & 0 \\ 0 & cos(4\theta_{HWP}) & sin(4\theta_{HWP}) & 0 \\ 0 & sin(4\theta_{HWP}) & -cos(4\theta_{HWP}) & 0 \\ 0 & 0 & 0 & -1 \end{pmatrix} \tag{3.4}$$

This shows that only Q and U are rotated with dependence on 4 times HWP angle, while I (and V) are intact.

3.2 Simplified Data Model

Given that the circular polarisation V is typically not measured by CMB experiments because V polarisation is not generated in the Standard Cosmological Model, the data model should contain I,Q, and U and the terms that represent the effects by optical components. In practice, we also consider the orientation of the detectors θ_{det} with respect to a common frame of measurement. Detector angles do not rotate, so the output signal can be written as:

$$d = I_i + Q_i cos(4\theta_{HWP} - 2\theta_{det}) + U_i sin(4\theta_{HWP} - 2\theta_{det}) \tag{3.5}$$

For a HWP continuously rotating at angular velocity ω_{rot}, the HWP θ_{HWP} evolves as:

$$\theta_{HWP}(t) = \omega_{rot} t$$

where we have defined the initial angle to be zero. Thus, a DC polarisation signal would show up at $4\omega_{rot}$, 4 times the HWP rotation frequency. A signal at frequency f_0 will show up at $4\omega_{rot} \pm f_0$. This separates the low frequency signal from the low frequency instrument or atmospheric noise.

Since signals have been modulated by the HWP, an important step is to demodulate the data registered by detectors. Importantly, intensity signal I_i does not rotate with the HWP, so the observed intensity I_o can be recovered with a low-pass filter, LPF as:

$$I_o(t) \equiv LPF[d(t)] \approx I_i(t) \tag{3.6}$$

The polarisation signals Q_o and U_o are retrieved by doing a band-pass filter around the modulation frequency and reverting the terms of the HWP and detector angles:

$$Q_o(t) + iU_o(t) \equiv BPF[d(t)] \times 2e^{4i\theta_{HWP} - 2i\theta_{det}} \approx Q_i(t) + iU_i(t) \tag{3.7}$$

3.3 Practical instrumental effects

The equations above correspond to perfect CRHWPs. However, real CRHWPs have imperfections. Due to the rotation of the CRHWP, the parasitic signals are expected to vary with the angle of the HWP. These HWP synchronous signals (HWPSS) can be Fourier expanded as:

$$A_{HWPSS}(t) = \sum_{n=1} Re[A_n(t)e^{-i\mathbf{n}\theta_{HWP}(t)}], \tag{3.8}$$

where **n** names the order of the harmonics, A_n is the amplitude at the respective harmonic. Key optical imperfections that contribute to this expansion will be described, and followed by other non-idealities most relevant to the data calibration and processing for this thesis.

3.3.1 Non-ideal transmission properties of the Half Wave Plate

For non-ideal HWPs, we have to account for different transmissivities for the polarisations along the HWP birefringent axes besides the phase delay ϕ between the polarisation components. On denoting the transmitivities as ρ_x and ρ_y, outgoing electric field from Equation 1.28 are then modified:

$$\begin{aligned} E_x &= E_{x0}\rho_x \\ E_y &= E_{y0}\rho_y e^{i(\phi)} \end{aligned} \tag{3.9}$$

Since amplitude transmitivities and phase difference also depend on the frequency ν of passing light, the modified Mueller matrix is:

$$M_{HWP} = \begin{pmatrix} a_T(\nu) & b_T(\nu) & 0 & 0 \\ b_T(\nu) & a_T(\nu) & 0 & 0 \\ 0 & 0 & -c_T(\nu) & s_T(\nu) \\ 0 & 0 & -s_T(\nu) & -c_T(\nu) \end{pmatrix} \tag{3.10}$$

with:

$$\begin{aligned} a_T(\nu) &= (\rho_x^2 + \rho_y^2)/2 \qquad b_T(\nu) = (\rho_x^2 - \rho_y^2)/2 \\ c_T(\nu) &= \rho_x \rho_y cos(\phi(\nu)) \qquad s_T(\nu) = \rho_x \rho_y sin(\phi(\nu)) \end{aligned} \tag{3.11}$$

Here, $a_T(\nu)$, $b_T(\nu)$ respectively correspond to the total transmittance of the HWP and the transmittance difference between 2 HWP axes. $c_T(\nu)$ plays in the HWP polarisation efficiency.

Non-ideal HWPs also absorb and emit polarised light following the fluctuation-dissipation theorem [77]. The corresponding Stokes vector from the HWP is:

$$S_{HWP}(\nu) = (1 - a_A(\nu), -b_A(\nu), 0, 0)I_{HWP},$$

where $1 - a_A(\nu)$ denotes the HWP absorptance, $b_A(\nu)$ denotes its anisotropy, and $I_{HWP}(\nu)$ represents the blackbody radiation at the HWP temperature. The output optical signal into the detector now includes terms from the HWP emission [78]:

$$\begin{aligned} P_{out} &= \langle a_T \rangle I_{in} + \langle 1 - a_A \rangle I_{HWP} + Re\left[\tfrac{\langle a_T - c_T \rangle}{2} (Q_{in} - iU_{in}) e^{2i\theta_{det}} \right] \\ &+ Re\left[\langle b_T \rangle (Q_{in} + iU_{in}) e^{-2i\theta_{HWP}} \right] + Re\left[(\langle b_T \rangle I_{in} - \langle b_A \rangle I_{HWP} - i\langle s_T \rangle V_{in}) e^{-2i\theta_{HWP} + 2i\theta_{det}} \right] \\ &+ Re\left[\tfrac{\langle a_T + c_T \rangle}{2} (Q_{in} + iU_{in}) e^{-4i\theta_{HWP} + 2i\theta_{det}} \right] \end{aligned} \tag{3.12}$$

Coefficients in angle brackets are frequency band average and can be derived by averaging values through the frequency band $f_{det}(\nu)$ using the source spectrum of the band as weights i. e. [79]:

$$\langle a_T \rangle = \frac{\int a_T(\nu) I_{in}(\nu) f_{det}(\nu) d\nu}{\int I_{in}(\nu) f_{det}(\nu) d\nu} \tag{3.13}$$

Equation 3.12 shows that the non-ideality of the HWP contributes to the second harmonics ($\mathbf{n} = 2$) in 3.8. The transmission of the HWP, $\mathfrak{I}$, and the polarisation efficiency, ϵ, are defined by:

$$\mathfrak{I} = \langle a_T \rangle; \epsilon = \langle \frac{a_T + c_T}{2a_T} \rangle \tag{3.14}$$

Equation 3.12 shows the additional polarised signal that appears at $2\theta_{HWP}$ besides the polarised signal at $4\theta_{HWP}$. These terms are modulated by twice the HWP frequency f (or $\mathbf{n}$ times the HWP frequency in general) will be referred to as $2f$ ($\mathbf{n}f$) terms hereafter. The output signal is mainly contributed to by the intensity and the polarisations at $4\theta_{HWP}$:

$$P_{out} = \Im(I_{in} + Re[\epsilon(Q_{in} + iU_{in})e^{-4i\theta_{HWP}+2i\theta_{det}}]) \tag{3.15}$$

3.3.2 Non-ideal primary mirror

Between the POLARBEAR HWP and sky is the primary mirror. As the mirror also absorbs a little of light and cause phase delay, the Mueller matrix for the mirror action is identical to 3.10 of the HWP, but for the mirror transmisivity $a_m(\nu)$ and the asymmetry in transmissitvity $b_m(\nu)$. The emissivity of the mirror is $1 - a_m(\nu)$. The signal including only the spurious terms from the mirror is [78]:

$$\begin{aligned} P_{out} &= \langle a_m \rangle I_{in} + \langle 1 - a_m \rangle I_{mirror} + Re[\langle b_m \rangle (Q_{in} + iU_{in})] \\ &+ Re\Bigg[(\tfrac{\langle a_m + c_m \rangle}{2}(Q_{in} + iU_{in}) + \tfrac{\langle a_m - c_m \rangle}{2}(Q_{in} - iU_{in}) \\ &+ \langle b_m \rangle I_{in} - \langle b_m \rangle I_{mirror} - i\langle s_m \rangle V_{in})e^{-4i\theta_{HWP}+2i\theta_{det}} \Bigg] \end{aligned} \tag{3.16}$$

where $\langle c_m \rangle$ and $\langle s_m \rangle$ are defined from a_m and a_m similarly as in 3.11. Equation 3.16 shows so the mirror induces an intensity-to-polarisation leakage that is modulated to $4\theta_{HWP}$ (or $\mathbf{n} = 4$) but does not contribute any term of $2\theta_{HWP}$ ($\mathbf{n} = 2$) in 3.8.

3.3.3 Other non-idealities

Both the surfaces of the HWP have anti-flection (AR) coating to mitigate bouncing lights between elements. However, the AR coating of the HWP is found to be non-uniform with a small air bubble. The additional signal from this spot is expected to depend on the rotation angles like the HWP. Denoting A_{spot} the amplitude of the signal from the HWP spot, we can Fourier expand the output from this signal as:

$$P_{spot} = \sum_{n=1} Re[A_{spot} e^{-i\mathbf{n}\theta_{HWP}}], \tag{3.17}$$

This signal appears in all modes, but the amplitudes are found to be most significant for $\mathbf{n} = 2$ and $\mathbf{n} = 4$ when calculated for estimation of systematic errors from the spot in 6.4.7.

3.3.4 Detector response

Practical detector response is a convolution of the incoming power at time t with a time-dependent response function $G(t')$:

$$d(t) = \int_0^\infty dt' G(t') P_{in}(t - t') \tag{3.18}$$

For simplicity, $G(t')$ depends on g, the responsitivity of the detector, and τ, the time constant.

$$G(t) = \begin{cases} g\frac{e^{-t/\tau}}{\tau} & \text{for} \quad t > 0 \\ 0 & \text{for} \quad t < 0 \end{cases} \tag{3.19}$$

For signals that vary slowly with respect to the time constant i.e. the instantaneous transfer of approximately constant signals, the detector response can be further simplified:

$$d(t) \approx g P_{in}(t - \tau) \tag{3.20}$$

Individually, the imperfect responsivity and the time constant alter the detector signals as followed.

3.3.4.1 Time constant delay

Considering only the intervention of time constant, the detector signal is altered due to the retardation of the register of rotating HWP angle as:

$$d(t) = I_{in} + Re[(Q_{in} + iU_{in})e^{-4i\theta_{HWP}(t-\tau)+2i\theta_{det}}] \tag{3.21}$$

where $\theta_{HWP}(t) = \omega_{rot}t$. The output polarisation signals differ from the true values by:

$$(Q_{in} + iU_{in})e^{4i\omega_{rot}\tau} \tag{3.22}$$

Estimation of time constant is done using stimulator measurements and described in 4.5.2. The median time constant of POLARBEAR detectors is $2.5ms$. The HWP rotating frequency is thus low enough for the corresponding cut-off frequency of the detectors ($64Hz$).

3.3.4.2 Detector non-linearity.

In addition, the time constant of the detector and responsivity has non-linear variations due to temperature variations of the detector, dynamic range of the detector, SQUID gain etc. These variations can be represented by their dependence on the incoming signal.

Expanding the dependence of the time constant and responsivity on the registered input power in Taylor series, we expect the zero-th order and first order terms will contribute most significantly:

$$g(P(t)) = g^{(0)}_{|P} + g^{(1)}_{|P}\Delta P(t) + ..., \tag{3.23}$$

$$\tau(P(t)) = \tau^{(0)}_{|P} + \tau^{(1)}_{|P}\Delta P(t) + ..., \tag{3.24}$$

Assuming all other factors are idealised and using Equation 3.20, the detector signal can be written as [78]:

$$\begin{aligned} d(t) &= (g^{(0)} + g^{(1)})I_{in}(t))Re[A_4^{(0)}e^{-4i\theta_{HWP}(t)}] \\ &= g^{(0)}Re([A_4^{(0)} + \tfrac{g^{(1)}}{g^{(0)}}A_4^{(0)}]e^{-4i\theta_{HWP}(t)} \end{aligned} \tag{3.25}$$

where $g^{(0)}$ and $g^{(1)}$ are the zero-th and first order terms in the Taylor expansion of responsitivity dependent on the small devidation of P_{in} of the detector. The term $A_4^{(0)}$ represents the HWPSS amplitude dependent on the intensity signal that appears in the polarisation. Equation 3.25 shows that the leakage of the intensity signal creates the non-linearity of the detector gain $g(t)$ that is coupled with polarisation term $A_4^{(0)}$, causing the overall variation of measured polarisation signals. Assuming the HWPSS causes the same variation of responsivity, the leakage coefficient due to non-linear responsivity given by:

$$\lambda_4^g = \frac{g^{(1)}}{g^{(0)}}A_4^{(0)} \tag{3.26}$$

Since time constant delay adds spurious term to the polarisation signal, the coefficient for non-linearity of the time constant can be given as [78]:

$$\lambda_4^\tau = i\omega_{rot}\tau A_4^{(0)} \tag{3.27}$$

3.3.5 1/f noise

As a ground-based CMB experiment, POLARBEAR undergoes heavy intervention from the the atmospheric fluctuation, which is the main component of 1/f noise. The reason why it is called 1/f noise is that the evolution of distributions of characteristics of a state of turbulence of the atmostphere i.e. the density, temperature, or humidity can be described by the temporally logarithmic spectra [80]. The noise scanned from this logarithmic distributions is logarithmic noise, and thus called 1/f noise. Since the atmospheric fluctuation is well-approximated to be unpolarised [81, 82], we have opted to use the HWP to mitigate this source of noise. Stokes parameters coming from sky having atmospheric noise *atm* can be simply modified as:

$$
\begin{aligned}
I_{in}(t) &= I_{sky}(t) + \delta I_{atm}(t) \\
Q_{in}(t) &= Q_{sky}(t) + \delta Q_{atm}(t) \\
U_{in}(t) &= U_{sky}(t) + \delta U_{atm}(t)
\end{aligned}
\tag{3.28}
$$

Since the intensity signal is not modulated by the HWP, the I component is heavily contaminated by $\delta I_{atm}(t)$. While $\delta Q_{atm}(t)$ and $\delta U_{atm}(t)$ are highly suppressed for the polarisation as compared to for the intensity, their order of magnitudes is still significantly challenging. In addition, since there is leakage from I to P, which raises the overall contribution of atmospheric noise to polarisation measurement. The threshold that we strive to for this noise is under bolometer white noise.

3.4 Summary of HWP treatments

In this chapter, I have reviewed the HWP and presented a model to described the HWP-modulated data collected by POLARBEAR. I presented the major sources of systematic errors due to imperfections in the HWP. The $4f$ is expected to be the dominant term compared to the $2f$ because, following 3.16, it remains in the polarisation signal even after band pass filter and perfect demodulation. The leakage from the primary mirror is estimated in [76], and the leakage from the HWP is assumed to be significantly below. The total coefficient for leakage from intensity to polarisation is [76]:

$$
\lambda_4 \equiv \lambda_4^{opt} + 2r^{(1)} A^{(0)}_{4|\langle I_{in}\rangle} + i\omega_{rot}\tau A^{(0)}_{4|\langle I_{in}\rangle} \tag{3.29}
$$

where λ_4^{opt} is the optical instrumental leakage coefficient, $2r^{(1)} A^{(0)}_{4|\langle I_{in}\rangle}$ is shortened from 3.26, and $i\omega_{rot}\tau A^{(0)}_{4|\langle I_{in}\rangle}$ is taken from 3.27. The term $A^{(0)}_{4|\langle I_{in}\rangle}$ means that this amplitude is estimated at the averaged incoming intensity $\langle I_{in}\rangle$. These 3 contributing coefficients are assumed to be insignificant and thus only estimated to the first order. The time-ordered data that contains the total intensity leakage after HWPSS subtraction and demodulation are given as [76]:

$$
d'_d(t) = \epsilon[Q_{in} + iU_{in}(t)] + A^{(0)}_{4|\langle I_{in}\rangle} + \lambda_4 \delta I_{in}(t) + N_d^{(Re)}(t) + iN_d^{(Im)}(t) \tag{3.30}
$$

where N_d is the white noise. Estimation of the leakage coefficients can be done using the model 3.30 and has been described by [76]. The leakage from optical instruments is measured to be $\leq 0.1\%$. The detector non-linearity is measured to be $\leq 0.4\%$, contributing mainly to the total leakage. This percentage of leakage due to detector non-linearity shows that the HWP rotating frequency is sufficiently fast compared to the variation of the gain and time-constant. A higher HWP frequency can reduce this leakage term but may increase the temperature of the HWP, yielding higher HWP-related spurious signals.

Overall, systematics effects can be estimated by using simplified data model 3.5 as a basis for the simulation of timestream and injecting spurious signals of the corresponding systematics. The variation of the polarisation amplitude (or the $4f$ term) is coupled to effects from detectors: time constant and non-linear responsivity. The overall variation in the polarisation signal is thus used as a tracer of HWP related systematic effects. While the leakage of the $2f$ is not measured, the impact of the $2f$ is estimated on the output spectra by assuming the upper limit of the $2f$ leakage percentage to be the same as for $4f$. Estimations of all systematics are presented in Chapter 6.

The atmospheric noise is not considered as a systematic, but is nevertheless a prominent source of noise in POLARBEAR data. The atmospheric noise in the intensity timestream is significantly larger than in the polarisation timestream. The fraction of leakage of intensity atmospheric term to polarisation is estimated to be $\leq 1\%$ [83].

Since the leakage of intensity to polarisation is found to be small, we add white noise N_d to the simplified detector signal model for simulations where the white noise floor is assumed to represent the atmospheric noise that we cannot mitigate even with CRHWP.

Chapter 4

Data pre-processing

4.1 Overview

CMB light goes through the outer optical system, arrives in the cold hardware, and gets registered as time ordered data by the readout. While CMB measurements are the central subject of this experiment, we need to calibrate the instrument to minimise bias to final results. This is done by establishing data models and relevant viable measurements to investigate properties of the instruments.

Four properties to be calibrated include individual detector pointing (Section 4.3), detector relative gain (Section 4.5), the beam model (Section 4.4), and detector polarisation angle (Section 4.6). Overall, each section of calibration has been reprocessed multiple times to ensure consistency and to fully check the effects of external conditions such as weather. Since the stored data now comprise both CMB data and calibration data, the total volume is gigantic. With the installation of the HWP, data observed have been modulated and so would add extra computational memory cost to run main analysis if kept as is. Hence, we need to downsample and demodulate data first.

4.2 Downsampling and demodulation

The data is demodulated and downsampled in a joint operation of 2 steps coupled with each other in pre-processing. The data model is previously described in Section 3.2. We demodulate the timestream following [84, 85] and separate the data timestream into intensity and polarisation components. Since demodulation is done both on CMB data, which is most essential to this thesis, and calibration scan data, I will describe the main operation steps here and note some differences between the operations for the CMB data and calibration data.

A simplified model of the TOD modulated by a CRHWP is shown earlier in 3.4. In the telescope frame, the detector receive raw input TOD of the form:

$$\begin{aligned} d_m(t) = I(t) + \varepsilon \mathrm{Re}\{[Q(t) + iU(t)]\, e^{-i(4\theta_{HWP}+2\theta_{\mathrm{det}})}\} \\ + A(\theta_{HWP}, t) + \mathcal{N}_m, \end{aligned} \tag{4.1}$$

Here, HWP angle θ_{HWP} is reconstructed from the encoder; $A(\theta_{HWP}, t)$ is the HWP-synchronous signal earlier introduced in 3.3. The terms $e^{-i4\theta_{HWP}}$, ε, θ_{det}, and $\mathcal{N}_m$ denote the polarisation modulation of the HWP, a polarisation efficiency, the detector angle with respect to instrument coordinates, and the detector white noise respectively.

Before demodulation, the CES scans of CMB data are first subjected to the fast-glich-cutting step of data selection 5.2, while this step is not done the calibration data. The HWP-synchronous signal is first estimated following [84] and summarised as followed. There are gaps in the CES TOD due to subscan removals resulted from the glitch cut stage, and these gaps are filled with the HWP synchronous structure before overall removal. Estimation of the HWPSS is done following [85] using the CRHWP angles reconstructed from the encoder. The HWPSS consists of several harmonics related to the number of times of the HWP rotating frequency $n \in \{1, 2, .., 7\}$. The dependence of these harmonics on time is formed by bandpass filtering the TOD at those frequencies then demodulating the bandpassed TOD. The amplitude of each harmonic is also fit with a linear drift to get the final harmonic template. These templates are summed together then subtracted from each TOD. This harmonic subtraction process is then repeated.

After HWP structure removal, the polarisation signal is multiplied with the demodulation function $e^{4i\theta_{HWP}-2i\theta_{det}}$ and low pass filtered at $3.8Hz$ to become as in 3.30. We opt for this frequency band because there are two $0.2Hz$ sidebands at $4Hz$ - twice the CRHWP frequency. A cut-off frequency at exactly 4Hz would leave spurious signals in polarisation timestreams due to imperfect demodulation. In addition, a low pass filter at $3.8Hz$ gives a corresponding explorable maximum multipole $l = 4,560$ for CMB data.

After the low-pass filtering, timestreams are downsampled by a factor of 24, from the native recording frequency of $190.73Hz$ down to $\sim 8Hz$. For real CMB data, we store the polarisation TOD, the intensity component called the $0f$, and the $2f$ TOD. The $2f$ components are stored primarily for sanity checks of processed TOD through the null tests in 6.3 since there are spurious signals from the $2f$ that can appear in the demodulated polarisation TOD as described in 3.3.

The polarisation TOD need further correction due to HWP modulation coupled with other effects (see 3.3.4.1). First, the phase of the modulated polarisation signal is retarded by the time-constant of the detector by $\sim 9°$. The time constant also changes the detector response to the signal by $\sim 1\%$. Measurements of time constant, τ, is described in Section 4.5.2. We correct for the finite time constant by multiplying the polarisation component with the factor equal to inverse of the effect, $(1 - i\omega\tau)$. Second, individual detector angle orientation, θ_{det}, and the origin of HWP angle encoder, θ_0, need to be corrected for. We thus modify the encoded HWP angle by the factor, $e^{2i\theta_{det}+4i\theta_0}$. Measurements of detector angle θ_{det} and θ_0 are described in section 4.6 and in [86]. For CMB science data and polarisation angle calibration data, time constant deconvolution is done in the mapmaking stage. For other calibration scans, this step is done before model fitting.

The intensity-to-temperature leakage subtraction does not belong to this pre-processing stage but is noted here due to its usage in polarisation angle calibration. We do the leakage subtraction for CMB data in both the data selection stage 5.2 and the mapmaking stage 5.3. The mapmaking for polarisation angle calibration also involves this step. This operation is not relevant to other types of calibration scans because the respective calibrations do not use polarisation TOD.

The difference between before demodulation and after demodulation plus temperature leakage subtraction for the averaged PSDs of a single CES is shown in Figure 4.1 . The PSD before demodulation consists of I, Q and U components, the leakage from the intensity, and the HWPSS and can go over the frequency of $10Hz$. The 'after demod.' PSDs are cut off at $3.8Hz$. The spike at $4f = 8Hz$ in the comprehensive PSD line becomes the spikes at $1f = 2Hz$ in the Q and U PSDs after demodulation and leakage subtraction. The spurious signals at $2f = 4Hz$ are visibly excessive and cause $0.2Hz$ sidebands. Hence the low pass filter frequency is chosen to be $3.8Hz$.

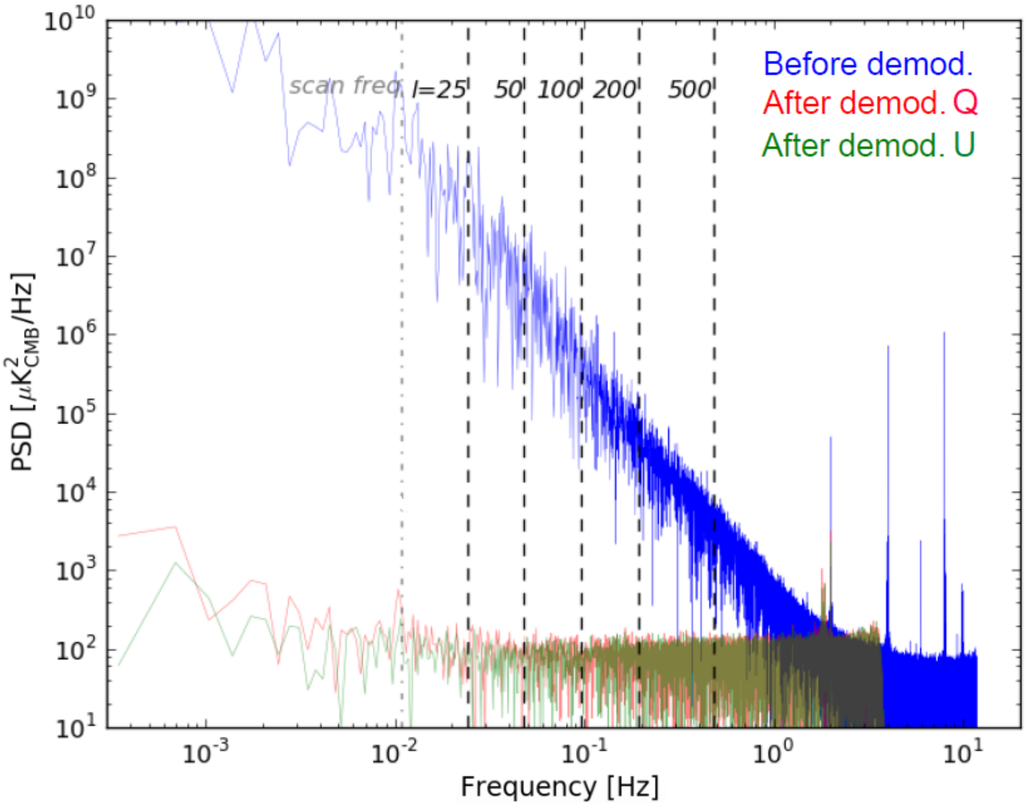

FIGURE 4.1: The PSD in frequency domain from 1 single CES. The vertical lines mark the scan frequency of $10mHz$ and the frequencies respective to shown ℓ multipoles. The blue PSD before demodulation consists of all components I, Q and U, the leakage to polarisation from the intensity component, and the HWPSS. The HWPSS spikes are visible at $1, 2, 3, 4, 5f$. The 'after demod.' Q and U PSDs are the results after demodulation and intensity leakage subtraction. Both the red Q and green U PSDs have spikes at around $2Hz$ which are relatively small compared to the HWPSS at the same frequency. The frequency range of Q and U PSDs goes up to only $3.8Hz$ due to the LPF. The U PSD is slightly more flattened at low frequencies because the leakage to U is smaller than to Q. Picture credit: Satoru Takakura.

After leakage subtraction, the U PSD is slightly more flattened at low frequencies because the intensity leakage to U is smaller than to Q due to the temperature-to-polarisation leakage being approximately out of phase with U [87]. An example of the difference between PSD of the demodulated Q and U timestreams prior to and after leakage subtraction can be found in Figure 5 in [76], where the leakage-subtracted PSDs are more flattened, which means an improvement in low frequency noise.

4.3 Pointing model

A key step in making maps is to determine where each detector is pointing on the sky as a function of time. The inputs to this are the telescope encoder readings of azimuth (AZ) and elevation (EL), as well as the thermometric measures of local conditions. The

TABLE 4.1: Parameters used for POLARBEAR pointing model

Parameters	Descriptions
ia	$AZ_{encoder}$ offset
ie	$EL_{encoder}$ offset and collimation error in elevation
ca	Collimation error in azimuth
an	Tilt of AZ axis from vertical in north direction
aw	Tilt of AZ axis from vertical in west direction
dt	Timing error in hour angle direction
sai	Differential solar heating flexure in elevation
sei	Differential solar heating flexure in azimuth

pointing model translates these inputs into Right Ascension and Declination (RA,DEC) on the sky as we opt for the equatorial coordinate system.

A key ingredient for the model is radio pointing observations that target bright extended and point-like millimeter sources chosen from known source catalogs [88, 89]. These sources have accurately known fixed sky addresses and cover a wide range of AZ,EL coordinates. Pointing observations are scheduled for at least once a day; each scan lasts between 10 to 15 minutes because sources drifts with time. Schedules also ensure that many locations across the CMB sky patch are observed.

The pointing model used for the maps in this work is an expanded version of the original 5-parameter model in [90], and includes 8 parameters as listed in Table 4.1. Five of these parameters capture the telescope structural misalignments, one stands for the timing error, and two represent flexure terms due to solar heating. One common pointing model is used to fit for all detectors. During the analysis, we tested reducing or adding more model parameters, but found these eight parameters were the minimal set to adequately recover sky positions. This work was done by Tucker Elleflot. The pointing of individual detectors is offset relative to the telescope boresight pointing. These detector offets are determined by raster scans across Jupiter. The offsets when combined with the boresight pointing yield the absolute pointing for each detector. Over all, we achieve an RMS error of less than $\sim 18''$ based on the bright radio sources.

4.4 Beam model

The beam model measures the impact on the signal received in detectors due to the limitation of the diffraction from the telescope optics. We represent the beam by a circular 2D Gaussian, with beam size defined by the effective Full Width Half Maximum (FHWM). Intuitively, there is signal suppression in all multipole scales, but higher multipoles undergo more suppression. This means the structures at high multipoles are washed out.

In addition to being used for the detector pointing model, observations of Jupiter are used to measure the beam maps. As a reminder, we use raster scans where we don't scan the entire planet for each bolometer at each observation. Instead, we track the planet, turning the telescope in large enough steps to allow all detectors in a row to see the planet. In actual analysis, we consider Jupiter as a point source with brightness temperature T_p because the angular diameter of the planet is small compared to the effective FWHM of $\sim 3.5'$ of each detector. We correct for the finite size R of Jupiter in the beam profile B_l in the final step with Bessel function $J_1(\ell R)$. For each detector, we make a beam map, m, that shows the spatial distribution of the beam-convolved planet. Calling the sky or planet signal S and B the effective beam of the instrument, we have the effect of the beam on an observed map m as:

$$m(\theta,\phi) = (S * B)(\theta,\phi) = \iint d\theta_1 d\phi_1 S(\theta-\theta_1,\phi-\phi_1)B(\theta_1,\phi_1), \tag{4.2}$$

where the $*$ sign means a convolution. Under the assumption that Jupiter is considered a point source, we can write the beam profile as:

$$B(\theta,\phi) = \frac{m(\theta,\phi)}{T_P \Omega_P} \tag{4.3}$$

where Ω_P denotes the solid angle subtended by Jupiter, and the brightness temperature of Jupiter T_P is used in place of the signal S. Jupiter's temperature is a fixed value taken from millimeter-wave measurements of [91]. Timestream of each bolometer is filtered to minimise the effect of atmospheric fluctuations by a masked first-order polynomial. We mask $50'$ around Jupiter for the polynomial fit. The filtered timestream is then coadded to detector maps, centered on Jupiter. Individual detector maps are weighted by the noise outside the mask radius to combine into one single scan map. This is necessary to have enough coverage and adequate signal to noise ratio to get beam profile from each observation. Figure 4.2 shows the full season map coadded from 215 observations, and 1 example map for 1 single wafer of detectors.

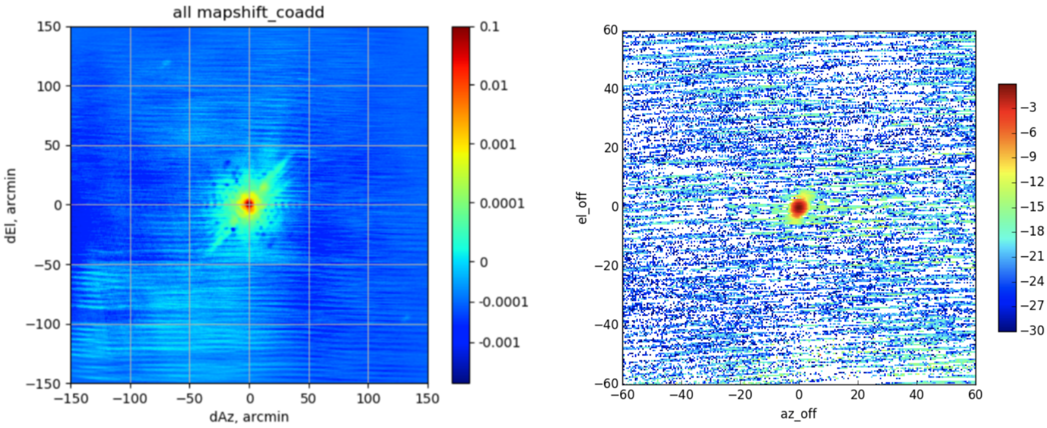

Figure 4.2: Left: Map of Jupiter coadded from all observations in all seasons in K_{RJ} and plotted between $azimuth = -150', 150'$ and $elevation = -150', 150'$ the map center is offset at the planet center. Picture credit: Neil Goeckner-Wald. Right: Map of Jupiter coadded from maps of all detectors in one wafer, which consists of around 200 working bolometers on average. The unit is ADC counts. This map is plotted between $azimuth = -60', 60'$ and $elevation = -60', 60'$ the map center is offset at the planet center. The white areas are missing pixels.

Convolution is done by multiplication in the frequency domain.We approximate each observation profile as the azimuthally averaged Fourier components converted to the multipole components:

$$B_l = \frac{M_l}{T_l W_l} \tag{4.4}$$

Here M_l is the temperature-calibrated map $m(\theta, \phi)$ Fourier transformed in 2 dimensions into $M(l, \phi_l)$ then averaged over ϕ_l. T_l is the response function for a finite planetary disk converted to Fourier space. The pixel window function W_l is to account for the effect of the pixelisation of the map. The final B_l is derived from profiles of all observations weighted by the noise estimated from noise when fitting all detectors to the planet template. The resulted degree of ellipticity of POLARBEAR beam is much less than 5%. Figure 4.3 shows the B_l profile from a number of observations with reasonable shapes and the combined final B_l. Note that the beam profiles calculated immediately from 4.3 are not normalised as those shown in Figure 4.3. Beam model analysis was done early on by David Leon, then by Neil Goeckner-Wald. We opt for Neil Goeckner-Wald's work for the final model. My own processing of Jupiter observations was used for first iterations of gain calibration, then as a crosscheck for Neil Goeckner-Wald's work and finally for the beam covariance construction.

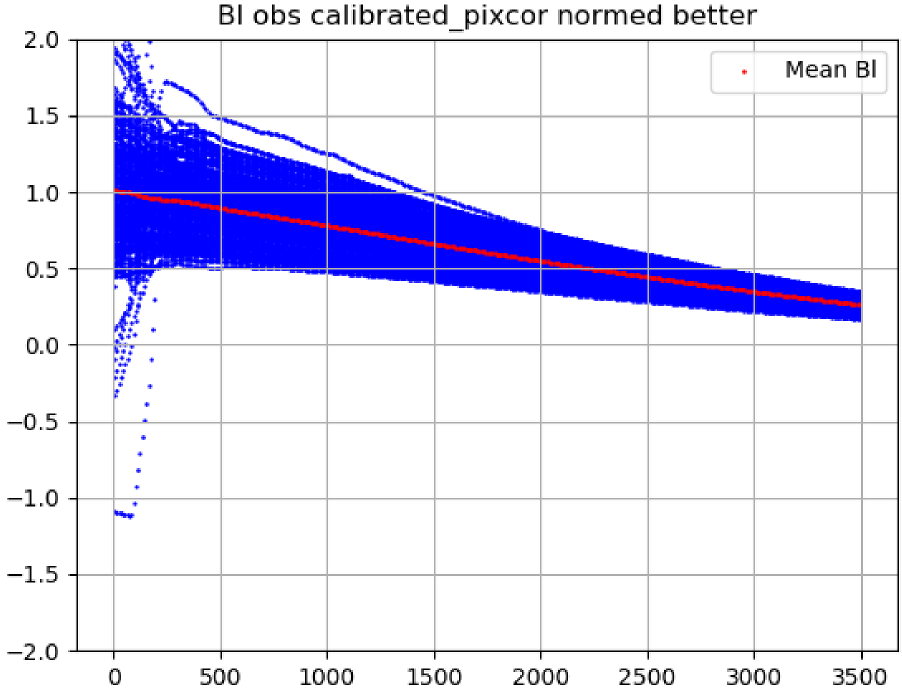

FIGURE 4.3: The normalised B_l from individual observations that are taken in to final B_l. The vertical axis is the amplitude with no unit. The horizontal axis is the multiple ℓ. While there are over 200 Jupiter measurements, only 183 are included for the final combination because beam profiles from excluded measurements are pathologically noisy.

4.5 Gain calibration

We also need to know the conversion from the recorded ADC units of time-ordered data to K_{CMB} on the sky, also known as the gain calibration. This is done in 3 main steps: 1,) getting detector responses in physical temperature with planet measurements, 2,) getting detector responses in ADC units from stimulator scans, 3,) matching these 2 types of responses to convert detector response originally in digital count unit to temperature unit. This section will first describe the further use of the planet measurements with Jupiter, then the stimulator scans and the calculation of the gain model. The elevation-nod scans will also be described because they are used as a crosscheck before the gain model is finalised. The analysis from the stimulator measurements onward in this section is my work.

4.5.1 Calibration with planet

Observations of Jupiter in 4.4 are used for gain calibration because the planet temperature T_P is a well-measured quantity across many experiments. We have around 70 Jupiter observations per season of observation.

Because what we get from stimulator scans are detector response in detector unit, it means we need to derive conversion factors from detector units to physical units using planet scans. We call the conversion factors the planet gain factor G. Note that as in section 4.4, signals received by detectors are partially suppressed due to the limitation of the telescope optics and presented by convolution of the input signal with the beam of the instrument. So the planet gain factor can be given as

$$G = \iint d\theta d\phi B(\theta, \phi) \tag{4.5}$$

Using the definition of a single Jupiter beam map shown by Equation 4.3 and noting the relation 4.5, we can express planet gain factor as:

$$G \approx \iint d\theta d\phi \frac{m(\theta, \phi)}{T_P \Omega_P} \tag{4.6}$$

From 4.6, the unit of G is ADC/K_{RJ} if m is an uncalibrated map in ADC. Due to the nature of employed raster scans where individual detectors do not see the entire Jupiter in each scan and elevation steps are too widely separated (2 arcminutes), the map term in the above equation is inefficient i.e. containing not enough information. Hence, in real analysis, we fit an elliptical Gaussian model to planet map centers then account for near-sidelobes by an integral of the map residuals from fitting. The expression for this model for a detector channel in an observation is:

$$G_{ch,obs} = \alpha(obs) \frac{I_1(ch, obs) + I_2(ch, obs)}{T_P \pi r_P^2(obs)} \tag{4.7}$$

Here, α denotes the correction for atmosphere transmission, T_P is the brightness temperature of Jupiter in microwave band, r_P is the average angular radius of Jupiter. I_1 and I_2 are the integrated intensity (in ADC.steradian) contributed by main lobe and side lobe respectively. Note that α,the inverse of the atmospheric transparency, is mainly used from APEX[1] but can also be estimated with elnod scans where Polarbear measure of sky brightness at different elevations. The angular radius of Jupiter for each observation is computed using ephemeris.

[1]http://www.apex-telescope.org/

To determine the intensity of Jupiter as seen by the detector main lobe, filtered timestream of a channel $d_{ch,obs}$ is first fitted with a 2D Gaussian template $P(A, \sigma_x, \sigma_y, x_c, y_c)$:

$$P(A, \sigma_x, \sigma_y, x_c, y_c) = Aexp(-\frac{1}{2}v^T C^{-1} v) \tag{4.8}$$

with $v = (x - x_c, y - yc)$ and $C = Diag(\sigma_x^2, \sigma_y^2)$. The intensity term from main lobe is then estimated by:

$$I_1 = \iint dxdyP(A, \sigma_x, \sigma_y, x_c, y_c) = 2\pi A\sigma_x\sigma_y \tag{4.9}$$

where σ_x and σ_y are the beams widths in 2 orthogonal directions. The 2D gaussian model has a corresponding simulated timestream. We thus subtract this simulated term from the original filtered timestream then calculate the side lobe intensity by integrating the intensity between 2 radii r_{in} and r_{out}:

$$I_2 = \iint_{r_{in}}^{r_{out}} dxdy(d_{ch,obs} - d_{ch,obs}^{sim}) \tag{4.10}$$

Typically, we use $r_{in} = 4'$ and $r_{out} = 15'$, and near-sidelobes intensity accounts for 10% of the total.

4.5.2 Stimulator response

Relative gain calibration for detectors is not complete without the measurements of detector responses in digital units using the stimulator. POLARBEAR stimulator consists of thermal source with known temperature of around $700°C$ placed behind the secondary mirror. This thermal source can transmit signals to bolometers through a $6.35mm$ light pipe connecting with a small gap in the secondary mirror. Note that large patch observation data have been divided into 3 seasons 3, 4, and 5 with respect to 3 times of stimulator source replacement. The stimulator also contains the chopper which is a two blade fan driven by a miniature stepper motor and having spinning frequency between 2 and 24 Hz. The stimulator chopped signal is thus modulated at 4-48 Hz. The temperatures of the source and the ambience of the chopper are measured with thermocouples and kept stable across long time scales.

Besides the stimulator thermal signal, the chopper also interrupts the photosensored synchronous demodulation of the detector timestreams. The photosensor data are sampled at 40 kHz by a computer data acquisition card, from which edges are detected. The arrival time of the edges in 40 kHz clock cycle counts are archived along with bolometer data. The storage of edge arrival times serves as a check on the frequency and stability of the chopper. In brief, the speed of the chopper(which is assumed to be constant) is fit to the registered chopper edge arrival times. RMS residuals of the timing error can signify stimulator failure if much different from the typical value of $30\mu s$.

As mentioned in Chapter 2, the stimulator measurement is the opening and also the end observation of each hour-long CMB scan block so as to calibrate the response of detectors during the entire block. Total observation time is 2.5 minutes, where the source is observed at a range of frequencies of 4- 44 Hz for 30 seconds each. This change of frequencies is designed to measure the bolometer time constant. At each observing frequency, the temperature observed by each bolometer is measured by fitting the following model to the frequency f and phase ϕ of the chopper:

$$M = Acos(2t\pi * f + \phi) \tag{4.11}$$

where A denotes the amplitude whose root mean squared is used as the effective stimulator temperature. Figure 4.4 shows the fitting of an example bolometer response by the stimulator chopper.

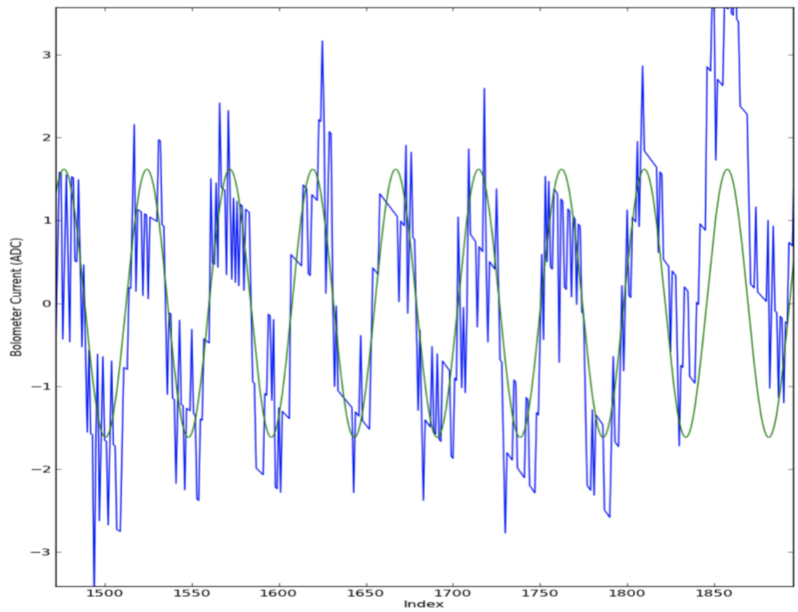

FIGURE 4.4: Bolometer response with respect to time. The real response of a bolometer by the chopper is in blue, and the fitted response is in green. X axis shows time index, and Y axis show the values of bolometer response in ADC count unit. For convenience, this picture is borrowed from [10]

The response of bolometers is best fitted to an one-pole constant model:

$$m(f) = \frac{g}{\sqrt{1 + (\frac{f}{f_{3dB}})^2}} + n(f) \tag{4.12}$$

Here, $m(f)$ is the magnitude of the response at frequency f, g is the detector gain, and bolometer time constant f_{3dB} is represented as $3dB$ roll off frequency. $n(f)$ is added as the error on the measurement of the magnitude. Note that, before all fittings, the detector timestreams is demodulated due to HWP rotation then high pass filtered. The first 30 second stimulator stare at one chopping frequency is used for an additional 10th order polynomial subtraction. The mean value of the time constant is 0.0025. A typical time constant fit is shown in Figure 4.5.

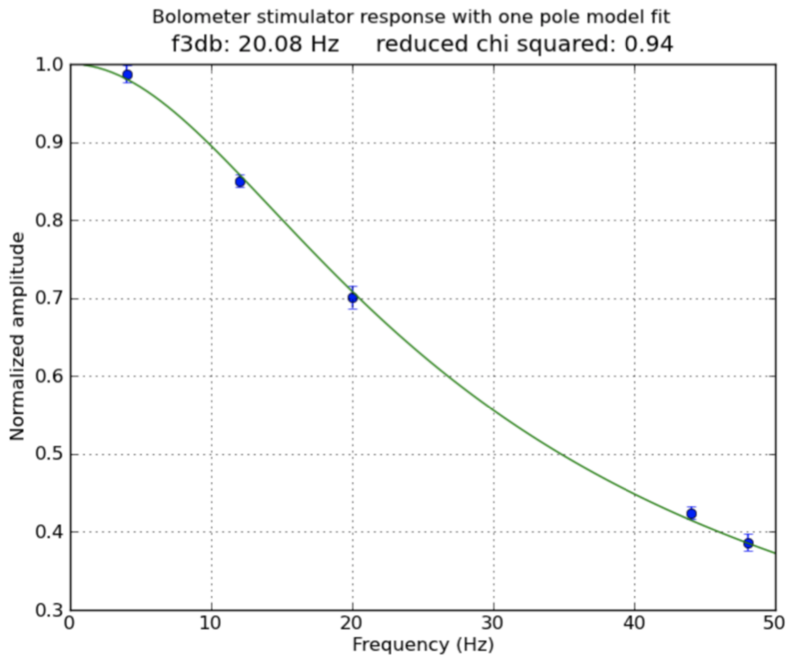

FIGURE 4.5: Example fitting of the magnitude of the response of a bolometer to the one-pole model with stimulator chopping at five frequencies. Blue denotes the magnitude response at the 5 frequencies and corresponding errors. Green shows the fit to one-pole model. Picture is borrowed from [11]

Having both the planet gain factors and the relative gains, we are now ready to make the intensity template for the detectors.

4.5.3 Intensity template and Effective temperature

Since planet observations are bootstrapped with stimulator scans, we match the mean of relative gain amplitudes of stimulator measurements done before and after the planet scan with planet gain factors. For each detector *ch* and each planet observation *obs*, we have:

$$A_{ch,obs} = \frac{A^{pre}_{ch,obs} + A^{post}_{ch,obs}}{2} \tag{4.13}$$

where *pre−* and *post−* mean before and after planet scan respectively. The effective temperature of each channel in each scan block is then determined by combining the mean relative scan amplitude and the planet gain G:

$$T^{eff}_{ch,ob} = \frac{A_{ch,obs}}{G_{ch,obs}} \tag{4.14}$$

The errors for the 2 above quantities are calculated by:

$$\Delta A_{ch,obs} = \left|\frac{(A^{pre}_{ch,obs} + \Delta A^{pre}_{ch,obs}) - (A^{post}_{ch,obs} - \Delta A^{post}_{ch,obs})}{2}\right| \tag{4.15}$$

$$\frac{\Delta T^{eff}_{ch,ob}}{T^{eff}_{ch,ob}} = \sqrt{(\frac{\Delta A_{ch,obs}}{A_{ch,obs}})^2 + (\frac{\Delta A}{A})^2 + (\frac{\Delta\sigma_x}{\sigma_x})^2 + (\frac{\Delta\sigma_y}{\sigma_y})^2} \tag{4.16}$$

Here, A, σ_s and σ_y are beam parameters determined for the planet gain as in section 4.5.1. These errors are calculated to use as weighting factors for each observation as well as to estimate the overall error caused by gain calibration. The intensity template of one whole season of observation is the weighted average of intensities of all scan blocks:

$$I^{eff}_{ch} = \frac{\sum_{obs} T^{eff}_{ch,obs} w_{ch,obs}}{\sum_{obs} w_{ch,obs}} \tag{4.17}$$

$$\Delta I^{eff}_{ch} = \sqrt{\frac{\sum_{obs}(T^{eff}_{ch} - T^{eff}_{ch,obs})^2 w_{ch,obs}}{\sum_{obs} w_{ch,obs}}} \tag{4.18}$$

where $w_{ch,obs} = 1/(\Delta T^{eff}_{ch,obs})^2$ is the inverse variance for each observation of a detector.

Since the temperature of the stimulator source is maintained stable for each season and the effective temperature of Jupiter is regarded constant after distance correction, we assume the intensity template is representative of the effective temperature of each bolometer for 1 whole season. We then have the relative gain conversion for 1 detector for a given stimulator observation to be:

$$g_{ch,obs} = \frac{I^{eff}_{ch}}{A_{ch,ob}} \tag{4.19}$$

We need to iterate on creating the intensity templates because this template affects our data selection and can also be used to check the impacts of the atmosphere on the detectors through the precipitated water vapor (PWV) measured with elevation-nod scans.

4.5.4 PWV measurements

In every constant elevation scan block, we also perform an elevation-nod (elnod) scan where the telescope nods up and down slowly between 2 elevations. Different elevations mean different atmospheric depths, which leads to variation in the input load temperature by $(\sin el)^{-1}$. The sky temperature at zenith observed by the receivers the atmospheric transparency τ following:

$$T_z = T_z^0(1 - e^{-\frac{\tau}{\sin el}}) \tag{4.20}$$

where T_z^0 is the true sky emission temperature. The dependence of the transmission τ on PWV at each frequency ν follows [92]:

$$\tau(\nu, PWV) = \tau_w(\nu) \times PWV + \tau_d(\nu) \tag{4.21}$$

where τ_d is an unvarying transparency term in dry condition, τ_w is the opacity term in wet condition and depends on the PWV of the atmosphere which varies with the time of observation. Given the elevation determined with telescope pointing data, the bolometer response with respect to time t is modeled as:

$$R = G(\frac{T_z}{\sin el} + N) + \gamma t \tag{4.22}$$

Here, gain factor G is determined from stimulator and planet measurements. Note that G is interpolated for every sample in the elnod TOD (or any CES TOD) and has the unit of ADC/K_{RJ}, N is an offset noise term, and γ denotes the slope in the bolometer response drift, which originates from offset drifts observably due to changing elevations while facing large 1/f noise.

In practice, the transmission templates are first prepared with the ATM software [12] for a wide range of PWV. These templates are similar to Figure 4.6 created with ALMA[2]. With this transmission template, we built a set of observed sky temperature $T_z^{template}$ with respect to the PWV and the zenith angle which relates to the elevation via $z = \pi/2 - el$. The actual bolometer TOD is fitted to the model of 4.22 for T_z, from which we can obtain the PWV values using $T_z^{template}$ and el from the scan data. Figure 4.7 shows an example of this fitting. With the derived PWVs, the correction α from Equation 4.7 for an observation having PWV available in close time is calculated via 4.21 and:

$$\alpha(obs) = \frac{1}{e^{-\tau(PWV)\sec(z)}} \tag{4.23}$$

[2]https://almascience.eso.org/about-alma/weather/atmosphere-model

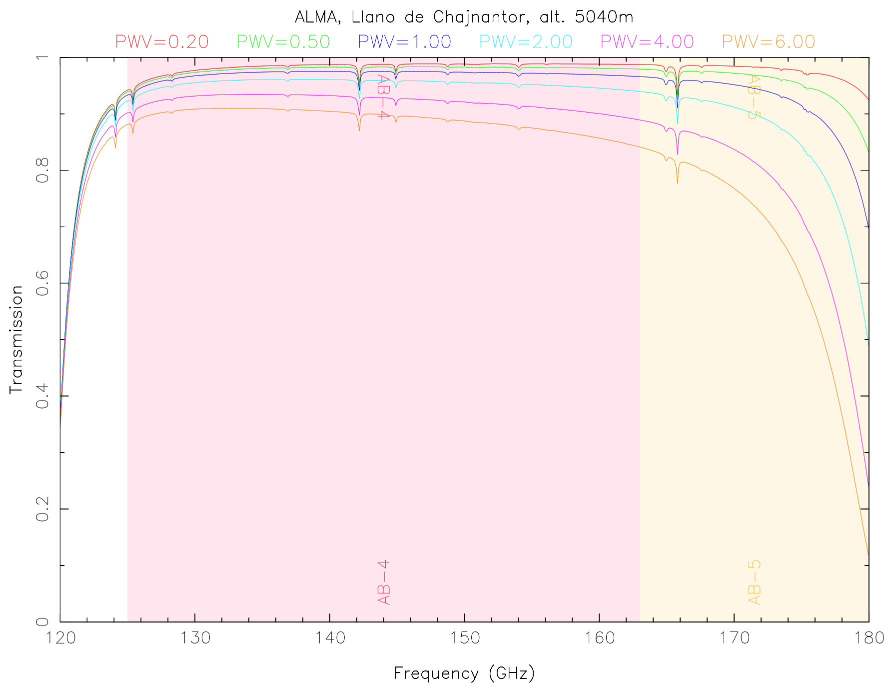

FIGURE 4.6: Atmospheric transmission between 120 and 180 GHz, POLARBEAR's frequency range of interest, for a set of PWV values is based on ATM software [12]. The PWV affects the correction of the data more severely as it increases.

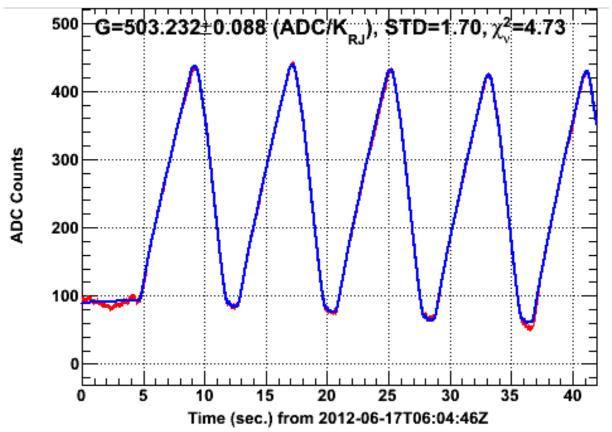

FIGURE 4.7: An example of fitting real TOD (in red) to a model of bolometer response (in blue) dependent on the elevations and PWV. The noted gain value G is calculated from stimulator measurements and planet measurement that happened in the same scan block. There is an overall observable slope in the TOD. Picture credit: Yuji Chinoney.

PWV values are used to select quality observations and to double check the gain factors. The last stage is to generate the effective relative gain in ADC/K_{RJ} for each channel for all science observation following Section 4.5.3. The whole pipeline is summarised by Figure 4.8.

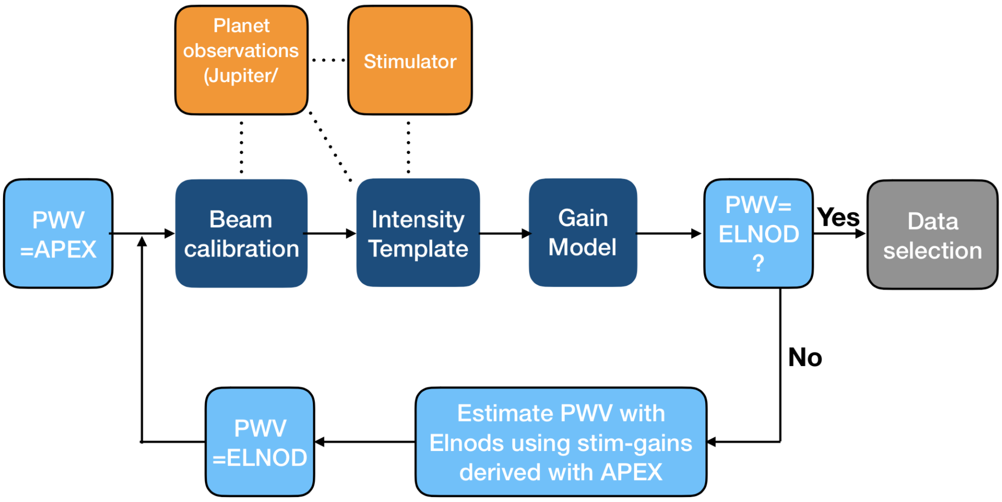

FIGURE 4.8: Relations of the components to get the final relative gain calibration. We first use PWV taken from APEX data as a multiplicative corrector for our observations of Jupiter. After getting the gain conversion factor following section 4.5.3, we re-estimate the PWV using POLARBEAR elnod scans. We then compare the distribution of the PWVs estimated in 2 sources and re-derive the gain templates for comparison. PWVs from APEX are used for the final gain model however.

4.5.5 Result for large patch data

Gain models have been finalised for all seasons of observations. While there were a number of scans of Saturn in the third seasons, I only use Jupiter for relative gain calibration to avoid unknown sources that can cause the difference between the intensity templates of each season. A series of tasks were done to validate the generated gain template: check of stimulator template as a relation with distance of Jupiter to the Earth, comparison of PWVs measured by POLARBEAR elnod scans and by APEX, check gain model i.e gain conversion files by using this model to calculate the flux of a known source i.e Tau A.

First, double-checking was done to see the effects of the distance of Jupiter from Earth on the templates. Jupiter's distance from the Earth varies between $\sim$ 650 million Kms and $\sim$ 950 milllion Kms. Thus, I divide the calibration measurements of each season into 2 halves with Jupiter's distance to Earth less than or more than 800 million Kms then create 2 respective intensity templates for comparison. Figure 4.9 shows an example of the templates for 2 halves of the third season. Two later seasons have similar results and are thus not shown.

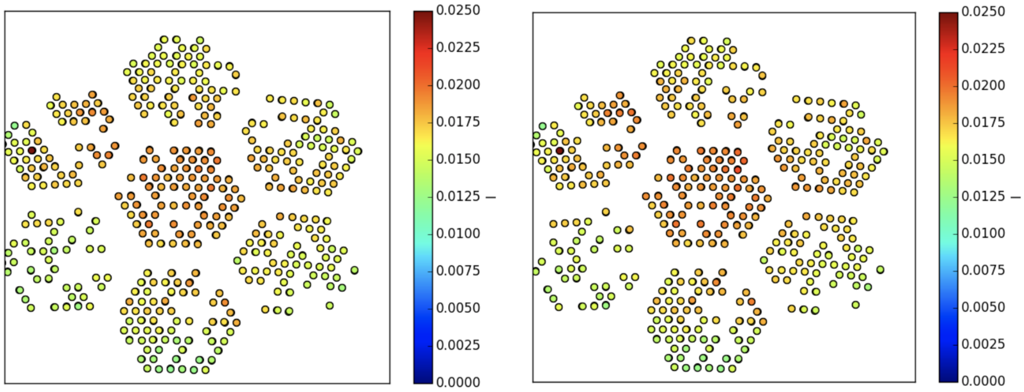

FIGURE 4.9: The intensity templates for 2 halves of calibration data in the third season are approximately identical. The template on the left has 38 Jupiter measurements while the one on the right has 36 measurements.

Second, comparison between PWV estimated from POLARBEAR elnod scans and PWVs from APEX data is also earlier mentioned in the pipeline iteration chart 4.8. Figure 4.10 shows the ratios between these 2 sets of PWV values. Stimulator scans and planet scans that the return PWV values that are more than 1.3 times different from APEX PWVs are discarded. In CES data selection in 5.2, we actually perform a cut discarding observations with $PWV = 4$. This cut however does not remove more than 5% of CES data because it is largely degenerate with the detector cut basing on observations that have very few channels alive. This detector cut is dependent on calibration cut and noise criteria and thus overlaps with the cut due to mismatching PWVs between APEX and POLARBEAR. Besides imposing the thresholds on the PWV values, which are used to correct observed planet intensity, the criteria to select data for intensity templates are based on the stimulator amplitudes and the planet gain factors. Detectors and observations that have stimulator amplitudes or planet gains outside of 2 sigmas of the mean value for all detectors in 1 single wafer are discarded. This is done to remove outliers in the stimulator intensity templates that obviously deviate far from the mean value of around 0.018 K_{RJ} as shown in Figure 4.11

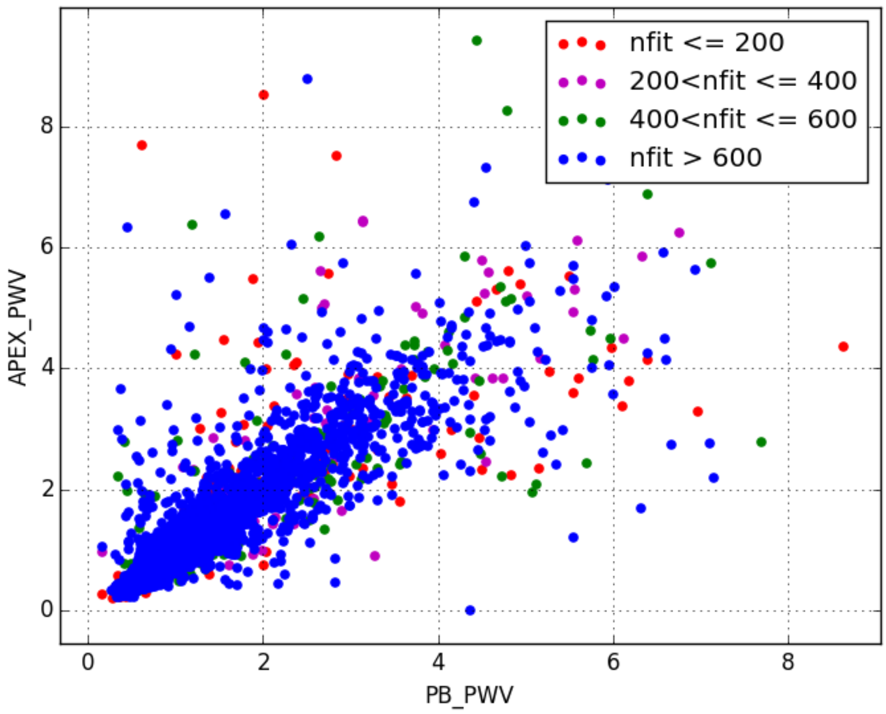

FIGURE 4.10: The PWVs measured by POLARBEAR elnod scans in comparison with PWVs from APEX. The unit for both axes is *mm*. The majority of PWVs from POLARBEAR analysis and from APEX have the 1:1 ratio. Selection of stimulator scans and planet scans also ensures that the relevant PWV ratios are not more than 1.3. The colors specify the number of channels "nfit" that yield fitting results for a single observation. Each observation is presented by color dot.

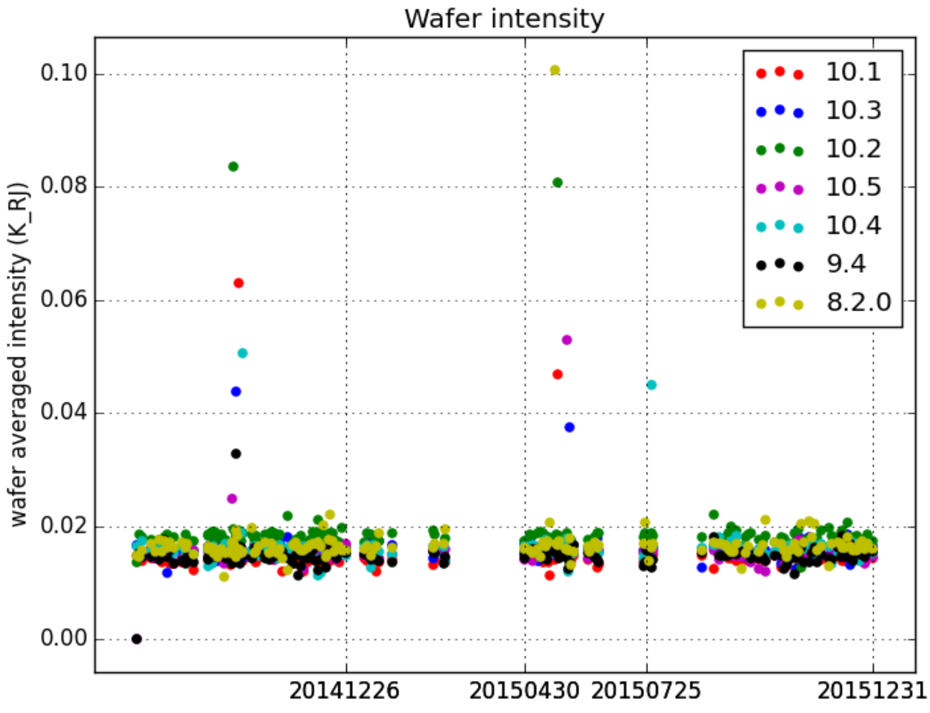

FIGURE 4.11: The intensity by each day averaged for all detectors belonging to the same wafer on the focal plane. The names and colors of the wafers are shown in the legend. All outliers are cut after imposing criteria on the stimulator amplitudes and planet gains, and reiterating of the pipeline to get a new intensity template.

Bolometers that don't appear in the intensity template are by default excluded from the rest of the analysis. Thus, each season has around 700 bolometers that remain in the template over 1512 ones.

The third check is done by creating maps of TauA then fitting a 2D Gaussian template to each map and calculate the flux by:

$$Flux = Amplitude \cdot \sigma_x \cdot \sigma_y \tag{4.24}$$

where σ_x and σ_y are the width in horizontal and vertical axes of intensity distribution on each TauA map. The values are then used to see the mean flux and deviation for each season. Result is show in Figure 4.12 for 3 seasons.

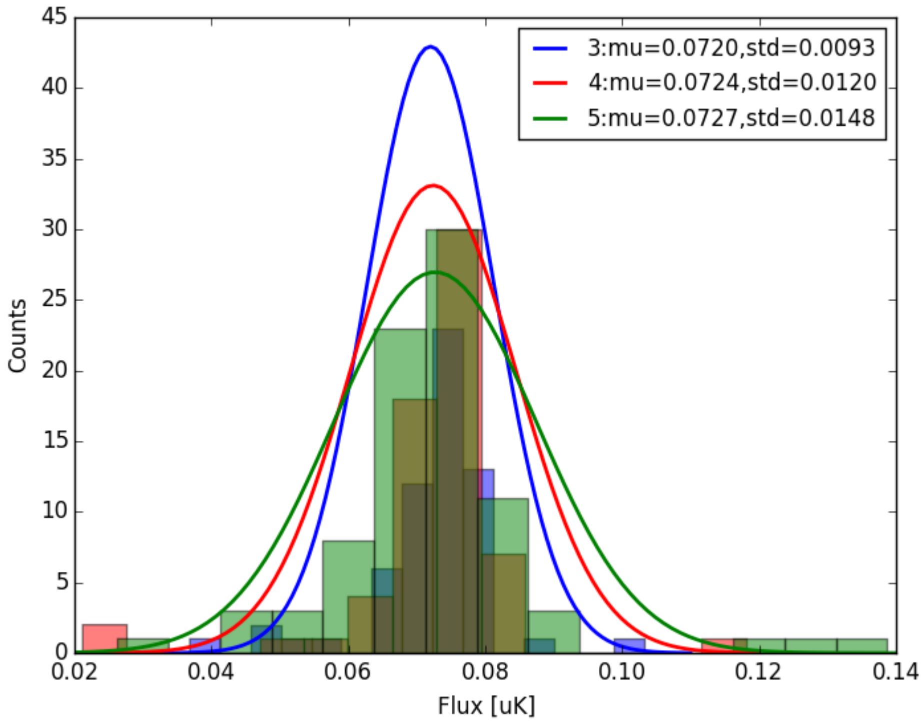

FIGURE 4.12: Histogram of the flux values for separate seasons 3,4, and 5. Mean values "mu" and standard deviation "std" are also noted. This is created before the final gain model is generated but shows good consistency between 3 seasons prior to removing outliers and also using the optimal polarisation angle calibration.

Finally, figure 4.13 shows the intensity templates for 3 seasons of large patch observations. The difference between each 2 seasons is due to the replacement of the stimulator source which corresponds to changes in amplitudes of the stimulator gains. This however does not affect the relative gain factors derived with Equation 4.19.

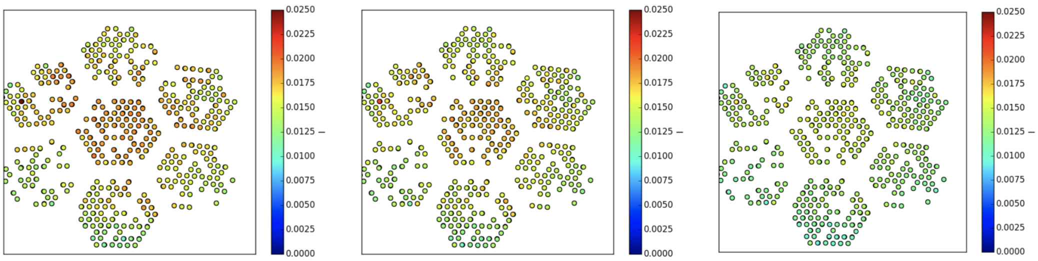

FIGURE 4.13: The intensity templates for 3 seasons of large patch observations of POLARBEAR, showing minor fractional difference between 3 seasons. The unit of the colorbar is K_{RJ}.

Having the relative gain factors for both pre- and post-stimulator measurements of each scan block, I generate gain conversion files by doing linear interpolation for all the scans in between over 2 ending values to account for possible drifts in the gains. The gain drift can be caused by the atmospheric loading changes. With interpolated gain factor $g_{ch,pbs}$, we have calibrated timestreams for every observation to be:

$$d^{cal}_{ch,obs} = \frac{I^{eff}_{ch}}{A_{ch,ob}} d_{ch,obs} \tag{4.25}$$

If an observation does not have a pre- or post- stimulator measurement passing the selection based on the stimulator amplitudes, that observation will be excluded from the final data product. As a result, each CMB observation has around 400 alive channels on average. The mean drift between any 2 consecutive observations is found to be 0.9%. The average total error from gain calibration is a quadratics combined from error of the effective temperature and stimulated gain amplitudes in Equation 4.7 and is found to be 4.7% for each detector. We will now look at the last component of data pre-processing, polarisation angle calibration.

4.6 Polarisation angle calibration

Polarisation angle calibration refers to determining the global instrument polarisation angle, individual detector polarisation angle and individual detector polarisation fraction(or polarisation efficiency) for the instrument. The global instrument polarisation angle means the absolute orientation of POLARBEAR polarisation with the sky polarisation. The detector polarisation angle calibration, also known as the relative polarisation angle calibration, means calibrating the orientation of the detector polarisation axis with respect to the sky coordinate system. Detector polarisation angle calibration for POLARBEAR observations in seasons 3-5 has been done by Greg Jaehnig and detailed in [93] and is summarised as followed.

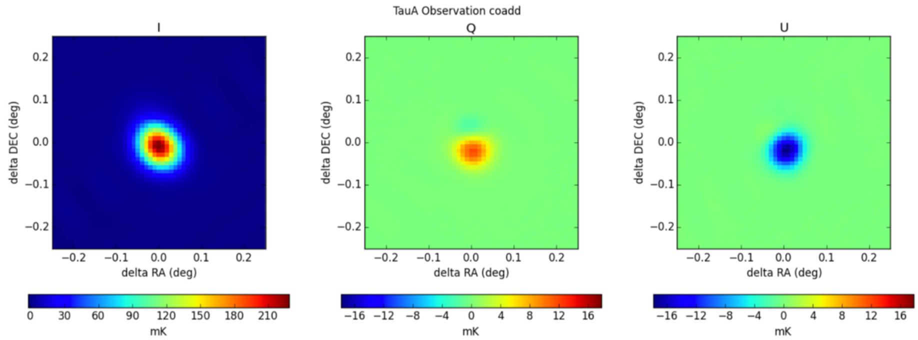

FIGURE 4.14: TauA measured in Stokes components I, Q, and U after coadding observation data from 3 seasons of observation. These maps shows good agreement with Tau A map by IRAM [13], implying stability of the detector polarisation angles across the seasons. The unit is mK_{RJ}. Picture is Greg Jaehnig's courtesy.

We use Tau A, the Crab Nebula or M1, as the source for polarisation calibration. Tau A consists of a rapidly rotating neutron star core wrapped by supernova remnant [94, 95]. It is a well-suited calibrator due to being the strongest source of synchrotron radiation in our galaxy [96] and being well studied in multiple frequency ranges. Description of the total flux of Tau A by frequencies are noted in [96]. Tau A polarisation angle measurement at 150 GHz can be found in [97]. Despite its decrease in intensity of 0.22 per year due to the remnant expansion [98], Tau A is expected to have the polarisation fraction and angle unchanged with respect to frequency because the synchrotron radiation is produced by the same magnetic fields. Both WMAP and Planck observed Tau A [98, 99], having results consistent with a polarisation fraction $7.00 \pm 0.22\%$. Precise measurements of Tau A polarised flux have been done by The Institut de Radioastronomie Millimétrique (IRAM) 30m telescope 89 GHz [13] and can be used to calibrate other instruments' observations of Tau A.

POLARBEAR observes Tau A with raster scans when not scanning the CMB patch. The elevation range to observe Tau A is between $38 - 32^\circ$ to substantially avoid detector performance degradation from the atmospheric loading with lower elevation and to prioritise CMB observations that have higher elevations. While Tau A has many characteristics [100], POLARBEAR should smooth out features of Tau A due to $3.5'$ beam FWHM as compared to Tau A's angular size of $7' \times 5'$, which simplifies the calibration.

Calibration analysis can be done using both maps and TOD. In the first way, maps of Tau A in Q and U are made processing the TOD through the mapmaking pipeline described in Chapter 5. Figure 4.14 shows TauA in I, Q, and U after coadding all observation together. Note that in this process, the time constant derived in section 4.5 is deconvolved from the TOD to correct the phase lags between the detector TOD and the reconstructed HWP angles since the phase lags can add up to the polarisation angle errors. From the produced map, Tau A angle is calculated by summing pixels i within $10\prime$ radius,

$$\alpha = \frac{1}{2} arctan2(\sum_{i}^{r_i<10\prime} U_i, \sum_{i}^{r_i<10\prime} Q_i) \tag{4.26}$$

where $arctan2$ means the $arctan$ of the angle formed by 2 axes (U, Q), similar to the definition in [97]. In the second way, TOD is simulated by scanning IRAM's I,Q, and U maps of Tau A with POLARBEAR's configuration for pointing, beam, and scan pattern. This can negate possible systematics that can vary between Tau A maps produced in the first way. The simulated TOD is then compared to a model that typically contains I,Q and U as in Chapter 3, but modified as:

$$d = g((I + x_i) + \rho(Qcos(2\Theta) + Usin(2\Theta))) \tag{4.27}$$

Here, g is the relative gain between POLARBEAR and IRAM. The polarisation efficiency ρ is a constant if without systematic effects. The angle Θ is modeled as :

$$\Theta = \theta_{pa} + 2\theta_{CRHWP} + 2\theta_{CHWP} + \pi/2 - \theta_{det} \tag{4.28}$$

where θ_{pa} is the parallactic angle of the source. Due to the sky rotation, the angle θ_{pa} is time-dependent, decreasing clock-wise from North on the celestial sphere following the convention of the International Astronomical Union. θ_{CRHWP} is the encoded rotating HWP angle, θ_{CRHWP} is the angle of the original cold HWP (CHWP) placed inside the cryogenic receiver in the instrument frame, and θ_{det} denotes the detector angle. We fit this TOD model to the simulated TOD for the unknowns g, ρ, θ_{CRHWP}, and θ_{det}. In the final result, the mean Tau A angle is found to be 150.°61 with standard deviation of 0.°31, which is in good agreement with [13]. CRHWP encoder position as well as the CHWP position are found to be stable across the seasons. The polarisation efficiency of POLARBEAR is varied across detectors in the focal plance and not perfect due to the mirror conditions, the intervention of CRHWP and cold HWP, and time constant. The angles between detectors in a pair of a pixel is consistent with 90°.

Note that the cold HWP was stationary across 3 seasons, and it impacts the TOD in 2 ways. First, the cold HWP rotates the overall polarisation angle of the detectors on the focal plane by some amount according to its position. Second, it reduces the polarisation efficiency by some percent which factors into the absolute EE gain calibration. The absolute EE gain calibration, done in 6.4 and 7.1, is found to be degenerate with absolute polarisation angle calibration corresponding to the correction needed for the effect due to global instrumental polarisation angle. The global instrumental polarisation angle causes the leakage of E to B and can be found and corrected for by fitting $C_l^{EB} = 0$

following [101]. Estimation of systematic errors due to global instrumental polarisation angle and detector polarisation angle is done in 6.4.

Chapter 5

Data analysis

5.1 Overview of the analysis pipeline

The main analysis involves using real data from POLARBEAR's science scans of the large patch of sky to create an estimate of the CMB anisotropies. This analysis employs a 3-stage pipeline. The first stage is data selection, which flags and removes anomalous data that can pass on as bias in the maps of the mapmaking stage. The second stage is map making from selected data. This stage aims to produce optimal anomaly-free maps by handling noise characteristics and non-idealities of the data with filtering and weighting options of TOD. The processed TOD is projected into flat maps of the sky. The corresponding third stage uses a flat sky approximation on the flat maps to produce pseudo spectra whose biases generated due to mapmaking are subsequently corrected with a combination of linear operations to yield a final estimate of the true CMB power spectrum. The pipeline used to compute the anisotropies in the high multipole range $\ell = 500 - 3000$ in this thesis is largely overlapping with the pipeline for the low multipole range $\ell < 500$ described in [102]. The 3 stages will be summarised here, and any differences will be noted. Overall, I am involved in creating the apodisation mask module and band power covariance in 5.6 and improving the modules for pseudo power spectrum, filter transfer function, and debiasing in 5.5.

5.2 Data selection

The data selection stage for high-ℓ includes 3 rounds of operations to remove possible problematic features in the TOD and to define noise characteristics: 1) glitch cut, 2) detector noise cut, 3) map domain noise cut. For the low multipole range, there is a common mode time domain noise cut before the map domain variance cut. In all rounds, we examine the detector subscans, which are defined as turns of telescope going left or right, and discard all data with the telescope's accelerating during turnarounds due to TOD spikes that are synchronous with such acute movements of the telescope. The data selection pipeline and the mapmaking pipeline share several TOD filtering and patching options, and outputs from noise characterisation in the data selection are employed in the mapmaking operation.

The first round, glitch cut, searches for and removes glitches in 2 main steps. The first step aims for fast glitches in individual detector full sample rate data. The high frequency sharp features in TOD are spotted and removed using a convolving high-pass kernel which also nulls out the HWP synchronous signal appearing at multiples of the HWP rotating frequency. Subscans where ratios of the maximum deviation to the standard deviation in the convolved TOD exceed 10 times are discarded. This leaves gaps in the TOD, which are then filled with HWP synchronous structure then demodulated following Section 4.2. At this point, the TOD consists of an intensity component and polarisation components and are passed onto additional high pass kernels. Subscans are again subjected to removal if having their maximum deviation 10 times larger than standard deviation. The second step aims for common mode low frequency glitches which are shown to originate from cloud polarisation in the upper atmosphere in [82]. Principle component analysis is done on the focal plane to remove detectors with insignificant atmospheric common mode in intensity timestreams. The TOD consisting of $Q + iU$ are processed in instrument frame and coadded to produce a full focal plane common mode signal. This signal is decomposed into minimum and maximum variance eigenmodes. Subscans are cut if having the ratio of the standard deviations of maximum to minimum modes larger than ten.

The second round is performed on demodulated timestreams of individual detectors to derive noise properties and remove detectors basing on noise statistics. Demodulation for CMB data is described in 4.2. Like for low multipole range $\ell < 500$, we now use a firs-order subscan polynomial filter on each demodulated TOD. The TOD then undergo subtraction of ground-fixed signals and temperature-to-polarisation leakage. The first subtraction is done by removing the template resulting from binning TOD in azimuth. The second is done by a PCA technique similarly in [76]. Note that these subtractions are also performed in the mapmaking stage in 5.3. Earlier flagged turnarounds and glitch-cut subscans are patched with white noise matching local RMS. The TOD now are considered "cleaned" and used to take the power spectral densities (PSD), each of which is then fit to a model composed of white noise and a $1/f^2$ low frequency noise term. The power law stays fixed at 2 for all detector PSDs because because letting it run freely does not improve resolving of the spectral shape of the low frequency component. Detectors are discarded if fitting is poor or results in pathologically high white noise floors, high 1/f noise. The fit quality is determined by the most extreme and average χ^2 of the real PSD to the noise model in the frequency range 25 mHz to 1.2 Hz. If 8σ excess is shown in more than 50 detectors in any common frequency bin, it is noted as common mode Fourier domain glitches which are notch filtered in next rounds or in the map making stage. This 8σ threshold is subjected to change depending on closer examination of individual detector PSD versus detector number and frequency.

At this point, for the low multipole range, there is an additional round basing on common mode noise in time domain re-calculated from PSDs of detectors passing the second round. Individual detector timestreams are weighted-averaged using the inverse of their PSD variance to produce a common mode PSD. This common mode PSD is then fitted to a noise model $A_0(1+(f_{knee}/f)^\alpha)$ for Q and U separately, where f_{knee} is the frequency where the power spectrum doubles the white noise level A_0. Averaging over focal plane reduces white noise but not the low frequency component. That means the f_{knee} might run higher, hence the power law α is set floating to better fit the common mode PSD. The median knee frequencies are found to be 45 mHz (24 mHz) for Q (U) in the instrument frame. As mentioned in 4.2, this is because the temperature-to-polarisation leakage being approximately out of phase with U. Observations with f_{knee} exceeding 150 mHz (100 mHz) for Q (U) or with explosively high the common mode noise floor are discarded. This cut is not done for high-ℓ data because the common mode noise is seen to only impact the measurement of low-ℓ modes.

In the third round, the cut is based on the noise properties of individual observation maps created using the detector weights saved from the second round and the common mode PSD computed in the third round. The employed TOD filtering options are borrowed from the mapmaking stage described in Section 5.3, but the TOD consisting of Q + iU are kept in the telescope frame i.e not projected into right ascension and declination coordinates. The maps are only resolved in degree pixels. Noise variance of each map is compared to the expectation derived from the individual detector noise weights, yielding a respective map χ^2. Observations don't pass this cut if having too low or high respective χ^2. This round in high-ℓ partially overlaps with the common mode noise cut for low-ℓ. More details on the treatments of noise and glitch in all rounds can be found in [82] and [78].

A final cut is done on observations having fewer than 100 active detectors. This cut results in insignificant change in the dataset as compared to from the treament of the main 3 rounds. The data selection stage has been done several times until the selected data satisfy the validation criteria described in 6.3. Overall, a total of 3391 CES observations from 3 seasons of data are retained in the final mapmaking.

5.3 Mapmaking

After demodulation and downsampling of real data following 4.2, we form single observation maps from selected detector time streams following the same pipeline for low multipole range but with slightly altered filtering options. For simulations of CMB data, we only construct demodulated TOD of the form:

$$d_d(t) = \varepsilon[Q(t) + iU(t)] + \mathcal{N}_d. \tag{5.1}$$

to avoid excessive computational cost from simulating TOD full-sampled at 8Hz and the complication of simulating the entire temperature-to-polarisation leakage effect. The following mapmaking process is applied for both real data and simulated TOD unless otherwise noted.

Data such as pointing and relative gain from calibration steps described in Chapter 4 are first prepared. Deconvolution of time constants for real data is done at this point. For simulations, we need to create non-modulated TOD for each detector. The azimuth and elevation from real pointing data are converted to RA, DEC, and parallactic angle (PA) for each detector using quaternion pointing. The map projection method, which will be noted later, is used early here to get the 2-dimensional pixel coordinate of each pair of RA-DEC of each time sample. Separated from this mapmaking stage, simulated skies are produced by generating a 2-dimensional Fourier frequency array given a chosen sky map width and a chosen pixel size then interpolating a chosen theory spectrum to 2-dimensional T, E, B arrays in Fourier frequency space. The E and B arrays are converted to Q and U arrays using the inverse of 1.36 with the angles constructed from the multipoles calculated from Fourier frequencies at each array entry. The T, Q and U real skies are then created by inverse Fourier transforming respectively the T, Q, U arrays in frequency space. Note that the sky map width is chosen to be significantly larger than the real output projected map width, and the create simulated skies are used for several parts that involve TOD simulations e.g 6.3 and 6.4. Back to mock-scanning for TOD simulations, each sample in the timestream d of each detector at time t is now simply filled in with an T,Q, or U sky entry of matching calculated pixel coordinate following :

$$\begin{aligned}
c &= cos(2 \times PA[t]) \\
s &= sin(2 \times PA[t) \\
d_I[t] &= T[pixel] \\
d_Q[t] &= c \times Q[pixel] + s \times U[pixel] \\
d_U[t] &= s \times Q[pixel] - c \times U[pixel]
\end{aligned}$$

There can be an extra step of adding TOD noise components to simulated signals here following Section 5.4.

Now we have either the earlier demodulated TOD or simulated non-modulated TOD in separated I,Q and U. Each TOD is set for further time domain filtering operations, to mitigate bias due to leakage of temperature to polarisation TOD. In the Fourier domain, notch filters of 10mHz width are prepared and applied to glitches earlier flagged in the data selection stage. We do not perform low pass filters for the high multipole range, while the low multipole treatment applies one at 1.2 Hz here.

For each whole CES, a second order polynomial filter is done to remove spurious signals caused by thermal fluctuations of the focal plane and cryogenics. Next, ground-fixed templates are constructed respectively for I, Q, and U TOD by averaging the telescope frame TOD in $14.'4$ azimuth bin, then subtracted from their respective TOD. Bolometers and CESs have independent templates in this step, while both left going and right-going subscans share the same template.

Following this, we estimate temperature-to-polarisation leakage caused by detector non-linearity and telescope design through a PCA technique similarly demonstrated in [76]. Note that this temperature-to-polarisation leakage effect is introduced earlier in 3.3. We then subtract temperature leakage from the pre-PCA polarisation TOD only for real data. The Q and U TOD for each subscan are filtered with a ninth-order polynomial while the I TOD are left intact in this step. Besides to mitigate low frequency noise, the ninth order is chosen because it is found that this choice makes the estimates of PSDs of the TOD for the high multipole range more stable. Finally, a common mode template is prepared by averaging over all detector timestreams using the inverse of their PSD variance for each of I, Q and U timestreams. The common mode is then subtracted in the respective timestream to remove the low frequency mode present in all detectors.

After the filtering stage, the TOD are projected into $2'$ pixels on the sky using the oblique Lambert equal area (OLEA) projection. This choice of pixel size is optimal because a bigger pixel size or lower resolution will not resolve the power spectra up to the desired highest multipole, while a smaller pixel size or higher resolution will cost more computational time without adding noticeably more precision which is foremost limited by the noise level of POLARBEAR. The choice of map projection is investigated in Chapter 6. The low multipole range analysis used cylindral equal area (CEA) map projection and an $8'$ pixel size. Nevertheless, the coadded maps produced in both analyses are visually identical. Thus, for convenience, I opt to show maps coadded of all observations in Q and U as well as noise maps made with CEA projection in Figures 5.1 and 5.2.

For simulations that contain signals only i.e simulations that do not have TOD noise injected in the TOD simulation step, we can coadd simulated full coadded maps or half-data maps with what we call the "signflip" noise realisations described in 5.4.

Day maps are grouped by every 10 days, resulting 38 splits of the data. Closer examination of the 38 individual maps of real data shows nonuniform and shrinking coverage near the edge due to scan patterns versus the availability of the patch as well as the weighting in mapmaking. This leads to nonuniform weighting of map pixels when taking cross spectra from our set of maps. In addition, the computational cost of forming spectra from 38 maps of both real data and simulations is noticeably high when the maps are remade several times to check for validity of data as described in Chapter 6. Hence, we further combined the 38 maps into 12 map "bundles" with more even and less cut coverage, which also saves time on the post-mapmaking stage.

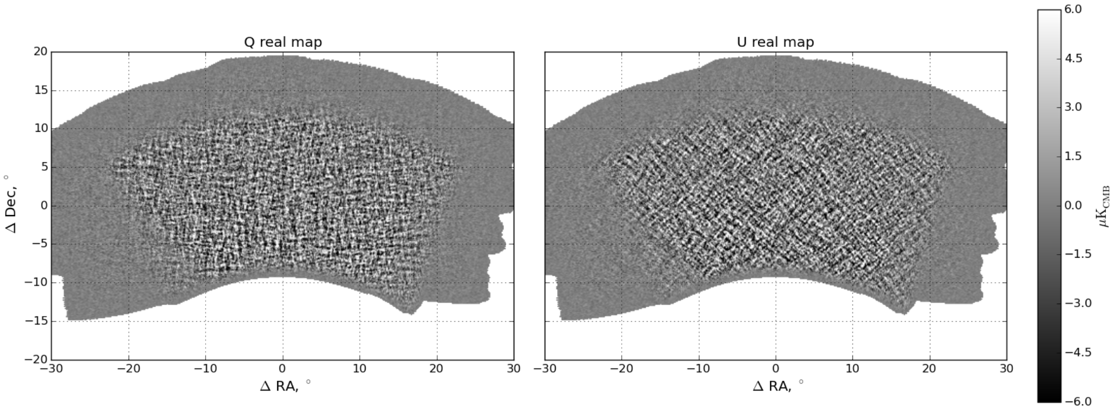

FIGURE 5.1: Maps of Q and U polarisation from coadding all observations in 3 seasons of data. Q map has vertical-horizontal pattern, while the U map has diagonal pattern as a typical characteristic of E-mode maps. The unit is μK_{CMB} per pixel of 8 arcmin. Picture credit: Neil Goeckner-Wald

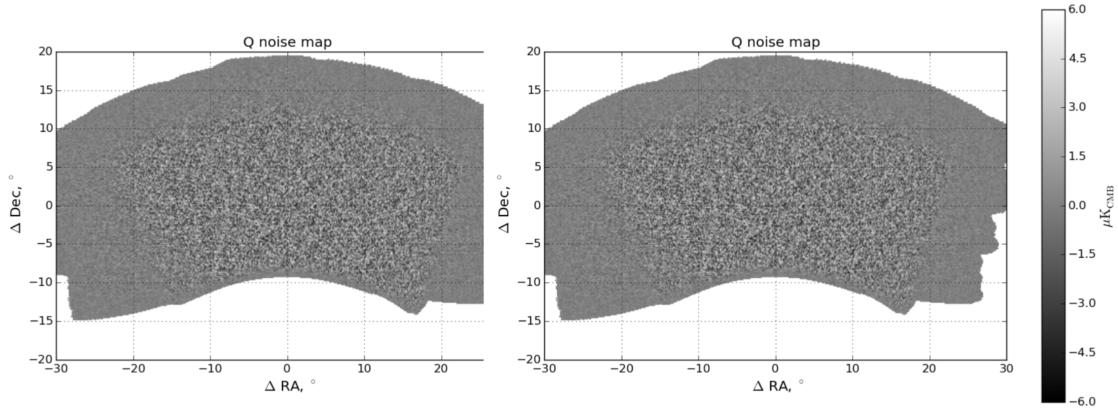

FIGURE 5.2: Noise maps in Q and U polarisation from coadding all observations in 3 seasons of data. These maps don't have visible patterns due to signals having been subtracted out. The unit is μK_{CMB} per pixel of 8 arcmin. Picture credit: Neil Goeckner-Wald

5.4 Notes on noise model

POLARBEAR uses 2 configurations of noise in analysis: TOD noise model and the signflip noise model. The TOD noise model relies on the noise properties of POLARBEAR data at low frequencies found to be well-modeled by

$$P(f) = A_0(1 + (f_{knee}/f)^{\alpha}) \tag{5.2}$$

which is used in data selection earlier described in Section 5.2. In this model, uncorrelated white noise component A_0 is generated for each bolometer using the noise weights produced in Section 5.2. Since the knee frequencies f_{knee} fit from real data are different for Q and U, the common mode low frequency noise components are generated separately for them in telescope frame. Then, these common modes are rotated into the frames of individual detectors using respective detector polarisation angles. Finally, the common modes and the white noise term are added together. In simulation of demodulated TOD, we only add white noise however.

In the "signflip" model, we create random sequences of +1 and -1 multiplicative factors that are assigned to CES maps in the coadding stage of individual observations. All CES maps that have the same sign go to 1 same half, and it is ensured that the total data weights of both halves are approximately equal. The polarisation weights of individual CES are calculated in the data selection stage. This operation should not change the correlation properties of the whole set of data if there is no correlation between CESs. For each sequence of signs, one final signflip map is created by subtracting one coadded half from the other and then dividing by 2. Like real product maps, signflip maps can be used for power calculations using the pipeline described in 5.5. Both models are used for different purposes in our analysis. Chapter 6 shows good agreement between estimates of spectra of noise components produced in these 2 configurations using our power spectrum pipeline described in Section 5.5.

As an extra note on the common mode in TOD noise model and as previously mentioned in 5.2, the U knee frequency distribution differs from the distribution for Q. This is due to different production mechanisms in 2 cases. For Q, the mechanism is assumed to be the leakage from intensity to polarisation or detector gain drifts coupled with the CRHWP synchronous structure. This leakage to polarisation TOD has been described in Chapter 3. For U, the low frequency noise has a phase difference with both the leakage from temperature to polarisation and the CRHWP synchronous structure. The phase difference is supposed to correspond to detector time constant drift.

5.5 Power spectrum

Past the map making stage that concerns the production of maps from real data as well as as simulated maps containing simulated signals and noise, this section describes the stage to produce the final output - the power spectrum pipeline. The power spectrum estimation pipeline has been outlined in [86] and "Pipeline A" in [103]. This pipeline shares many components with the pipeline in [87] and has been configured specifically for high-ℓ analysis. Over all, we first create an apodisation mask. Then we weight our maps with this mask in pseudo spectrum calculation, which follows the cross spectrum formalism in [104]. We correct our pseudo spectra using the MASTER algorithm in [105].

The apodisation mask is created from our full data pixel weight map whose area is wrapped as the intersection of all map bundles. We mask point sources with a $10'$ disk and a $10'$ cosine taper in our full data pixel weight map. The point sources are from Planck [99]. Then we apply on this weight map an $8°$ cosine square edge taper and an $8°$ Hamming window to the weight map before zero-padding for the final apodization mask. The pseudo power spectrum is formed as the cross spectrum between map bundles to remove uncorrelated biases from individual bundles following

$$\tilde{C}^{XY} = \frac{1}{\sum_{i\neq j} w_i w_j} \sum_{i\neq j} w_i w_j \mathbf{m}_i^X \mathbf{m}_j^{Y*} \tag{5.3}$$

Here, $\mathbf{m}$ and w denote respectively Fourier transformed map and weight mask of each map bundle. For 12 map bundles weighted with the same apodisation mask, the final pseudo-spectra are the average of 66 cross spectra. The pseudo-spectrum is calculated up to multipole $\ell = 3500$ and averaged into bins of size $\Delta\ell = 10$. We take the sum of auto pseudo spectra of map bundles minus the cross pseudo spectrum $\tilde{C}^{XY}$ as the noise pseudo spectrum $\tilde{N}^{XY}$.

We further average the pseudo spectrum into bandpowers of wider bins, which are to be shown in our bandpower results and null tests, and correct into the true underlying power spectrum on the sky:

$$\hat{C}_b = \sum_{b'\ell} \mathbf{K}^{-1}_{bb'} \mathbf{P}_{b'\ell} \tilde{C}_\ell, \tag{5.4}$$

$$\mathbf{K}_{bb'} = \sum_{\ell\ell'} \mathbf{P}_{b\ell} \mathbf{M}_{\ell\ell'} F_{\ell'} B^2_{\ell'} \mathbf{Q}_{\ell' b'}. \tag{5.5}$$

Here, both $\mathbf{P}$ and $\mathbf{Q}$ are binning and interpolation operators. The binning step now weights the modes by the number of modes for each multipole in a bin. Mode coupling matrix $\mathbf{M}_{\ell\ell'}$ accounts for mixing of multipoles due to limited sky coverage. We use the previously made apodisation mask to build our mode-mixing matrices $\mathbf{M}_{\ell\ell'}$ analytically following the description in Appendix A of[105]. The filter transfer function $F_{\ell'}$ is calculated in a similar way as in [86].

$$F^n_\ell = F^{n-1}_\ell + \frac{\tilde{C}_\ell - \sum_{\ell'} \mathbf{M}_{\ell\ell'} F^{n-1}_{\ell'} C_{\ell'} B^2_{\ell'}}{C_\ell B^2_\ell}, \;\; F^0_\ell = 1. \tag{5.6}$$

but pipeline has been modified so that the transfer function is stable after the first iteration. The filter transfer function is calculated from 192 simulated maps that are scanned from 192 simulated skies and then processed through the filtering operations in the mapmaking stage. The $1'$ pixel simulated skies contain temperature signal and either ΛCDM EE-only or BB-only and are generated from the *Planck* 2015 baseline TT,EE,TE+lowE+lensing ΛCDM cosmology [14] with $r = 0$. The BB theory spectrum returned by CAMB[1] is however non-zero. To get EE-only or BB-only simulated skies, the EE or BB theory spectrum is thus set to zero. The theory spectra are used as the input to create simulated skies as described in 5.3. The theoretical spectra are converted into the binned spectra comparable to our bandpowers via the band power window functions $\mathbf{w}_{b\ell}$,

$$\hat{C}_b = \sum_{\ell} \mathbf{w}_{b\ell} C_\ell, \tag{5.7}$$

[1]https://camb.info/

$$\mathbf{w}_{b\ell} = \sum_{b'\ell'} \mathbf{K}^{-1}_{bb'} \mathbf{P}_{b'\ell'} (\mathbf{M}_{\ell\ell'} F_{\ell'} B^2_{\ell'}). \tag{5.8}$$

We have validated the mode mixing matrix and the filter transfer function by checking that the errors contributed from our pipeline are insignificant when using this debiasing operation for different underlying cosmologies for simulations as described in the Section of Pipeline validation in Chapter 6. The statistical uncertainties on the corrected power spectrum are calculated analytically following:

$$\delta \hat{C}^{EE}_b = \sqrt{\frac{2}{\nu_b}(C^{EE}_b + \hat{N}^{EE}_b)} \tag{5.9}$$

where ν_b denotes the effective number of degrees of freedom in bandpower b:

$$\nu_b = (2\ell_b + 1)\delta\ell f_{sky,eff} \tag{5.10}$$

The effective fraction of sky $f_{sky,eff}$ varies for signal-dominated and noise-dominated cases respectively following:

$$f_{sky,signal} = f_{sky,total} \frac{w_2^2}{w_4} \tag{5.11}$$

$$f_{sky,noise} = f_{sky,total} \frac{w^2}{w_2} \tag{5.12}$$

where w,w_2,w_4 stand respectively for weight functions for noise, signal and total weights. All the weight functions are based on the inverse of the pixel variance weights which are calculated from the apodisation masks during the computation of the E-polarisation spectrum.

We also derive the statistical uncertainties as the standard deviation of unbiased power spectra from our set of Monte Carlo (MC) simulations containing ΛCDM sky signal plus noise and processed with our map making pipeline. The results computed in both ways are found to be consistent with each other. Note that we assume BB power is minute compared to EE, hence ignore power leaked from B to E due to mode coupling. The unbiased spectra are presented as $D_\ell \equiv \ell(\ell+1)C_\ell/(2\pi)$ unless otherwise noted.

5.6 Band power covariance

Bandpower correlations and uncertainties sneak into the estimation of parameters through our estimate of E-mode power spectrum with POLARBEAR data. To quantify them, we build a bandpower covariance matrix $C_{bb'}$ from signal variance due to limited sky coverage and noise variance due to the instrument and atmosphere.

Because of non-unity absolute calibration factor, we calculate sample variance and noise variance separately. For sample variance, we create a sample covariance matrix for bin size $\Delta\ell = 50$ from 192 mock-observed noiseless simulated maps previously made for the transfer function.

For most parts, we adopt the method in [6] to create a common conditioned correlation matrix. For noise variance, we create a similar matrix from absolute-calibrated spectra from 192 signflip noise maps. Two diagonals of the two covariance matrices are added together into one single arrays of diagonals set aside. The matrices are normalised into correlation matrices, whose mean is used as a common correlation matrix subjected to next treatments. Due to near-zero mode coupling between any pair of far-away bandpowers, we average entries the same distance away from the diagonal similarly as in [6] and zero all entries that are 3 entries away from the diagonal. This conditioned correlation matrix is multiplied with the set-aside diagonal values to reconstruct the final bandpower covariance matrix. We apply the binning operator $\mathbf{P}$ to get the covariance matrix for our customized binning.

We do not incorporate POLARBEAR beam uncertainties in the covariance matrix but implement them during parameter estimation. Given a set of planet observations for calibration, we first create a beam correlation matrix by first pivoting the individual observation beam profiles with their values at $\ell = 1000$, then taking the ratios of beam profiles and the pivoted mean effective beam profile, and finally taking the weighted covariance of the normalised beam profiles with the errors from beam calculations. This matrix, ranged from $\ell = 1$ to $\ell = 3500$, is then binned into the final binning configuration by the same binning operators used in our band power making step. We add this final beam correlation matrix $C_{bb'}^{beam}$ to our conditioned covariance matrix following:

$$C_{bb'}^{all} = C_{bb'} + C_b \cdot C_{bb'}^{beam} \cdot C_{b'} \tag{5.13}$$

where C_b is the transpose of the theory bandpower $C_{b'}$.

Chapter 6

Data validation

6.1 Overview of validation

This chapter describes the validations of 2 components used to produce the final power spectrum and the estimation of systematics contaminations onto the final power spectrum: the established pipeline and the selected data. Data validation is performed by running null tests to ensure that our data are optimally free from bias after data processing. We also estimate the bias from known systematics, finding that the contamination to the final power spectrum is negligible. The pipeline validation aims to check possible bias brought by the power spectrum estimation or bugs introduced in map making. As detailed in Chapter 5, after the data selection stage, the whole pipeline goes from the map making stage to the final power spectrum stage. While we can visually explore the produced maps, it is compulsory to ensure the end-to-end power spectrum calculation is unbiased. Thus, I validate the power spectrum pipeline using simulations before applying it to real data.

6.2 Power spectrum pipeline validation

The power spectrum pipeline consists of the making of pseudo spectra, and the debiasing of these pseudo spectra with mode coupling matrices and filter transfer functions as described in Chapter 5. The validation of this part of the pipeline is divided into the inspection of the pseudo power spectrum making, the validation of the debiasing duo, and the validation of the entire power spectrum pipeline.

6.2.1 Pseudo power spectrum and effects of projections

The pseudo power spectrum step takes 2 dimensional Fourier transforms of the Q and U maps, and converts these Fourier transforms into the Fourier transforms of E-mode and B-mode maps. We choose to test the pseudo power spectrum calculation with regards to different map projections because they directly decide how the TOD are mapped into 2D grids, which are the immediate inputs for this calculation. Thus, this step is checked by mock-scanning simulated skies that contain signal only without going through the filtering options so as to decouple from the filter transfer correction step, meaning the debiasing operation in 5.5 is not used in this test. The effect of mode coupling due to finite map widths is not corrected but should cause only percent level errors.

To obtain the results, 8 simulated curved skies with pixel size of approximately $0.43arcmin$ produced from the same theory spectrum in 5.5 using Healpix package [106] with $nside = 8192$ are scanned for 8 set of TODs. The process of mock-scanning is identical to that described in 5.3, except that pairs of RA-DEC are converted to pixel addresses $[pixel]$ using Healpix's method. The simulated TOD are then projected into flat sky 50×50 maps with $2'$ pixels using one of 2 projection methods: Oblique Lambert Equal Area (OLEA) projection or Lambert Cylindreal Equal Area (CEA) projection. This results in 16 projected maps (2 methods $\times$ 8 simulations each), and thus 16 pseudo spectra. Those made with the same map projection are averaged together. The average pseudo spectra produced using the 2 projections are then compared to each other. Note that different projections also lead to different weights projected into of each pixel. This results in 2 different weight masks, which are apodised prior to Fourier Transformation as in Chapter 5. Another handy comparison can be done by generating flat skies from 1 single theory spectrum then using these 2 weight masks to get 2 pseudo spectra from 1 common set of flat skies. The projections should cause no anomalies in weight masks that can cause significant difference between 2 pseudo spectra. The results are shown in Figure 6.1, proving the pseudo spectrum making step is stable with respect to considered map projections.

It is of interest to explore how much the projections can independently contribute to errors of power spectrum calculation. This part is done independently from the power spectrum pipeline as it does not involve running POLARBEAR simulation pipeline to project TOD into maps. Instead, one simulated full sky is produced at $Nside = 8192$ using Healpix package. The coordinates of pixels in this curve sky are projected directly into flat maps with OLEA and CEA projections. Because only the coordinates are projected while the signals are neglected, this check does not involve the map making pipeline. The distances of the points in curve sky coordinates and in flat sky coordinates

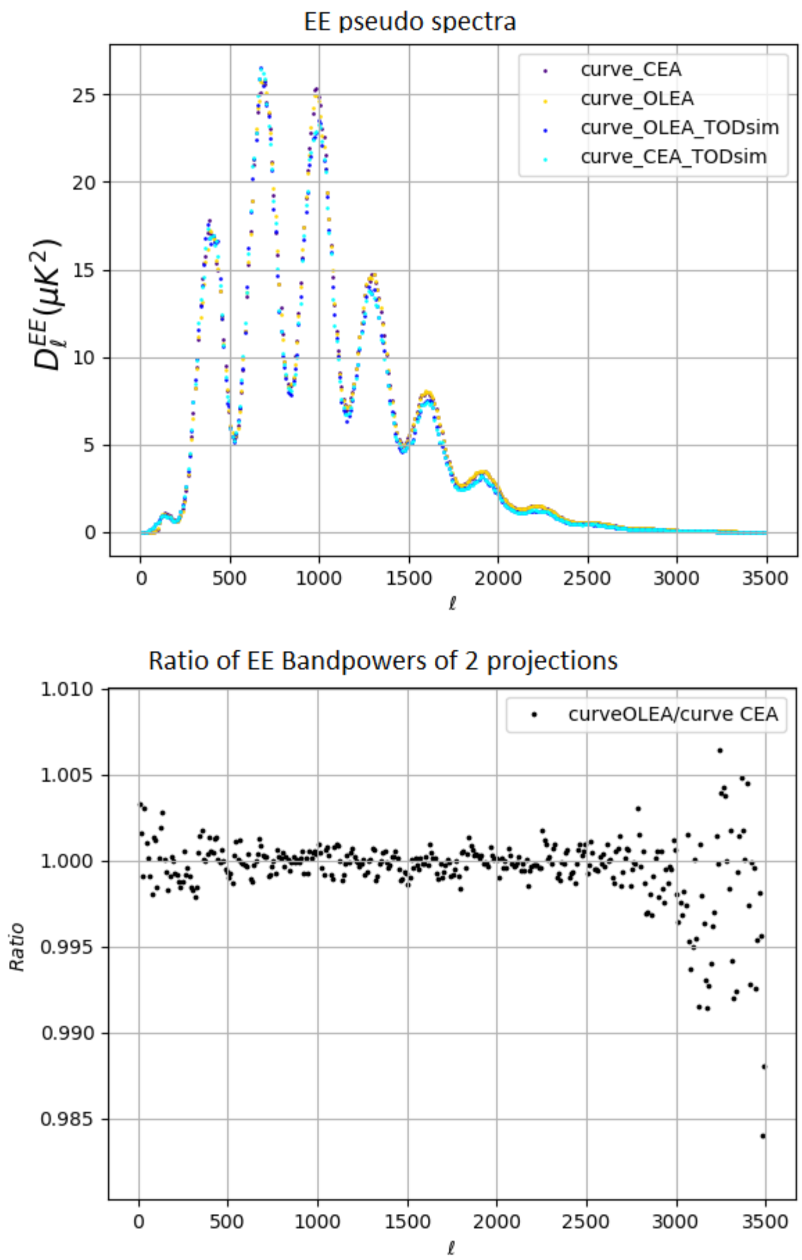

FIGURE 6.1: Up: 'Blue' and 'cyan' are average pseudo spectra from 2 cases of maps made with simulated TODs projected in 2 methods. 'Purple' and 'gold' are average pseudo spectra from 2 cases of simulated skies not mock-scanned but only apodised with weight masks produced from 'blue' and 'cyan' maps . 'Purple' and 'gold' are expected to have higher acoustics peaks because the maps only undergo 1 time of sampling i.e sky generation, while the 'blue' and 'cyan' undergo 2 times i.e curve sky generation and mapping resulting in more power nulling in higher multipoles. 'Curve' denotes that the TOD is scanned from curve sky. Down: The ratio of 'blue' and 'cyan' spectra shown in the left-hand side plot. The increased fluctuation at $\ell < 100$ is due to the limited number of large modes in this multipole range due to limited map size. The excessive noisy $\ell > 3000$ is due to the resolution of the maps being only 2 arcminute pixels. As expected, the ratio is consistent with unity over all.

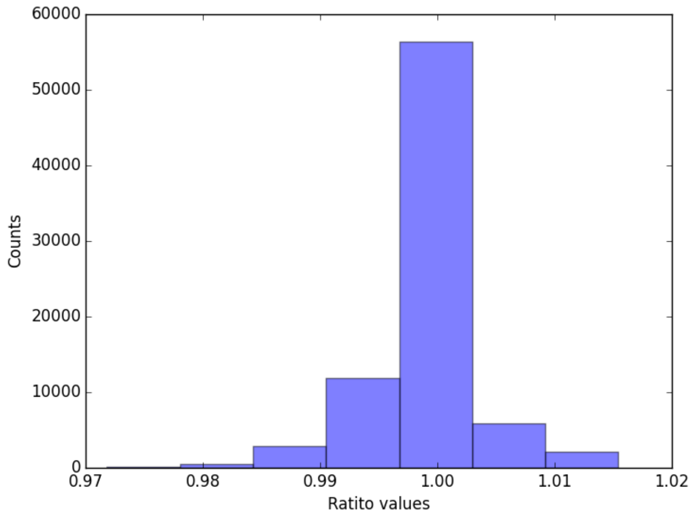

FIGURE 6.2: Distribution of the ratios of curve sky distances and flat sky distances mapped with CEA projection. The standard deviation is $\sigma = 0.00243$, which is higher than for OLEA, $\sigma = 0.00163$. The distribution is expected to center around unity. The slight skewness can be reduced by using a curved sky resolution much smaller than the resolution of the flat maps.

are then calculated. The ratios between curve sky distances and flat sky distances can thus be calculated and plotted into distribution as in Figure 6.2.

This has been done for both OLEA and CEA. Note that distance distortion translates into under- or over-estimation of mode sizes. Assuming Gaussianity, we will estimate power of modes to be smaller or larger than their true values. Hence the distribution of distance ratio can roughly be converted into the distribution of ratios of distorted power spectrum estimates versus true powers. The standard deviation with CEA, $\sigma = 0.00243$ is found to be higher than for OLEA, $\sigma = 0.00163$, meaning we should opt for OLEA in final map making and concentrate on additional checking for this method. The standard deviations are used to create kernels of distortion mixing adjacent modes. This results in errors in power spectrum estimation via:

$$C_l^{distorted} = C_l \cdot K_{ll'}^{distort} \tag{6.1}$$

where $C_l^{distorted}$ is the power spectrum after distortion at each multipole, C_l is the true power, and $K_{ll'}^{distort}$ is the distorting kernel. These 2 power spectra are shown in Figure 6.3.

This result shows that the map projections have minor effects on E-mode power spectrum estimation for the POLARBEAR survey region size. The specific numerical values or the deviations between 2 spectra are found to be less than 5% of the POLARBEAR's statistical error bars calculated following the description in Chapter 5. The statistical

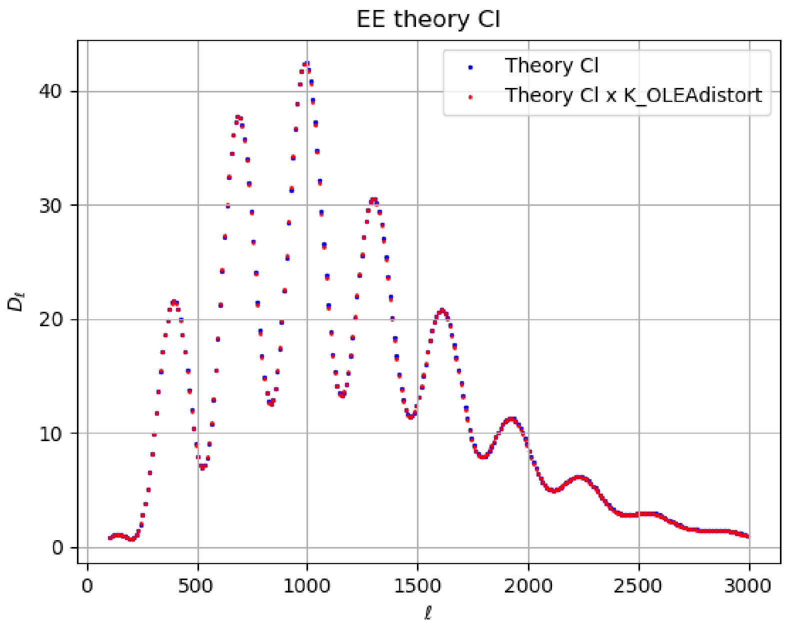

FIGURE 6.3: Comparison of the original theory power spectrum in blue versus the power spectrum in red after distance distortion. Visually, the distorted power spectrum is minimally different from the true theory power spectrum.

errors of the POLARBEAR E-mode bandpowers for different binning configurations can be found in Section 6.2.4 and Section 7.1.

6.2.2 Validation of mode coupling matrices and transfer functions

Now that I have ruled out distortions due to the flat-sky projection as a significant issue, I turn to validate the debiasing step. The test means to ensure that the mode coupling matrix and transfer function calculation introduce insignificant error to any corrected bandpowers regardless of the cosmology implied by the bandpowers. This can be done on mode coupling matrices $\mathbf{M}_{\ell\ell'}$ derived for maps made with any dataset or subset, but is opted directly for POLARBEAR's data. Thus, we calculate the mode coupling matrix from POLARBEAR's full data weight mask. Note that this mode coupling matrix is also used to correct the final power spectrum output of POLARBEAR. The test is done as followed.

The action of mode coupling and filter transfer function can be tested using different cosmologies. Four theory spectra are generated using the CAMB package [107] with cosmological parameters obtained from Planck spectra [14] fitting with 4 different models. The chosen models include 1 best-fit ΛCDM with 6 parameters and 3 other cosmological models extended from ΛCDM :

- Best fit ΛCDM

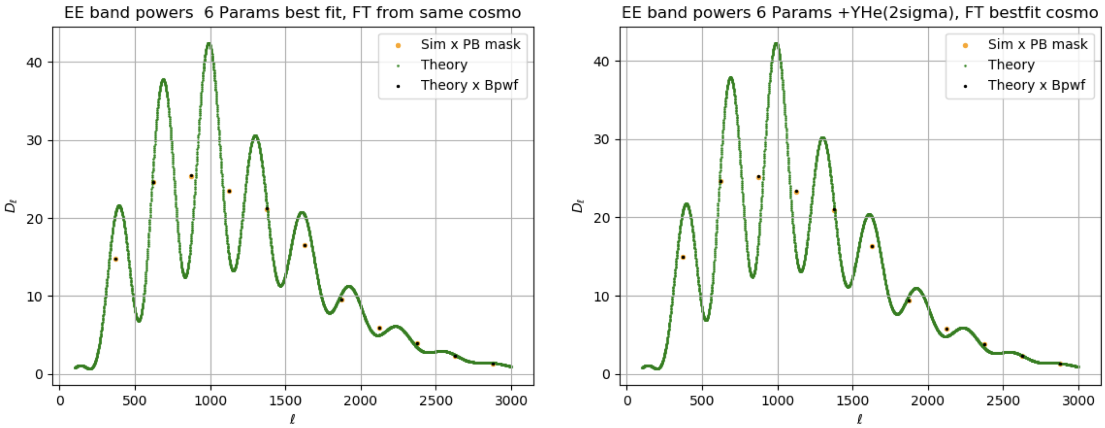

FIGURE 6.4: Left: Plot shows the theory spectrum for ΛCDM with 6 parameters resulting from best-fitting with *Planck* 2015 data [14], the respective theory bandpowers, and the average debiased spectrum calculated from related simulated skies apodised with POLARBEAR real data weight map. The filter transfer function (FT) is produced from this same set of simulated skies. Right: Plot is the same as left-hand side, except the model is ΛCDM extended with Y_{He}, whose value is the central value plus 2σ from best fitting of *Planck* 2015 with this extended model. The filter transfer function is shared with spectra on the left-hand side. Visually, the filter transfer function unmatching with the cosmology theory produces minimal deviations between the theory bandpowers and the debiased simulated bandpowers.

•ΛCDM+ Y_{He}

•ΛCDM+ $Y_{He} + N_{Eff}(2\sigma)$

•ΛCDM+ $Y_{He}(2\sigma) + N_{Eff}$

In all these models, all parameters take the central values as best fit with Planck data, except those with 2σ notion take values 2σ higher than the central values. Note that, for the purpose of this test, any number of any models plus extensions can work. All relevant parameters have been described in 1.5. From each theory spectrum, 40 signal-only simulated flat skies are generated then passed onto the pseudo spectrum making step. Simulating at the map level instead of TOD level reduces the computational cost. While these skies are not filtered, it is valid to create filter transfer functions from them using the pipeline because the debiasing step is meant to correct for any power loss due to whether filtering or mapping. In other words, this aims to test the functionality of the modules instead of the quality of the filtering for POLARBEAR data. To see the effect of the filter transfer function regardless of the cosmologies, only 1 cosmology has its filter transfer function calculated. All sky pseudo spectra are then debiased using the same $\mathbf{M}_{\ell\ell'}$, $F_{\ell'}$ and beam function $B_{\ell'}$. To compute theory bandpowers, theory spectra are convolved with the band power window function (BPWF) created with the same $\mathbf{M}_{\ell\ell'}$, $F_{\ell'}$, $B_{\ell'}$ following Chapter 5. Figure 6.4 show 2 cases of average debiased spectra and theory bandpowers.

The mean debiased simulated bandpowers are visually close to the theory bandpowers.

TABLE 6.1: Total χ^2 and PTEs for 4 different cosmologies

Cosmology	Best fit ΛCDM	ΛCDM+ Y_{He}
Total χ^2	0.008	0.54
1 - PTE	5.31E-12	8.51E-05
Cosmology	ΛCDM+ $Y_{He} + N_{Eff}(2\sigma)$	ΛCDM+ $Y_{He}(2\sigma) + N_{Eff}$
Total χ^2	0.46	0.33
1 - PTE	4.75E-05	1.25E-05

The theory spectra are generated using the central values of all parameters, except in cases where the notion of 2σ means the parameter value is the central value plus 2 times of the standard deviations in parameter constraints with Planck data. The numerical values of (1- PTE) are shown instead since the PTEs in all cases closely approach unity.

However, to evaluate the goodness of the debiasing step, I compare between these 2 bandpowers using the χ^2 of the difference:

$$\chi^2 = (\frac{C_l^{Theory} * BPWF - Mean(C_bSim)}{\sigma(C_bSim)})^2 \tag{6.2}$$

Here, $C_l^{Theory} * BPWF$ is the theory bandpowers, C_bSim is the bandpowers from simulated skies, and $\sigma(C_bSim)$ is the standard deviation of the simulated bandpowers. Because it is not certain what cosmology POLARBEAR or any CMB experiment implies, the filter transfer produced from a cosmology will introduce errors to the bandpowers should the bandpowers imply a different cosmology. Thus, I derive the respective Probability-to-exceed (PTE) to quantify the significance of errors generated by a filter transfer function that is not matching the cosmology. The results are shown in Table 6.1. The total χ^2 is less than 1 for the number of degree of $Ndof = 11$, which is sufficiently small. The PTE for Best fit ΛCDM is tiny as expected given that the filter transfer function is calculated from the spectrum for this cosmology. Over all, the small PTEs show that while the filter transfer function is produced from a single given cosmology, the bias introducing in this debiasing step is negligible regardless of what cosmology produced the (simulated) maps.

6.2.3 A separate check on the filter transfer function calculation

Given that the precision of this debiasing step is related to the precision of the filter transfer function step, I have also rechecked the algorithm to calculate the filter transfer function. As noted in Chapter 5, the filter transfer function $F_{\ell'}$ is calculated as:

$$F_\ell^n = F_\ell^{n-1} + \frac{\tilde{C}_\ell - \sum_{\ell'} \mathbf{M}_{\ell\ell'} F_{\ell'}^{n-1} C_{\ell'} B_{\ell'}^2}{C_\ell B_\ell^2}, \tag{6.3}$$

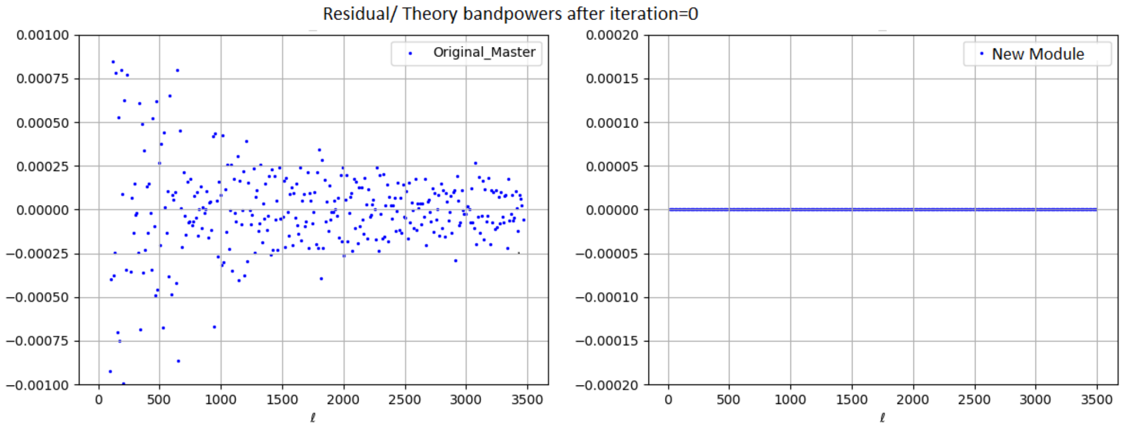

FIGURE 6.5: Left: Ratios of the residuals versus the theory bandpowers calculated using the original pipeline. Right: Ratios of the residuals versus the theory bandpowers calculated using the new module.

where $\tilde{C}_\ell$ is the true power spectrum of the sky, $C_{\ell'}$ is the power spectrum calculated from simulated maps and not yet correct, $B_{\ell'}$ is the beam profile to correct for the finite beam effect on the pseudo spectrum from real or simulated data. Given that the mode mixing matrix $\mathbf{M}_{\ell\ell'}$ is set by the POLARBEARfull map, the precision of the filter transfer function depends foremost on the calculation of $F^0_{\ell'}$ from this equality :

$$\tilde{C}_\ell = \sum_{\ell'} \mathbf{M}_{\ell\ell'} F^0_{\ell'} C_{\ell'} B^2_{\ell'}, \tag{6.4}$$

This calculation requires matrix inversion, so its stability is questionable. Hence, I have written another module for filter transfer function calculation to compare with the module already existing in the original pipeline. These 2 modules can be compared via the difference of the right hand side with respect to the left hand side of Equation 6.4, where the filter transfer function has been computed and is now plugged back in the right hand side. The ratios of the residuals versus the theory bandpowers are shown in Figure 6.5. The new module is seen to yield smaller residuals, which mean higher precision. However, when these 2 filter transfer functions computed with 2 modules are used to debias a same set of 96 simulated pseudospectra, the total χ^2 of 2 average debiased spectra with respect to theory bandpowers are 0.24 from the new versus 0.28 from the old module for 25 multipole bins, which are not significantly different. I expect that it is because the number of simulated spectra (which also contributes to the precision of the output filter transfer function) is not large enough to compensate for the limited number of modes in each angular multipole bin i.e. the errors coming from the original filter transfer function modules are already tiny compared to the uncertainties from the modes. The new module is used in final bandpower making however because it does not require iterations like the old one and a minor improvement is better than none. Now that the debiasing pipeline has been validated irrespective of the map making pipeline, the next step is to check the stability of the whole power spectrum pipeline with regards to map making outputs.

6.2.4 Whole pipeline validation

Validating the power spectrum pipeline in conjunction with mapmaking needs to be done without opening the box i.e without seeing the actual E-polarisation power spectrum of POLARBEAR data. This can be done by exploring the estimates of noise produced using the "signflip" noise configuration described in Chapter 5.

By this point, maps have been produced for all individual real observations. From the real maps, I create 74 null "signflip" maps. The signflip maps are created following the filtering-inclusive procedures described in 5.3 and 5.4. All signflip maps are used to calculate noise PSDs, the average of which is then used to create 74 noise sky realisations. Since the standard deviation is inversely proportional to the square root of the number of maps, using 64 maps can yield a noise estimation that is on average at maximum 12.5% away from the true estimation of noise spectrum. Surely, a higher number of maps means more accuracy. Number 74 is randomly chosen because it is not computationally costly, and I expect that it is sufficient to show that the mean noise spectra resulting from 2 cases are 10% within each other. All sky realisations and signflip maps have the same size as our full coadded real map. One set of simulated maps is also produced using the simulation mapmaking pipeline including filtering options, described in Chapter 5, and coadded into a single full simulated map. The full map is added separately to each of 74 signflip maps and 74 noise sky maps. Only 1 set of simulated maps is needed because the E-mode bandpower calculations from simulations have been described in e.g 6.2.2, and we are attempting to check the pipeline via estimation of errors from real data. Power spectra are created from 74 signflip noise + simulated signal maps and 74 PSD noise + simulated signal maps and debiased with the debiasing modules following 5.5. The standard deviations of 2 sets of debiased spectra are the bandpower errors which can be compared to each other. The result is shown in Figure 6.6. For a single multipole bandwidth of $\Delta\ell = 250$ over a range of $\ell = 500 - 3000$, there are 10 bands. It can be seen from the ratios of bandpower errors that there is no bias where one case results in overall higher estimates than the other. In addition, the estimates for each multipole band in both cases are within 10% of each other. Thus, the bandpower errors produced in both cases are consistent with each other. This validates 2 ways of estimating errors and shows the stability of power spectrum pipeline with respect to mapmaking outputs.

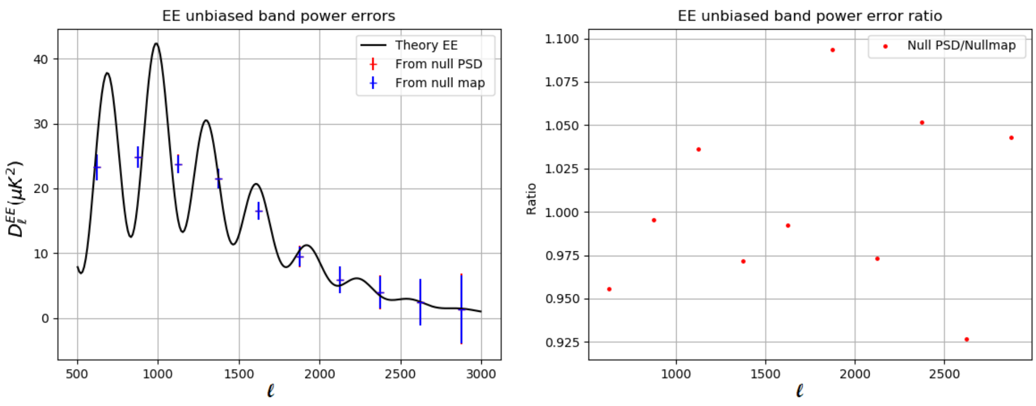

FIGURE 6.6: Left: Bandpower errors are plotted with the theory spectrum from the best fit *Planck* 2015 ΛCDM in [14]. Red is for maps with noise generated from PSD. Blue is for maps with noise components coming directly from the null "signflip" maps. Right: The ratios of red over blue bandpower errors. Here, the multipole bandwidth is $\delta\ell = 250$.

6.3 Null tests

With the power spectrum pipeline validated, I next turned to the real data. To look for unknown unknowns, I apply a set of null tests to the real data. Absent biases, the power spectra of these nulls should be consistent with zero.

6.3.1 Framework

In null tests, the data are split into 2 halves, which are chosen to maximise the sensitivity to possible sources of bias. The power spectrum of the difference between these two halves are calculated:

$$\hat{C}_\ell^{\text{null}} = \hat{C}_\ell^A + \hat{C}_\ell^B - 2\hat{C}_\ell^{AB}, \tag{6.5}$$

where $\hat{C}_\ell^A$ and $\hat{C}_\ell^B$ ($\hat{C}_\ell^{AB}$) are the autospectrum for each half of the split (the cross spectrum between the splits) after debiasing with filter transfer functions and mode mixing matrices. As mentioned in 5.3, one single common apodisation mask is used for all map bundles in 1 dataset. Splitting data into 2 halves further reduces the usable area of each map bundle because the areas where weights are high pre-division can be come low post-division and might tend to zero due to apodisation. If every bundle is zeroed out (due to very low weights) in different directions, the area of the common apodisation mask (which takes in overlapping areas of all submaps) can be greatly reduced, meaning a large percentage of data are not weighted i.e. not taken into cross spectrum calculations. Leaving out a big portion of data makes null tests unmeanningful. Thus, the maps of each real or simulated half are re-bundled into between 10 and 19 submaps to maximise overlapping area, then used to take cross spectra with one single common apodisation mask. This framework for null spectra $\hat{C}_\ell^{\text{null}}$ is used in [86], [103], and based on the formalism developed originally by the QUIET collaboration [108].

The filter transfer functions are calculated from 48 simulated maps mock-observed from 24 EE-only and 24 BB-only *Planck* 2018 ΛCDM input skies for each test. I choose 24 foremost due to the computational cost. In addition, the simulated maps and the real maps are subjected to the same bias from these filter transfer functions, so the final statistics are not impacted. Of equal importance, this is within my computational budget. The null spectra need to have the same ℓ binning configuration as for the final power spectrum.

My run of null tests produces EE, EB, and BB null spectra, but I will emphasise the results for EE more due to their direct relevance to the parameter constraints. I obtain null spectra from real data and 48 $EE + BB$ signal plus noise simulations. The noise term is generated following the TOD noise model, which does not include an additional anticorrelated noise term that exists when detector pairs are separated and is seen in some null tests of real data. I thus remove the anticorrelation terms that exist in the calculation of $\hat{C}_\ell^{AB}$ for both real maps and simulated maps.

The suite of null tests consists of 19 splits. The descriptions of 14 of them are borrowed from [102]:

- First half versus second half: the dataset is split into two equal-weight halves chronologically to probe for time-dependent changes in the instrument, such as drifting calibration.
- Middle versus rising and setting: the three different CES types are split in middle range elevation scans versus rising plus setting scans to detect, for example, elevation-dependent miscalibration or residual ground synchronous signal.
- Left-going versus right-going subscans: the dataset is split in half according to the direction of motion of the telescope to test for, for example, microphonic or magnetic pickup in the data.
- High gain versus low gain observations: the dataset is split into observations with above and below average mean detector gain coefficients to search for problems with the gain calibration.
- High PWV versus low PWV: the dataset is split by PWV as measured by the nearby APEX radiometer to check for loading or weather dependent effects.

- Mean temperature to polarisation leakage by channel: split the dataset into detectors that see small and large temperature leakage coefficients to test the subtraction and search for residual contamination.

- $2f$ amplitude by channel, $4f$ amplitude by channel: split the data by HWP signal amplitude to check for problems removing the HWP structure or systematic contamination coupling into the data through these terms.

- Q versus U pixels: each detector wafer is fabricated with two sets of polarization angles. We split the data into the two pixel types to check for problems in the device fabrication.

- Sun above or below the horizon, Moon above or below the horizon: we split observations based on whether or not the sun or moon is up to check for residual sidelobe contamination.

- Top half versus bottom half, left half versus right half: we split detectors by the boresight axis of the telescope to check for optical distortion and problems due to far sidelobes.

- Top versus bottom bolometers: with a continuous HWP each bolometer TOD independently measures Q and U. We explicitly separate detector pairs[1] to check for temperature aliasing or device mismatch.

The other 5 splits are:

- Mean temperature to polarization leakage by CES: split the dataset into CESs that see small and large temperature leakage coefficients to test the subtraction and search for residual contamination.

- $2f$ amplitude by CES, $4f$ amplitude by CES: split the data by HWP signal amplitude for CES to check for problems removing the HWP structure or systematic contamination coupling into the data through these terms.

- Low distance or high distance from the Sun: we split observations based on the distance to the Sun to check for residual sidelobe contamination.

- Random splits of bolometers: We randomly split bolometers into 2 halves to check for temperature aliasing or device mismatch.

The suite of null tests were also selected with regards to the correlation between tests. This correlation can depend on the number of observations that 1 half of a specific null

[1]Two bolometers coupled to the same slot-dipole antenna belong to the same detector pair.

test shares with any half of another null test. The problem of noise correlation between bolometers that resulted in non-zero null spectra shown in early trials of null tests for the high-ℓ multipole range also demands more inspection by additional less-correlated null tests.

For each null test, if there is no bias, the signals estimated for each half and for the cross term should be the same after the debiasing step, meaning that the null spectra will have only noise left since the signals are canceled out. The sanity of the null spectra can examined as followed.

For each bin in each null spectrum, we define $\sigma_{MC}(\hat{C}_b^{\text{null}})$ as the standard deviation of the Monte Carlo (MC) simulated null spectra. The statistics χ_{null} and χ^2_{null} are determined from:

$$\chi_{\text{null}} \equiv \hat{C}_b^{\text{null}} / \sigma_{MC}(\hat{C}_b^{\text{null}}) \tag{6.6}$$

We compute χ_{null} and χ^2_{null} for both real data and 48 MC realisations. While stopping at 48 MC should not affect any results, it is preferable to draw more random samples if the covariance information of the already existing distribution and the mean value of the distribution are available. I thus project these 2 statistics from MC into a larger sample population of 10000 by using the methods in Numpy[2] on the mean χ_{null} and the covariance matrix of the simulated χ_{null} values. This results in 10000 MC sets, each of which has 25(bins) $\times$ 19(tests) χ_{null} values. The total χ^2_{null} can be taken along the axis of test or bin or both test and bin for real data or for each set of projected χ_{null}. The Probability-to-exceed (PTE) is calculated by the fraction of this 10000 population that have χ_{null} or total χ^2_{null} above the respective values from real data.

6.3.2 Null test results

Visual inspection of null spectra for both real data and simulated shows no significant issue in real data. Figure 6.7 shows an example of null spectra for both EE and BB for the test "4f amplitude by CES": The resulting PTEs for both tests and bins are shown in Table 6.2. We do not require but expect the χ_{null} for real data for all tests and bins to follow Gaussian distribution. This expectation is true with the P-value from Kolmogorov-Smirnov (KS) test being 0.22. The fitting of χ_{null} from POLARBEAR data with Gaussian distribution is shown in Figure 6.8. The minimum threshold for the PTE of each test or bin was loosened to be 0.2%, which relates to 3σ. The reason is the deviation of a bin or test for both real or simulated spectra from the mean of the distribution corresponding to simulated data can be at the order of 3σ when we use a sufficient number of tests or simulated maps. Note that, for each test, 48 simulated maps

[2] https://numpy.org/

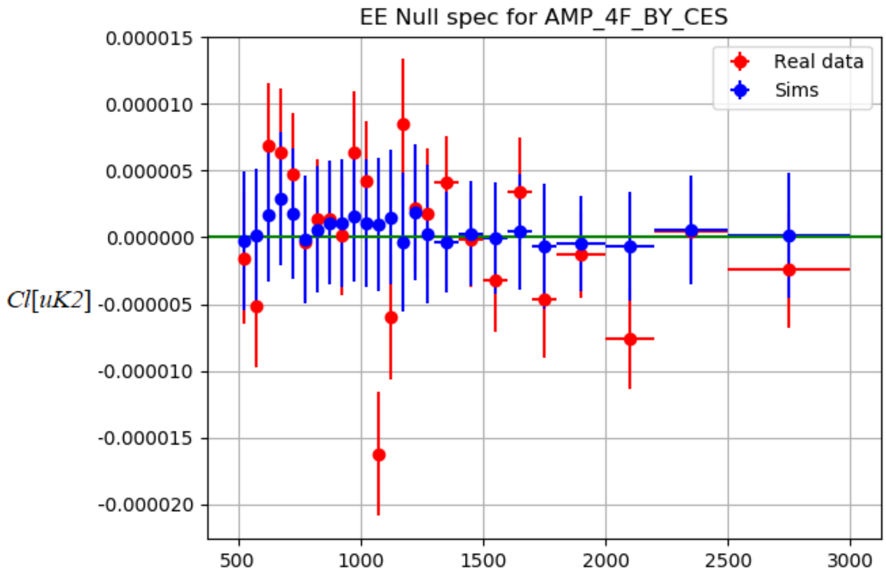

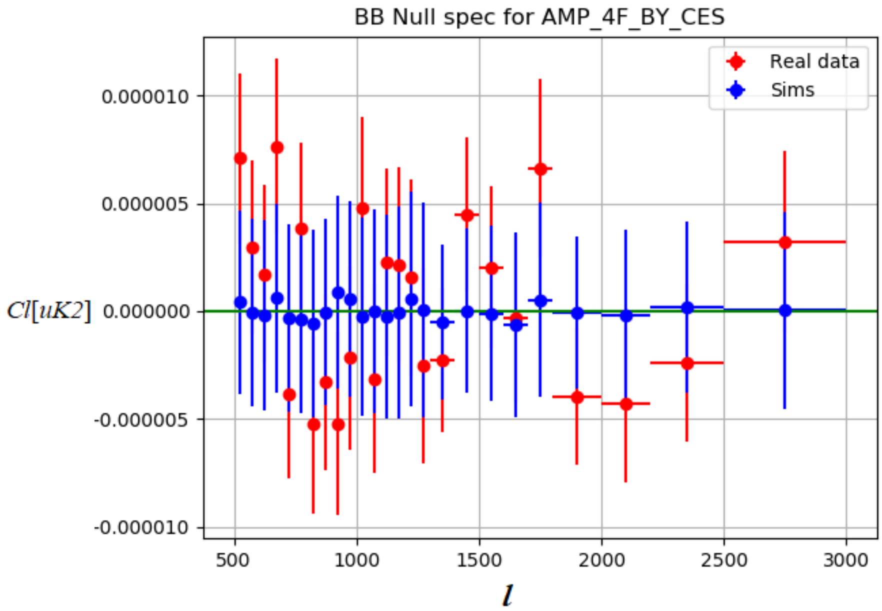

FIGURE 6.7: Up: Null spectra for EE for the test "$4f$ amplitude by CES". Down: Null spectra for BB for the same test. In both plots, 'Real data' means the null spectrum is from POLARBEAR selected data, and 'Sims' means the average of null spectra from 48 simulated maps. Unlike the power spectra presented in other sections (e.g 6.2.4), the spectra are shown as C_ℓ, not $D_\ell \equiv \ell(\ell+1)C_\ell/(2\pi)$, in order to see that the error bars should be uniform across all bins like in a white noise spectrum. The error bars for all bins are similar for both real data and simulated data. The error bars for EE and BB are approximately equal, which shows good estimation and cancellation of the signal for each half of the data because polarisation noise is expected to be the approximately same for EE and BB.

The null spectra, similar as in the example, are consistent with zero, although a few consecutive bins in real data are negative or positive, which is because of the coupling between bins. This phenomenon is also seen in some null spectra from some individual simulated maps, which means this is a not problem in real data. Note that a problematic null spectrum contains the majority of bins staying either on the negative of positive side. This was seen in early trials of null tests, but is not present in this iteration.

TABLE 6.2: Null test PTE values

	Total EE χ^2 PTE
Null test summed over ℓ bins	
First half versus second half	90.1 %
Middle versus rising and setting	88.0 %
Left-going versus right-going subscans	39.5 %
High gain versus low gain CESs	58.0 %
High PWV versus low PWV	43.6 %
Mean temperature leakage by bolometer	11.4 %
Mean temperature leakage by CES	84.5 %
$2f$ amplitude by bolometer	71.7 %
$4f$ amplitude by bolometer	9.2 %
$2f$ amplitude by CES	47.5 %
$4f$ amplitude by CES	24.4 %
Q versus U pixels	89.4 %
Low or high distance from Sun	96.7 %
Sun above or below the horizon	65.8 %
Moon above or below the horizon	82.1 %
Top half versus bottom half	69.9 %
Left half versus right half	88.8 %
Top versus bottom bolometers	96.9 %
Random splits of bolometers	24.8 %
ℓ bin summed over null tests	
$500 \leq \ell < 550$	34.7 %
$550 \leq \ell < 600$	8.9 %
$600 \leq \ell < 650$	96.8 %
$650 \leq \ell < 700$	52.2 %
$700 \leq \ell < 750$	90.9 %
$750 \leq \ell < 800$	47.1 %
$800 \leq \ell < 850$	82.3 %
$850 \leq \ell < 900$	96.8 %
$900 \leq \ell < 950$	39.2 %
$950 \leq \ell < 1000$	25.8 %
$1000 \leq \ell < 1050$	90.1 %
$1050 \leq \ell < 1100$	44.8 %
$1100 \leq \ell < 1150$	79.6 %
$1150 \leq \ell < 1200$	52.5 %
$1200 \leq \ell < 1250$	69.3 %
$1250 \leq \ell < 1300$	72.0 %
$1300 \leq \ell < 1400$	95.4 %
$1400 \leq \ell < 1500$	2.3 %
$1500 \leq \ell < 1600$	96.5 %
$1600 \leq \ell < 1700$	18.8 %
$1700 \leq \ell < 1800$	48.5 %
$1800 \leq \ell < 2000$	47.6 %
$2000 \leq \ell < 2200$	87.0 %
$2200 \leq \ell < 2500$	66.9 %
$2500 \leq \ell < 3000$	80.2 %

Projected PTE values for the total χ^2 of each null spectrum summed over ℓ bins and each ℓ bin summed over null splits. We find that not projecting the χ_{null} from 48 MC to a large population or using a moderate subset of simulations does not cause any PTE to be overtly problematic. Overall, the PTEs indicate no significant problems.

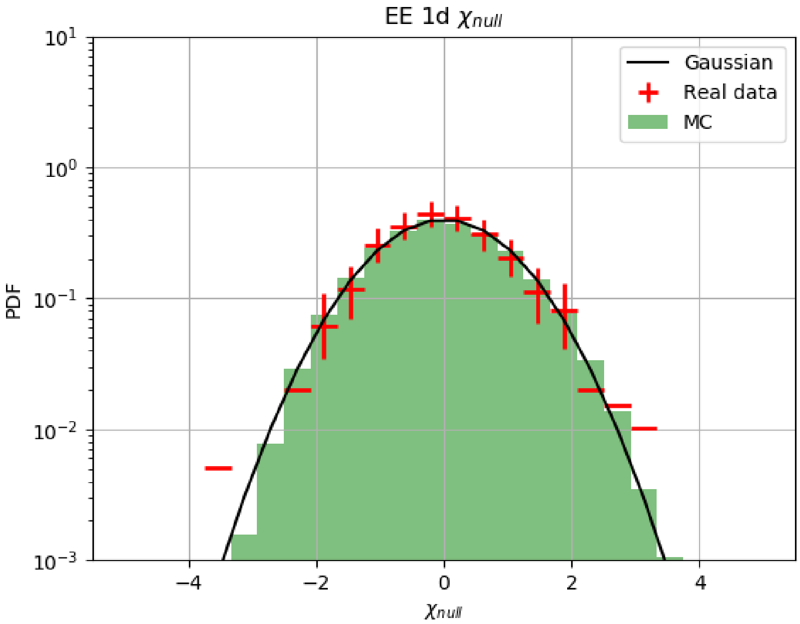

FIGURE 6.8: Black is the Gaussian distribution fitted from the MC χ values in green. Red is the χ values of real POLARBEARdata

are sufficient to spread over 99.8% of a normal distribution when the random generator used to generate simulated map RMS noise is bias-free. However, all returned PTEs are safely above this threshold as shown in Table 6.2, which indicates no significant problem.

In addition, we perform a KS test on the three sets of PTEs of the χ^2_{null} values by test, by bin, and overall to compare the distributions of the sets with a uniform distribution. The distribution of the returned PTEs in Table 6.3 are found to be consistent with uniformity. Finally, we require the total PTE χ^2_{null} overall to be at minimum 12% to have the overall false-positive rate of 5%. As defined in 6.3.1, the total PTE χ^2_{null} is the PTE computed from the number of projected total χ^2_{null} summed over all tests and bins. The achieved PTE is a positive number of 67.9% for EE case. For BB, the achieved PTE is 65%, which is consistent with EE and is expected when the estimation of signals in the null spectra is efficient and the polarisation noise is equal for both EE and BB spectra. Other quantities, whose names are clear in themselves, are not examined for our set of established set of criteria but also shown in Table 6.3. Over all, the null tests pass our criteria and imply that our real data are free from unknown unknowns.

6.4 Systematics

The final check on the data quality is to estimate the magnitude of known sources of systematic bias. This is done by simulating known systematic effects and estimating

TABLE 6.3: Null test PTE values

Null statistic	EE PTE
Average χ overall	94.7 %
Most extreme χ^2 by bin	44.1 %
Most extreme χ^2 by test	65.4 %
Most extreme χ^2 overall	29.2 %
Total χ^2 overall	67.9 %
KS test on all bins	44.9 %
KS test on all spectra	29.5 %
KS test overall	13.3 %

PTE values for each of the high level null test statistics pass out null test criteria, indicating that our real data are reliable for unblinding.

upper bounds of these effects in the simulated spectra. The estimation of systematics relies on both simulated map making pipeline and the power spectrum pipeline. We find upper bounds on the bias introduced by these effects to be subdominant to the statistical error in all spectra.

The systematic mapmaking pipeline is modified from the simulation pipeline used for the null tests and final real data outputs. The pipeline updates are done by Neil Goeckner-Wald and Satoru Takakura, while I run this pipeline to get the final systematic estimation for selected high-ℓ data. For most systematic sources, clean simulated TOD are first produced by mock-observation of a signal-only ΛCDM sky with POLARBEAR detector pointing configuration. How the simulated sky signals are passed into simulated TOD is earlier described in 5.3. Then, systematic effects are injected into these TOD case by case. The injected TOD are then processed with usual filtering and projection options shared with real data. The injected maps are divided into 12 bundles like for real data, then passed onto the power spectrum pipeline of which the mode mixing matrix and filter transfer function for most systematic cases are shared with real data powerspectra. Since systematics can be degenerate with deviated gain and polarisation angle, the spectrum of each case is calibrated with the theory spectrum, returning an absolute gain factor g for all bandpowers such that the Total Chisquared:

$$\chi^2_{Tot} = \sum_b \frac{(C_b^{theory} - g^2 C_b)^2}{(\sigma D_b)^2} \tag{6.7}$$

is minimised. Here, C_b^{theory} are the theory bandpowers which can be calculated similarly to 6.2.2, the theory is the same one noted in 5.5, C_b are the bandpowers from simulated maps, and σD_b are the bandpower errors calculated using 5.10. In this specific case, the signal part of σD_b is from the theory bandpowers, while the noise part is calculated from the simulated real signflip maps following the pipeline described in 5.5.

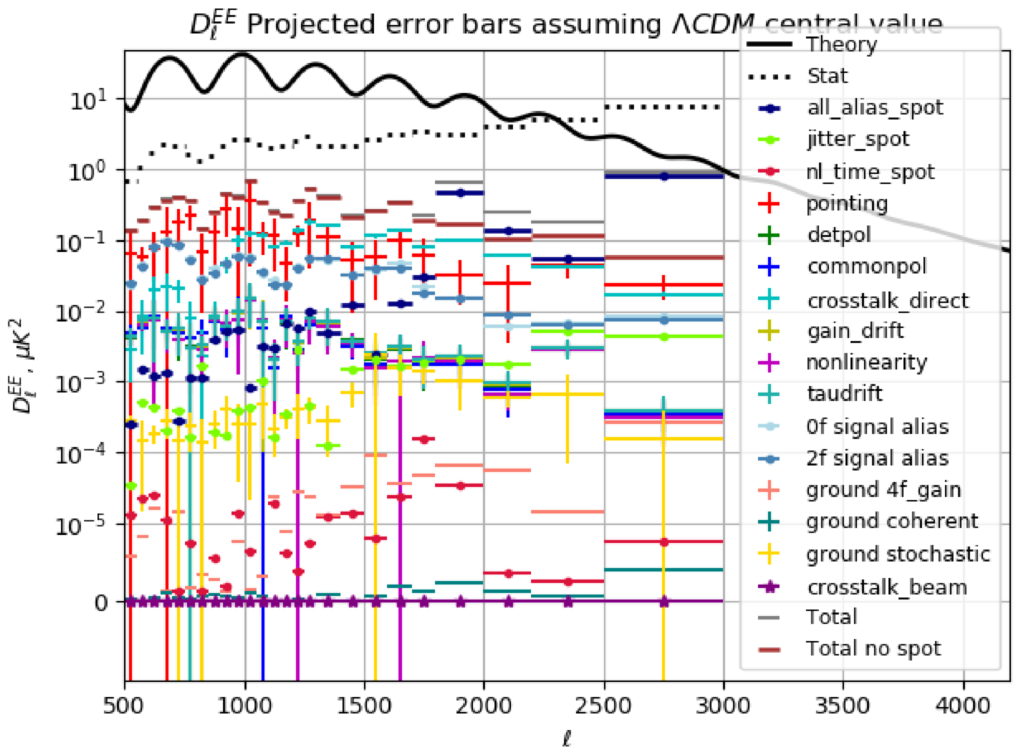

FIGURE 6.9: Estimates of systematic errors as well as the linearly combined total systematic error are shown. The total systematic error excluding the errors due to the HWP spot is also plotted to see the amplitude of this effect as compared with others. The statistical error is above all.

A set of simulated systematic-free maps are also created for reference spectra. The absolute difference between the distorted spectra and the reference spectra is defined as the systematic error. The cross spectrum framework in 5.5 typically gives a separation of noise and signal, which cannot be done with an autospectrum of a single map made from full data. However, this separation is not perfect as seen from the non-zero difference between the distorted spectra and the reference spectra.

The overall systematic error is taken to be the linear sum of errors from each systematic source. This is done basing on the assumption that the effects are largely uncorrelated with each other, which results in a upper limit for estimation. The total systematic error estimate as well as the contributions from groups of effects in EE are shown in Figure 6.9. The total systematic error is found to be sufficiently below the statistical error. Individual effects that contribute to this estimate are described as followed.

6.4.1 Gain miscalibration, time constant drift, detector non-linearity

Gain miscalibration, time constant drift, detector non-linearity are denoted as "gain drift", "taudrift", and "nonlinearity" respectively in Figure 6.9. Gain miscalibration is considered to have effects on the finite precision of detector relative gain calibration. This effect is thus done by varying the gain calibration factor for each detector in each observation with errors following a normal distribution around the average fractional error that is estimated following Chapter 4 and found to be 4.7%. Thus, a sample at time t of a detector (demodulated) timestream d is miscalibrated to be:

$$d(t) \times g(t) \times (1 + e(t))$$

where $e(t)$ is the fractional error at time t with the mean value of 4.7%.

Detector non-linearity is seen to cause mainly the additive temperature to polarisation leakage following Chapter 3. However, this increased polarisation supposedly causes gain variation which is a multiplicative term acting on signal. Hence, the detector small signal gain (time constant τ) is traced with downsampled normalised TOD amplitude at 4 times of HWP frequency ($4f$). The non-linear behavior is taken as the time dependent polarisation angle error injected into the simulated clean timestreams. Detector non-linearity effect is simulated by shifting the timestamps of the samples in TOD with detector time constants to cause the change in gain values at each time instant. Time constant drifting "taudrift" effect is simulated by re-modulating the TOD with the function $e^{2i\theta_{det}}$ then demodulating with $e^{-2i\theta_{det}+err}$ where err is a small phase error caused by time constant and roughly estimated by $\tau \times 4\pi$ due to τ being very small in the used unit (second).

6.4.2 Polarisation angle error

Detector polarisation angle miscalibration is modeled by varying the calibrated detector polarisation angle errors around the true values following a Gaussian distribution of standard deviation $1.^\circ 2$. This standard deviation is taken from the distribution of the pair angles between two detectors of the same pair, where pair angle means the difference angle between two detectors. The impact of an overall polarisation angle miscalibration is estimated by changing the polarisation angle of the input sky by $0.^\circ 5$ RMS. This number is the Tau A polarisation angle uncertainty quoted in [13]. The residual between the calibrated spectrum for overall polarisation angle miscalibration and the reference spectrum is non-zero even after absolute polarisation angle calibration following [101]. The reason is different Q and U common mode filtering in map making operation changes under polarisation angle rotation. The impact from detector polarisation angle miscalibration is minimal after the absolute polarisation angle calibration. Detector polarisation angle miscalibration and overall polarisation angle error are denoted as "detpol" and "commonpol" respectively.

6.4.3 Boresight pointing error

As given in 4.3, the pointing error is 18". The boresight pointing systematic effect is estimated by using alternative pointing models in mapmaking operation to create another set of mock-observation maps. This is justified by the fact that incomplete understanding of the boresight pointing leads to inclusions or exclusions of parameters or Jupiter data in constructing candidate models. This uncertainty in the choice of models directly leads to pointing errors. This is the largest systematic error in our E-mode spectrum for $\ell < 2000$ because the signal still surpasses the noise in this range for POLARBEAR data and the variance in pointing results in the variance in calculations of mode size. However, this effect is safely under our statistical errors over our multipole range.

6.4.4 Crosstalk

Crosstalk systematic is defined to be originated from electrical couplings between detectors readout connected to the same cables. This crosstalk is assumed to be linear and the same for the whole dataset i.e a constant crosstalk impact is applied the same way in each CES. The effect of crosstalk is estimated using Jupiter data taken for calibration in Chapter 4. Because Jupiter is mapped as point source with POLARBEAR beam width, maps of Jupiter show beam shape in the center. Crosstalk would produce visible negative copies of the beam shape around the main beam. Since crosstalk is due to detector readout coupling, a matrix can be established to represent the coupling of signals in detectors i and j using the amplitudes of the images,

$$d_{j,\text{observed}} = d_{j,\text{real}} + \sum_{i \neq j} \mathbf{L}_{ij} d_{i,\text{real}}. \tag{6.8}$$

Elements of $\mathbf{L}$ are fitted to individual Jupiter detector maps for detectors on the same cables. Non-zero off-diagonal elements of $\mathbf{L}$ are found to be around $\sim 1\%$, and the median row sum is approximately 4%. Equation 6.8 shows the constant crosstalk can be injected directly into the demodulated polarisation TOD in simulations. This effect is found to be already sufficiently below our statistical error without using the crosstalk matrix to suppress this effect as done in [6]. The crosstalk effect via beam calibration is estimated by using crosstalk-injected maps to derive the change in the beam profile, which supposedly impacts the correction of the power spectra. Overall, this effect is found to be insignificant.

6.4.5 Ground Pickup

Ground pickup systematics are taken as the ground-fixed structure observed in the TOD. The ground structure likely originates from far sidelobes seeing the surrounding terrain. The amplitude of this structure is at the level of 100 μK after subscan polynomial filtering. The effect is mainly removed by subtracting TOD binned in azimuth for each detector per CES. This effect is denoted by 'ground coherent' in Figure 6.9.

Ground pickup can be coupled with detector non-linearity which introduces the detector small signal gain. This non-linearity results in imperfect ground fixed structure subtraction. The ground template for subtraction can drift over the course of a CES. This is modeled for each CES type (rising, middle, and setting). For each detector, the polarisation TOD for each subscan is fitted to tenth order Legendre polynomial series. These coefficients resulting from fitting are averaged across all CESs to make the ground synchronous structure polarisation templates. This effect is denoted by 'ground 4fgain' in Figure 6.9.

The drift of the ground fixed signal amplitude within a CES is expected to be uncorrelated with solar or sidereal time. This is modeled on the assumption that the apparent ground fixed signal temperature drift causes the variance in the ground amplitude slope. This effect is found to cause noise mainly in low-ℓ range in the map domain and is denoted by 'ground stochastic' in Figure 6.9.

The overall contamination from ground pickup is also validated to be insignificant via the passing of relevant null tests concerning CES types (rising, middle, setting)and half focal plane splits.

6.4.6 HWP Signal Aliasing

We group the total leakage from intensity to polarisation due to optical elements into HWP signal aliasing. As in 3.3, HWP signal aliasing causes an increase in the variance in the polarisation data via aliasing of the temperature signal into polarisation band centered at the HWP $4f$ and leakage of the temperature signal into the sidebands of the HWP $2f$, which can then be aliased into the polarisation timestreams. Both cases are unavoidable because separation of temperature and polarisation is imperfect despite the leakage subtraction done in 5.3. The impact of this effect is estimated by injecting the temperature TOD at the 0.6% level to the $2f$ and the $0f$ components of the polarisation TOD. The number 0.6% is chosen basing on the leakage summarised in 3.4 and consists of the leakage due to non-linearity and twice the leakage from optical elements to round up the effects due to HWP transmission. The TOD are not filtered but simply projected into maps. Pseudo spectra produced from these maps are thus not corrected with a filter transfer function. We see a coupling between the aliased component and the polarisation signal scanned from simulated skies containing both intensity and polarisation. The estimate for this systematic thus varies with the amplitude of the polarisation power spectra and is assumed to be the conservative upper limit for this effect. Overall, this systematic error appears to be negligible compared to our statistical errors for both E and B-mode channels.

6.4.7 HWP Imperfections

As described in 3.3.3, the HWP contains a small imperfection from a small air bubble in the anti-reflection coating on the rotating HWP. Estimation of the HWP spot amplitudes is done by fitting the left-over TOD post HWPSS subtraction and I, Q, U separation to the $0f$,$2f$, and $4f$ modes of Equation 3.17. The HWP spot is found to have synchronous structure stable with time. Like the HWPSS, the HWP spot structure can be subtracted. Thus, the aliased power from the HWP spot is estimated by convolving of the total of harmonics appearing at different numbers of the HWP frequency with other effects that change the multiplicative factors on the timestream like in 6.4.1: non-linearity, time constant drift, and gain error. The aliased power is added directly to the simulated TOD. The terms related to the HWP imperfections are denoted with the suffix "spot" in Figure 6.9. The total error due to HWP spot is found to be sufficiently below our statistical error. The figure also shows the term 'Total no spot', which means the sum of all systematic biases excluding the ones caused by the spot to show that the HWP spot contributes most to errors in the upper multipoles.

Chapter 7

Results

Having validate the selected data and the processing pipeline, we want to unblind the E-mode power spectrum measured from POLARBEAR data. This chapter closely follows *Pham et al 2020*, an already submitted POLARBEAR paper. I will present the POLARBEAR bandpowers, and then present the cosmological model constraints from POLARBEAR bandpowers together with other datasets. A brief overview of the parameters will be given prior to the results of constraints.

7.1 Bandpowers

The debiased E-mode spectrum of POLARBEAR is first calibrated with the theory spectrum similarly to the work for the simulated spectra in 6.4 using POLARBEAR's debiased bandpowers and debiased noise bandpowers. Absolute gain calibration can also be done as demonstrated in [87]. The first way results in $g = 1.1$, which is close to $g = 1.08$ in [87].

The calibrated E-mode bandpowers measured by applying the analysis method of Section 5.5 to the POLARBEAR 670 deg^2 survey are shown in Figure 7.1 and tabulated in Table 7.1. The full data were divided into 12 bundles before calculation of cross spectra. Note that without the cross spectrum framework, all bandpowers would contain error bars and thus exceed at high-ℓ bins e.g $2500 < \ell < 3000$. The figure shows that errors might not be entirely separated from signals however. E-mode power is detected at very high significance, with zero E-mode power excluded at 61σ. This uncertainty is taken as the inverse of the significance of the detection, which is $\sim 2\%$. The POLARBEAR bandpowers trace out the third through seventh acoustic peaks in the E-mode spectrum, and extend to $\ell = 3000$ well into the Silk damping tail.

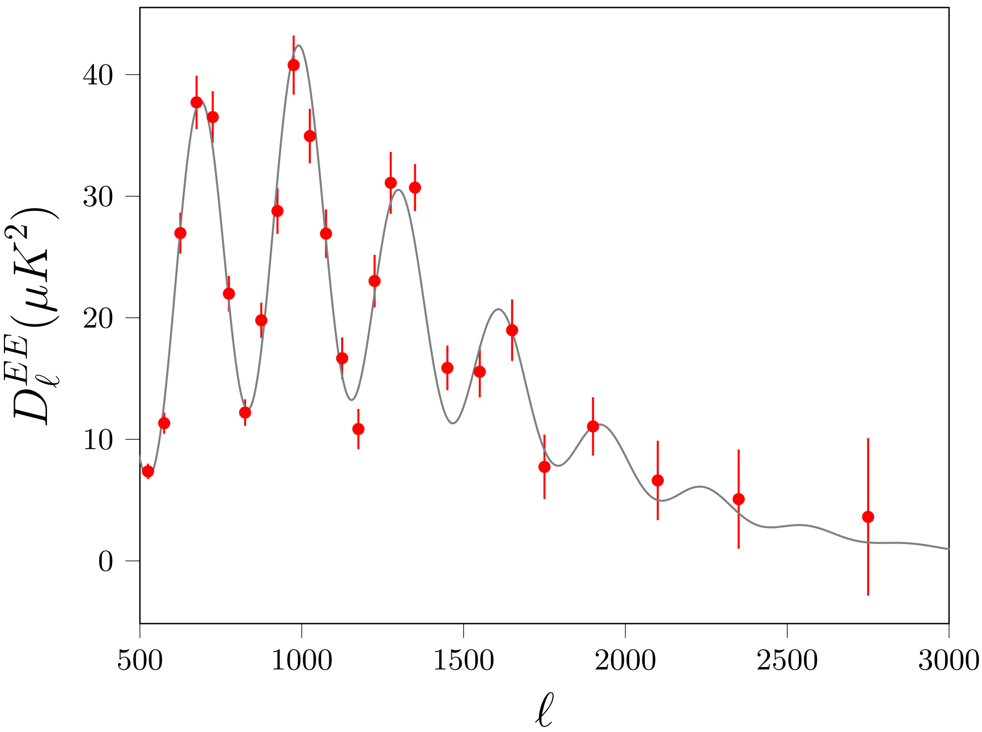

FIGURE 7.1: Measured POLARBEAR E-mode spectrum with included error bars from statistical uncertainties. The grayish line is the best fit *Planck* 2015 ΛCDM in [14]. The numerical values of bandpowers and statistical errors are shown in Table 7.1. POLARBEAR bandpowers are overall consistent with the ΛCDM model.

We show the current state of E-mode power spectrum measurements in Figure 7.2. In this figure, we compile the bandpowers of this work with other recent E-mode measurements [16, 15, 17, 6]. The observed E-mode spectra agree well between experiments, enhancing our confidence in the E-mode measurements.

7.2 Cosmological implications

I now turn to the cosmological implications of the POLARBEAR E-mode power spectrum along with other recent cosmological observations. First, I will look at parameter constraints for the standard, six-parameter, ΛCDM cosmological model. Then, I also look at three one-parameter extensions to ΛCDM, $N_{\rm eff}$, $Y_{\rm He}$, or $n_{\rm run}$, chosen because the extension influences the damping tail. Finally, I consider the two-parameter extension of $Y_{\rm He}$+$N_{\rm eff}$, of interest as a test of Big Bang nucleosynthesis (BBN). Now I will describe the methodology to constrain these parameters with selected datasets.

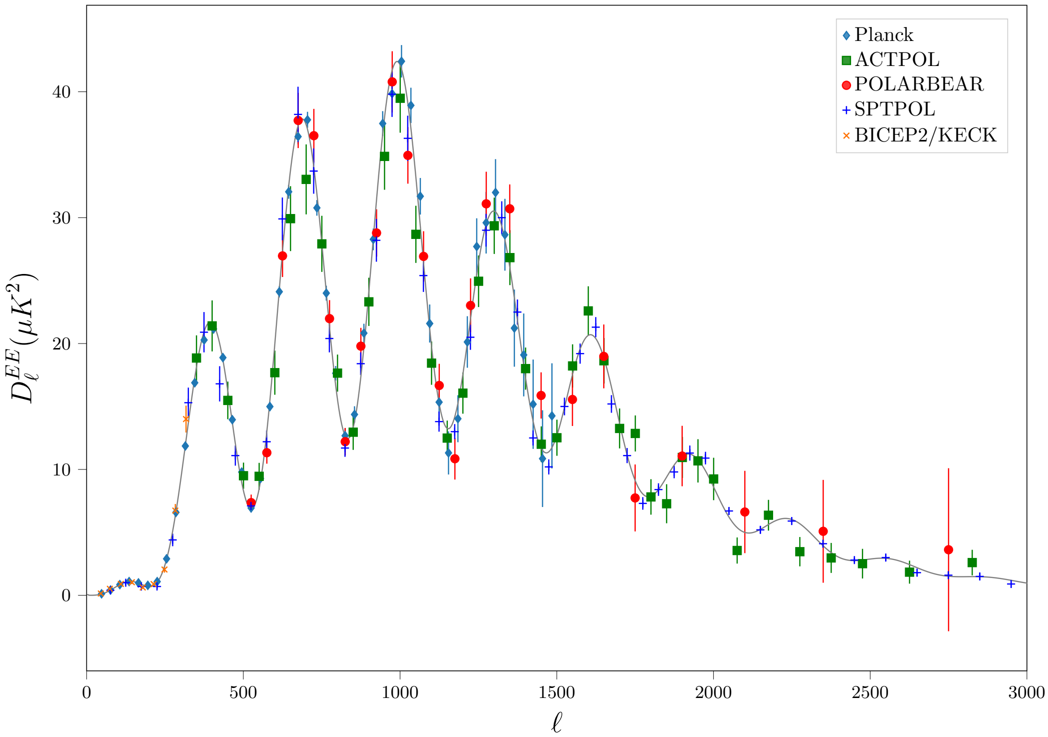

FIGURE 7.2: Recent CMB E-mode power spectrum measurements from *Planck* [15], POLARBEAR, SPTPOL [6], ACTPOL [16], and BICEP2/Keck [17] have mapped out the E-mode power spectrum at high S/N from very large scales out to the ninth acoustic peak. The power spectrum measurements from the different experiments are in good agreement with each other. The data used in the parameter section of this work are shown by filled points.

7.2.1 Methodology

I derive parameter constraints using the 2019 version of the Markov Chain Monte Carlo (MCMC) package COSMOMC [109]. The COSMOMC has been extended to include the POLARBEAR bandpowers in a manner similar to the public likelihood for [6]. The POLARBEAR likelihood code and data are available on the LAMBDA website.[1]

In addition to the normal cosmological parameters in COSMOMC, I have added five nuisance parameters specific to the POLARBEAR data, most with an informative prior. The first parameter is the calibration factor (in power) for the POLARBEAR E-mode power spectrum. A prior on this factor has been set based on the expected 2% uncertainty in the absolute calibration (see Section 7.1). The other four parameters relate to on-sky signals. First, one term serves to describe the polarized Poisson-distributed point source power in the field after masking. This power scales with ℓ as $D_\ell \propto \ell^2$, and the reported power is at $\ell = 3000$, D_{3000}^{PS}. I use a non-informative prior on the point source power that is uniform for $D_{3000}^{PS} \in [0, 10]\,\mu\mathrm{K}^2$. The upper limit $10\mu\mathrm{K}^2$ is just chosen to be high

[1] https://lambda.gsfc.nasa.gov/product/polarbear/

TABLE 7.1: Bandpowers

Multipole range	ℓ_{eff}	D_b^{EE} [μK^2]	$\sigma(D_b^{EE})$ [μK^2]
$500 \leq \ell < 550$	525.4	7.36	0.64
$550 \leq \ell < 600$	575.3	11.33	0.87
$600 \leq \ell < 650$	625.3	26.96	1.68
$650 \leq \ell < 700$	675.2	37.72	2.19
$700 \leq \ell < 750$	725.4	36.51	2.13
$750 \leq \ell < 800$	775.2	21.98	1.46
$800 \leq \ell < 850$	825.3	12.20	1.09
$850 \leq \ell < 900$	875.2	19.79	1.45
$900 \leq \ell < 950$	925.3	28.79	1.87
$950 \leq \ell < 1000$	975.2	40.78	2.43
$1000 \leq \ell < 1050$	1025.3	34.95	2.25
$1050 \leq \ell < 1100$	1075.2	26.92	2.0
$1100 \leq \ell < 1150$	1125.2	16.67	1.72
$1150 \leq \ell < 1200$	1175.1	10.89	1.65
$1200 \leq \ell < 1250$	1225.2	23.02	2.16
$1250 \leq \ell < 1300$	1275.1	31.09	2.55
$1300 \leq \ell < 1400$	1350.6	30.71	1.93
$1400 \leq \ell < 1500$	1450.6	15.88	1.84
$1500 \leq \ell < 1600$	1550.6	15.56	2.11
$1600 \leq \ell < 1700$	1650.5	18.98	2.54
$1700 \leq \ell < 1800$	1750.5	7.74	2.65
$1800 \leq \ell < 2000$	1901.8	11.06	2.40
$2000 \leq \ell < 2200$	2101.6	6.62	3.27
$2200 \leq \ell < 2500$	2353.2	5.08	4.08
$2500 \leq \ell < 3000$	2757.6	3.621	6.47

The angular multipole range, E-mode bandpowers, and uncertainties for the POLARBEAR survey. The uncertainties are taken from the square root of the diagonal of the covariance matrix, and do not include beam or calibration errors.

enough so that it does not cut off the data posterior. Second, two parameters are used to describe polarized Galactic dust, which is modeled as having a power spectrum,

$$D_\ell^{\text{dust}} = D_{80}^{\text{dust}} \left(\frac{\ell}{80}\right)^{\alpha}_{\text{dust}}. \tag{7.1}$$

Given that the POLARBEAR bandpowers are at angular multipoles much much higher than $\ell = 80$, which is the reference multipole in 7.1, I fix $\alpha_{\text{dust}} = -0.58$ and apply a strong Gaussian prior of $D_{80}^{\text{dust}} \in N(0.0094, 0.0021^2)\,\mu\text{K}^2$ on the amplitude. These values are taken from [17]. Finally, I allow for "super-sample lensing" variance [110]. This is parametrised by a the mean lensing convergence across the field, κ, to which I apply a Gaussian prior centered at zero with a $1\,\sigma$ width of 0.001[111].

7.2.2 Data sets

I include the *Planck* 2018 TT, TE, and EE power spectra likelihoods in all results [15]. Constraints from *Planck* alone are referred to by '*Planck*'. I also explore the effects of adding ground-based CMB measurements, specifically the SPT-SZ TT measurements [112], ACTpol TT/TE/EE measurements [16], and the POLARBEAR EE spectrum in this work. BICEP2/Keck array data at large angular scales are not included because this analysis does not aim at the tensor-to-scalar ratio. The SPTpol TE/EE measurement [6] is also excluded because it has nearly 100% sky overlap with the POLARBEAR survey. Accounting for the common sample variance would be a non-trivial exercise and is not possible using only the publicly available likelihood. Given the clear agreement between the different E-mode measurements in Figure 7.2, I am confident that it is appropriate to combine these different datasets. Constraints from the combination of *Planck* 2018 and the ground-based CMB measurements are referred to by 'CMBall' in the tables and 'All CMB' in the figures.

As noted in 1.5, the small degeneracy between the spectral index and the optical depth in the temperature power spectrum can be resolved with information from the low-ℓ range of the polarisation spectrum. This range is however not available from additional CMB datasets included in this analysis except *Planck* 2018.

What impact data besides the CMB power spectra have on the cosmological constraints is also a point of consideration. Here this analysis includes the lensing power spectra from *Planck* and SPTpol [113, 114]. The [115] local measurement of the Hubble constant, $H_0 = 74.03 \pm 1.42\,\mathrm{km/s/Mpc}$, is also included. Lastly, I include three baryon acoustic oscillation measurements: the SDSS-III BOSS DR12 Consensus sample [116], the DR7 MGS sample [117] and the 6dFGS survey [118]. The constraints that include these data in addition to the CMB power spectrum data are labeled 'CMBext'.

7.2.3 Constraints on the ΛCDM model

As has been previously noted, the *Planck* 2018 CMB power spectrum data alone do an excellent job of constraining all six parameters in the standard ΛCDM model. We report the median parameter values and 68% confidence intervals in Table 7.2. While the optical depth is relatively uncertain with a 14% error bar, the other five parameters are measured with percent-level precision. Adding the ground-based CMB power spectrum measurements to the mix reduces the allowed parameter volume by a factor of 2.0, or roughly a 7% reduction in parameter uncertainties. These small-scale power spectrum measurements do not help recover the optical depth however, as that measurements

TABLE 7.2: ΛCDM parameter constraints

	Planck	CMBall	CMBext
$\boldsymbol{\Omega_b h^2}$	0.02237 ± 0.00015	0.02229 ± 0.00014	0.02232 ± 0.00014
$\boldsymbol{\Omega_c h^2}$	0.1200 ± 0.0014	0.1203 ± 0.0013	0.1199 ± 0.0011
$\boldsymbol{100\theta_{MC}}$	1.04089 ± 0.00032	1.04102 ± 0.00029	1.04100 ± 0.00029
$\boldsymbol{\tau}$	0.0548 ± 0.0079	0.0524 ± 0.0079	0.0522 ± 0.0067
$\boldsymbol{\ln(10^{10} A_s)}$	3.044 ± 0.016	3.042 ± 0.016	3.040 ± 0.014
$\boldsymbol{n_s}$	0.9650 ± 0.0045	0.9643 ± 0.0038	0.9645 ± 0.0039
$\boldsymbol{H_0}$ (km s^{-1} Mpc^{-1})	67.42 ± 0.69	67.21 ± 0.57	67.39 ± 0.49

The median values and 68% confidence intervals for the six ΛCDM parameters for the *Planck*, CMBall and CMBext datasets. Adding the ground-based CMB power spectrum measurements to *Planck* reduces the parameter uncertainties by ∼7% (except for the amplitude terms A_s and τ which depend on the low$-\ell$ polarization bump). Adding the BAO, H_0 and CMB lensing data further reduces uncertainties by an additional ∼10%.

depends on the reionisation bump at $\ell < 10$. Adding the CMB lensing, BAO and H_0 data yields an across the board further reduction in uncertainties of order 10%. Notably, lensing provides another avenue to measure the amplitude of fluctuations, A_s, which partially breaks the $A_s e^{-2\tau}$ degeneracy in the power spectrum alone and helps the determination of A_s and τ. Both 2 datasets CMBall and CMBext see a decrease in τ compared to *Planck*. This suggests that additional information from other CMB experiments and BAO improves the constraint of τ that may have been limited by the galactic dust template for *Planck*.

There has been much discussion recently about the degree of tension between local determinations of the Hubble constant, H_0, and the values inferred from the *Planck* data [119]. Adding the ground-based CMB bandpowers to the *Planck* data supports the current tension on the Hubble constant by reducing the uncertainty by a factor of 1.2 to:

$$H_0 = 67.21 \pm 0.57 \text{ km s}^{-1}\,\text{Mpc}^{-1}. \tag{7.2}$$

The tension with the local determination by [115] of $H_0 = 74.03 \pm 1.42$ km s^{-1} Mpc^{-1} remains essentially unchanged from 4.3 to 4.5 σ.

7.2.4 Constraints on running of the scalar spectral index

The shape of the power spectrum of the primordial scalar anisotropies is an important clue to the origins of the Universe. In the slow-roll inflation models, the departure from scale invariance, $1 - n_s \simeq 0.04$, is first order in the slow-roll parameters, while running of the scalar spectral index, $dn_s/dlnk$ is second order and thus smaller [3]. In this model, we consider the running of the spectral index in addition to the original 6

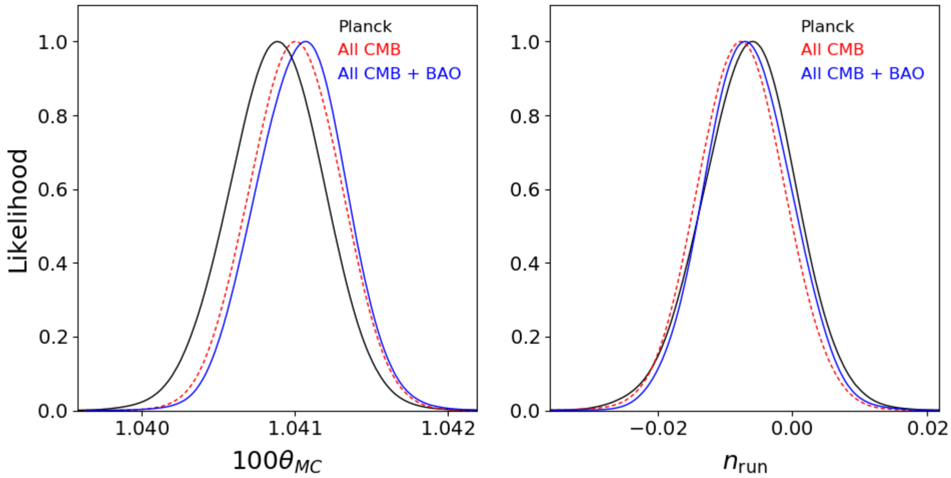

FIGURE 7.3: ΛCDM+$n_{\rm run}$ model parameter constraints for the primordial amplitude A_s and the running of the spectral index $n_{\rm run}$. The amplitude A_s is increased less than 0.5σ with additional datasets. The values of $n_{\rm run}$ are consistent in all cases, although the All CMB case sees a slightly smaller value for this parameter.

TABLE 7.3: Parameter constraints for ΛCDM + $n_{\rm run}$

	Planck	CMBall	CMBext
$\boldsymbol{\Omega_b h^2}$	0.02240 ± 0.00015	0.02235 ± 0.00015	0.02236 ± 0.00013
$\boldsymbol{\Omega_c h^2}$	0.1202 ± 0.0014	0.1205 ± 0.0013	0.1200 ± 0.0011
$\boldsymbol{100\theta_{MC}}$	1.04088 ± 0.00031	1.04100 ± 0.00029	1.04103 ± 0.00029
$\boldsymbol{\tau}$	$0.0564^{+0.0077}_{-0.0085}$	$0.0538^{+0.0075}_{-0.0084}$	0.0524 ± 0.0077
$\boldsymbol{\ln(10^{10} A_s)}$	3.050 ± 0.018	$3.048^{+0.015}_{-0.017}$	3.043 ± 0.015
$\boldsymbol{n_s}$	0.9635 ± 0.0046	0.9624 ± 0.0041	0.9634 ± 0.0040
$\boldsymbol{n_{\rm run}}$	-0.0064 ± 0.0070	-0.0076 ± 0.0065	-0.0065 ± 0.0064

Values of 7 parameters with 68% limits from the constraint of the extended ΛCDM with 3 combinations of datasets.

parameters. For all combinations of data, the baryon density, dark matter density and the angular size of the sound horizon are consistent with values from fitting the ΛCDM model. The constraints of the standard ΛCDM model extended with the running of the spectral index using 3 combinations of data are presented in Table 7.3. The probability distribution of $n_{\rm run}$ are shown in Figure 7.3.

Subsequently adding all other CMB datasets and BAO data slightly decreases both the primordial amplitude A_s and the optical depth τ by around 0.5σ. Like in the constraint for ΛCDM, the optical depth central values decrease in CMBall and CMB ext compared to *Planck*. *Planck* 2018 and CMBext (all CMB plus BAO) datasets result in the same central value for the spectral index n_s while the all-CMB dataset sees a small decrease for this parameter. This is directly related to the running of n_s from the all-CMB dataset going more negative as compared to the *Planck* 2018 and CMBext. The more

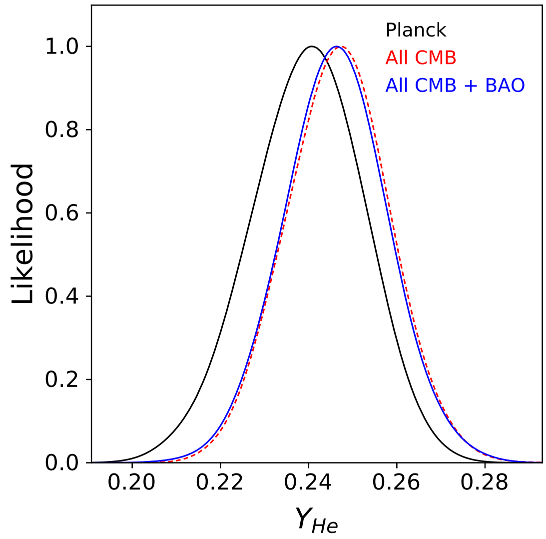

FIGURE 7.4: Posterior for the primordial helium abundance, Y_{He}, for the three datasets. Adding the ground-based CMB data to *Planck* slightly shifts the preferred helium abundance towards the BBN prediction of $Y_{\mathrm{He}} \sim 0.2467$, but leads to only a minor reduction in the uncertainty. All three datasets are in good agreement with the BBN prediction.

negative running of the spectral index could mean the small scales in the damping tail measurements from POLARBEAR, ACTPOL and SPTPOL are slightly over-estimated, at least compared to *Planck* 2018. Overall, this result is consistent with models that do not imply the running of n_s such as the standard ΛCDM and does not favor any models with large n_{run}. Inflationary models with large n_{run} can be found in [60].

7.2.5 Constraints on the primordial helium abundance

We also look at the inferred primordial helium fraction, which can be viewed as a test for new particles or physics during the epoch of big bang nucleosynthesis (BBN). The expected helium fraction under BBN consistency in the ΛCDM model for the CMBall dataset is extremely tightly constrained at $Y_{\mathrm{He}} = 0.246695 \pm 0.000057$. BBN predicts elemental abundances as a function of expansion rates during the right temperatures in the early universe. BBN consistency in COSMOMC sets the Helium abundance to that prediction from some nuclear modelling that some groups do (see e.g [120, 121]). Relaxing BBN consistency substantially weakens what we can infer about the helium fraction. However, the CMB anisotropies have some sensitivity to the helium fraction as it changes the number of free electrons at recombination. Higher helium fractions lead to fewer free electrons, a longer photon mean free path and thus more Silk damping. Using *Planck* alone, we find $Y_{\mathrm{He}} = 0.239 \pm 0.013$. Adding the other CMB measurements improves this slightly to

$$Y_{\mathrm{He}} \;=\; 0.246 \pm 0.012, \tag{7.3}$$

in excellent agreement with the expectation from BBN. There is no further improvement from adding the other cosmological data.

7.2.6 Constraints on the number of relativistic species

The energy density of relativistic particles in the early Universe is proportional to N_{eff}, the effective number of relativistic species. The standard model of particle physics predicts that $N_{\mathrm{eff}} = 3.046$ for the three neutrino species plus a small correction from positron annihilation. The preferred N_{eff} from the CMBall dataset is within $0.4\,\sigma$ of this prediction:

$$N_{\mathrm{eff}} = 2.97 \pm 0.20.$$

Adding the non-CMB data (i.e. the CMBext dataset) slightly reduces the preferred value of N_{eff}, but it remains within $0.9\,\sigma$ of the expectation:

$$N_{\mathrm{eff}} = 2.90 \pm 0.17.$$

When N_{eff} is allowed to vary, as shown in Figure 7.5 we see that it correlates strongly with $\Omega_c h^2$ and n_s. As discussed by [50], increasing the matter density as N_{eff} increases avoids shifting the redshift of matter-radiation equality. The central value of the optical depth is visibly decreased with each additional dataset as shown in Table 7.4. Decreased optical depth means that the scales below the horizon are less damped, which means that the amplitudes of acoustic peaks in the damping tail should be larger. This is consistent with a slightly decreasing N_{eff} because smaller N_{eff} means a sparser neutrino component which has a reduced gravitational effect on traveling photons. The optical depth does not see any substantial degeneracy with N_{eff} in the constraint however. Like for the constraint for ΛCDM, the decrease in the optical depth should also be due to more information from CMB data besides *Planck*. A side effect is that the CMB constraint on the Hubble constant significantly weakens: the uncertainty on the Hubble constant nearly triples from ± 0.57 to ± 1.5 km s^{-1} Mpc^{-1} (the central value changes by less than $0.4\,\sigma$).

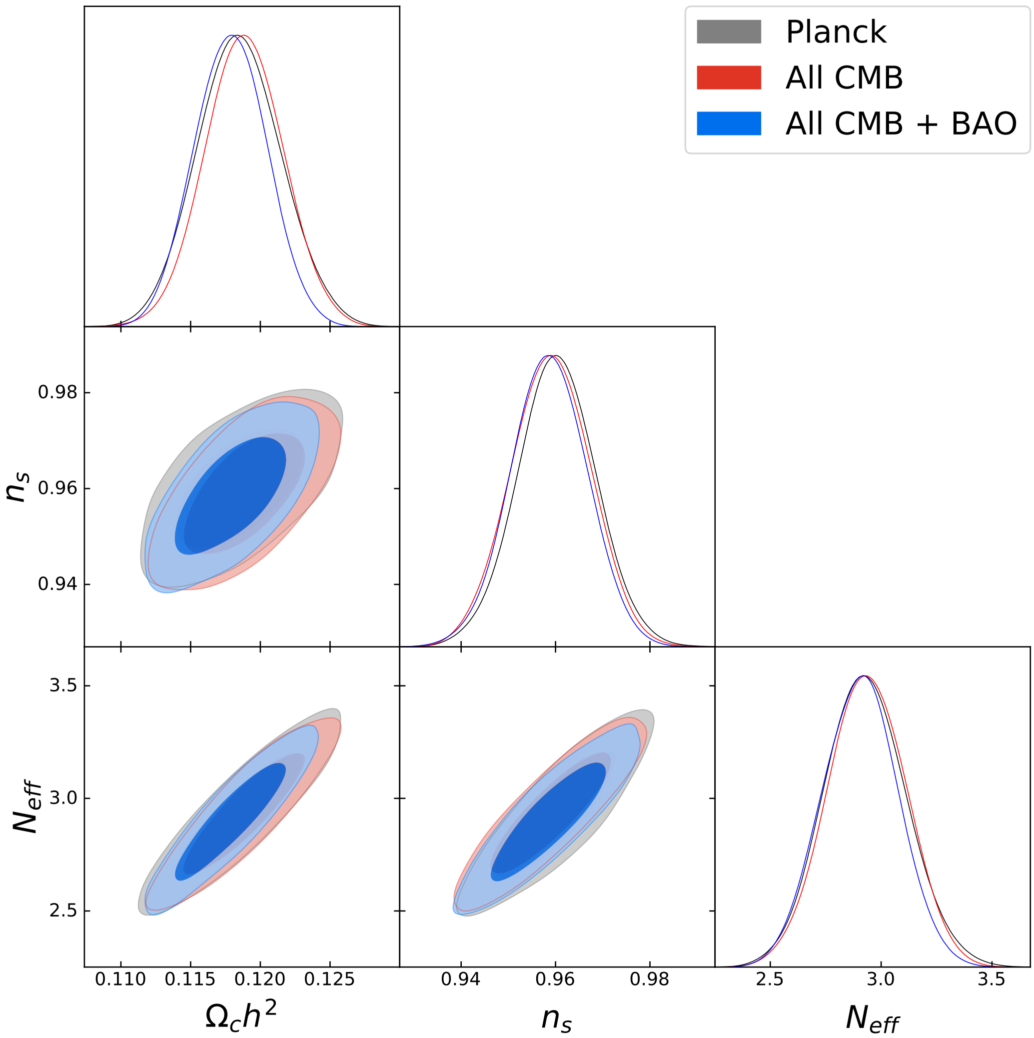

FIGURE 7.5: Posteriors for the $N_{\rm eff}$, n_s, and $\Omega_c h^2$ parameters for the *Planck*, CMBall, and CMBext datasets. Adding data beyond the *Planck* CMB bandpowers only modestly reduces the allowed parameter volume without significantly shifting the preferred values or breaking the parameter degeneracies.

TABLE 7.4: Parameter constraints for ΛCDM $+N_{Eff}$

	Planck	CMBall	CMBext
$\boldsymbol{\Omega_b h^2}$	0.02226 ± 0.00022	0.02218 ± 0.00021	0.02220 ± 0.00021
$\boldsymbol{\Omega_c h^2}$	0.1185 ± 0.0030	0.1188 ± 0.0028	0.1181 ± 0.0025
$\boldsymbol{100\theta_{MC}}$	1.04109 ± 0.00045	1.04117 ± 0.00040	1.04122 ± 0.00040
$\boldsymbol{\tau}$	$0.0538^{+0.0071}_{-0.0082}$	0.0508 ± 0.0076	0.0509 ± 0.0069
$\boldsymbol{N_{eff}}$	2.93 ± 0.18	2.94 ± 0.18	2.90 ± 0.17
$\boldsymbol{\ln(10^{10} A_s)}$	$3.040^{+0.017}_{-0.019}$	3.036 ± 0.018	3.032 ± 0.017
$\boldsymbol{n_s}$	0.9603 ± 0.0083	0.9590 ± 0.0084	0.9587 ± 0.0081

Values of 6 parameters 68% limits from the constraint of ΛCDM $+N_{eff}$ with 3 combinations of datasets.

7.2.7 Constraints on the ΛCDM+Y_{He}+N_{eff} model

We now consider the results when allowing both N_{eff} and Y_{He} to vary, as both parameters affect the damping tail. As with the other extensions to ΛCDM considered, freeing these two parameters does not significantly improve the quality of the fit ($\Delta\chi^2 \simeq 1.2$ for two new parameters for the CMBext dataset). The resulting parameter posteriors are shown in Figure 7.6. We find for the CMBall dataset:

$$
\begin{aligned}
N_{\mathrm{eff}} &= 2.67 \pm 0.28, \\
Y_{\mathrm{He}} &= 0.262 \pm 0.016.
\end{aligned}
$$

The CMBext dataset prefers essentially the same values as well:

$$
\begin{aligned}
N_{\mathrm{eff}} &= 2.70 \pm 0.26, \\
Y_{\mathrm{He}} &= 0.261 \pm 0.016.
\end{aligned}
$$

Adding the ground-based CMB measurements of the damping tail to the *Planck* bandpowers pushes along the $N_{\mathrm{eff}}/Y_{\mathrm{He}}$ degeneracy towards higher values of Y_{He}, and lower values of N_{eff}. However, we hesitate to over-interpret this as the $2\,\sigma$ parameter ellipses still contain the ΛCDM values and, as mentioned above, the quality of the fit does not substantially improve.

TABLE 7.5: Parameter constraints for the CMBext dataset

	ΛCDM	ΛCDM+$n_{\rm run}$	ΛCDM+$N_{\rm eff}$	ΛCDM +$Y_{\rm He}$	ΛCDM+$Y_{\rm He}$+$N_{\rm eff}$
$\boldsymbol{\Omega_b h^2}$	0.02232 ± 0.00014	0.02236 ± 0.00013	0.02220 ± 0.00021	0.02232 ± 0.00019	0.02222 ± 0.00021
$\boldsymbol{\Omega_c h^2}$	0.1199 ± 0.0011	0.1200 ± 0.0011	0.1181 ± 0.0025	0.1199 ± 0.0012	0.1151 ± 0.0044
$\boldsymbol{100\theta_{MC}}$	1.04100 ± 0.00029	1.04103 ± 0.00029	1.04122 ± 0.00040	1.04109 ± 0.00051	1.0424 ± 0.0011
$\boldsymbol{\tau}$	0.0522 ± 0.0067	0.0524 ± 0.0077	0.0509 ± 0.0069	0.0516 ± 0.0076	0.0500 ± 0.0068
$\boldsymbol{\ln(10^{10} A_s)}$	3.040 ± 0.014	3.043 ± 0.015	3.032 ± 0.017	3.040 ± 0.015	3.027 ± 0.015
$\boldsymbol{n_s}$	0.9645 ± 0.0039	0.9634 ± 0.0040	0.9587 ± 0.0081	0.9657 ± 0.0069	0.9583 ± 0.0081
$\boldsymbol{n_{\rm run}}$	-	-0.0065 ± 0.0064	-	-	-
$\boldsymbol{N_{\rm eff}}$	-	-	2.90 ± 0.17	-	2.70 ± 0.26
$\boldsymbol{Y_{\rm He}}$	-	-	-	0.246 ± 0.012	0.261 ± 0.016
$\boldsymbol{H_0}$ (km s^{-1} Mpc^{-1})	67.39 ± 0.49	67.45 ± 0.51	66.4 ± 1.3	67.46 ± 0.59	65.3 ± 1.6

The median parameter values and 68% confidence intervals with the CMBext dataset for the ΛCDM model as well as the four extensions to the ΛCDM model considered in this work. In the last row, we also show the constraints on a derived parameter, the Hubble constant H_0, that has received attention recently due to tensions in the preferred value between different experiments.

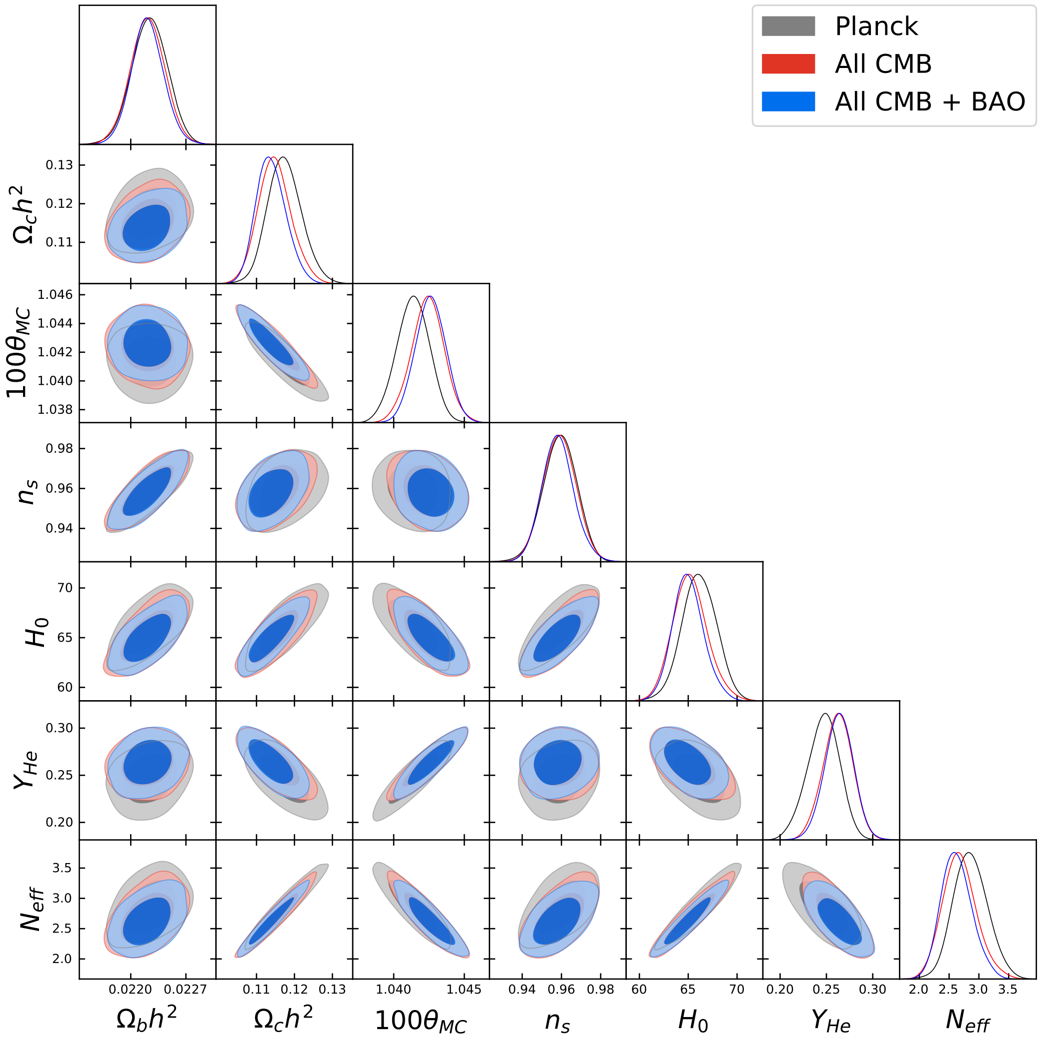

FIGURE 7.6: Parameter posteriors for the ΛCDM+$Y_{\rm He}$+$N_{\rm eff}$ model. We have excluded the optical depth τ and amplitude of scalar perturbations A_s to reduce the complexity of the figure as these two parameters show little change between the datasets.

TABLE 7.6: Parameter constraints for ΛCDM + Y_{He} + N_{eff}

	Planck	CMBall	CMBext
$\boldsymbol{\Omega_b h^2}$	0.02224 ± 0.00023	0.02221 ± 0.00022	0.02222 ± 0.00021
$\boldsymbol{\Omega_c h^2}$	$0.1174^{+0.0041}_{-0.0047}$	$0.1148^{+0.0039}_{-0.0046}$	0.1151 ± 0.0044
$\boldsymbol{100\theta_{MC}}$	1.0414 ± 0.0012	1.0424 ± 0.0012	1.0424 ± 0.0011
$\boldsymbol{\tau}$	0.0536 ± 0.0079	0.0514 ± 0.0080	0.0500 ± 0.0068
$\boldsymbol{N_{eff}}$	$2.86^{+0.27}_{-0.30}$	$2.68^{+0.26}_{-0.30}$	2.70 ± 0.26
$\boldsymbol{Y_{He}}$	$0.247^{+0.018}_{-0.016}$	0.262 ± 0.016	0.261 ± 0.016
$\boldsymbol{\ln(10^{10} A_s)}$	3.037 ± 0.019	3.032 ± 0.019	3.027 ± 0.015
$\boldsymbol{n_s}$	0.9593 ± 0.0085	0.9590 ± 0.0084	0.9583 ± 0.0081

Values of 6 parameters 68% limits from the constraint of ΛCDM $+Y_{He}+$ N_{Eff} with 3 combinations of datasets.

Chapter 8

Conclusion and outlook

The cosmic microwave background has provided an incredible wealth of information for the field of cosmology. Observations of the CMB show excellent evidences for the standard model of the universe at large, including the geometry and early universe matter compositions. Recent and future CMB experiments aim to further test the ΛCDM model and hope to unveil signs of physics beyond the standard ΛCDM model. In this thesis, I continue this effort by constraining cosmological models using data from the POLARBEAR experiment in combination with other CMB and BAO datasets. In this final chapter, I will summarise the prerequisite understandings and data processing, the main results of the data analysis, and give an outlook on CMB measurements.

8.1 Review of prerequisites

I have started with revision of the Standard Model of Cosmology in Chapter 1. In the Standard Model of Cosmology, the first evidence of an expanding universe comes from the Hubble observation and appears in line with our quest for a framework with which we can attempt to describe the universe. For that, I have briefly reviewed general relativity theory along with Einstein's equations, which are foundations for derivation of the equation of state of physical species. Einstein's equations and the Friedmann Equations are pathways to describe the geometry and the evolution of the universe through the evolving species in the Standard Model. The current universe appears to be mainly driven by Dark Energy as cosmological constant. I have then introduced the CMB as one of the best sources to learn about the early universe. The inhomogeneities in the CMB have been shown to be sourced by the quantum perturbations during inflation, and the significance of these inhomogeneities are learned through the CMB power spectra. Milestones of CMB measurements have been mentioned, with the CMB temperature spectrum measured at extremely high accuracy. CMB polarisation spectrum measurements are continuously improved, with the E-mode spectrum updated to small angular scales and the B-mode spectrum being in the current spotlight of many experiments. Higher precision in E-mode measurements is expected to shed light on the neutrino sector of the Standard Model and also physics beyond the Stand Model. I have also given a brief review of cosmological parameters that can be constrained using power spectrum information, especially parameters that are relevant to this work.

In Chapter 2, I have introduced the POLARBEAR experiment. I have described the location of the experiment, the optical configuration and the receivers of POLARBEAR telescope. POLARBEAR started observations in 2012, and data used for this thesis were acquired between July 2014 and December 2016. These data include main CMB science scans of a large patch of the sky in the southern hemisphere, and calibration scans of astrophysical sources and insitu thermal sources. The scan strategy of POLARBEAR is optimised with respect to the location of site, the availability of the observation patches of sky, and the maintenance of the telescope and readout.

In Chapter 3, I have briefly described the function of the continuously rotating half wave plate installed at the prime focus of POLARBEAR telescope for observations of a larger patch of the sky. The main purpose of this HWP is to mitigate low frequency noise coming from atmosphere and ground pickup. I have given the data model under the impact of a CRHWP. In simplified cases, the HWP is expected to rotate the polarisation signals of light by 4 times of the HWP rotating frequency while not acting on unpolarised intensity signal and noise. In more complicated situations, the Mueller matrix needs to be employed to describe effects such as the transmission of the mirror or different transmissivities for the polarisations along the HWP birefringent axes and the phase delay between the polarisation components. The simplified data model with HWP can be modified for outstanding cases not involving opticals elements: detector non-linearity, time-constant, and low frequency (1/f) noise. Understanding these cases is important for the construction of the pipeline to estimate systematic effects described in Chapter 6.

In Chapter 4, I have described POLARBEAR data pre-processing stage, which consist of downsampling, demodulation, calibration of pointing, beam, relative gain, and polarisation angle. Downsampling is the first step to downsize data for better housekeeping as well as optimising computational costs in later stages. Demodulation is a required step due to the polarisation signals being modulated by the frequency of the continuously rotating half wave plate. I mainly mention the mathematical operations or filters that are applied on the time-ordered data to separate intensity and polarisation signal as well as to deconvolve the polarisation signals from time constant retardation. Pre-processing calibration is done using data from calibration scans i.e scans that don't target CMB signals from the $670\,\mathrm{deg}^2$ patch of sky. For pointing calibration, an 8 parameter model is established to account for errors from the telescope mechanics or the ambient temperature. We observed over 100 well-categorised point sources across the CMB large patch and achieved sufficiently small RMS fluctuation errors in source locations after getting the best fit pointing model. For beam calibration, we observed Jupiter to get the effect of beam on power spectra across a full multipole range of $\ell = 0 - 3500$. I also use these Jupiter scans in combination with insitu thermal source scans to get the relative gain conversion between digital unit and physical temperature unit for each single observation. To cross check our relative gain calibration, I apply the derived gain factors on the TOD from elevation nod scans to yield the PWV values which are then compared with the PWV values from APEX data to check overall sanity as well as to remove calibration data that may relate to problematic weather. For polarisation angle calibration, the analysis uses performed scans of Tau A (the Crab Nebula). The Tau A angle is stable across the seasons, and all detectors within a pixel pair are consistently orthogonal to each other.

In Chapter 5, I have described the data analysis pipeline used for data from CMB science scans. The pipeline primarily consists of the data selection stage, the mapmaking stage, and the power spectrum calculation stage. In the data selection stage, data are selected with respect to properties of noise in science scan TOD: glitch, detector noise, and map domain noise. This stage has been iterated several times to select optimally clean data. The noise properties are also relevant to the filtering steps in both the TOD processing step and the mapmaking stage. The TOD processing step is done prior to the operations in the mapmaking stage and most of the data selection stage. While TOD pre-processing are also described in the Section of Downsampling and Demodulation in Chapter 4, I have given specific notes on the CMB scan TOD which concern treatments of glitch cuts and storage of polarisation data. The mapmaking stage employs a series of filtering options optimised basing on the noise model in the data selection stage and projects the final clean TOD into flat maps using OLEA projection. I have noted a few difference between this stage for real POLARBEAR data and for simulations. Our two noise configurations can be added into simulated data either in the TOD simulating step (for TOD noise) or in the final simulated maps (for signflip noise). The power spectrum calculation stage is done using the cross spectrum formulation to subtract the bias in single maps. This stage also includes debiasing components: mode mixing matrix, filter transfer function and beam function to correct for power loss due to mode coupling from finite observation sky, filtering, and beam effects. I have also built a band covariance matrix to account for errors in our signal and noise estimation, and this matrix is employed in parameter constraint in Chapter 7.

In Chapter 6, I have described the validation of our established pipeline and our selected data. I first validate our power spectrum calculation pipeline mostly without use of POLARBEAR data. The pseudo spectrum calculation has been checked with respect to different map projections using maps produced with our simulation mapmaking pipeline without involving real data filtering options. The result is the pseudo spectra from 2 map projections are consistent with each other without concerning the debiasing step. The errors from kernel distortion due to map projections are found to be minimal compared to forecasted POLARBEAR error bars. The debiasing step is validated by generating noiseless simulated skies without involving the mapmaking pipeline. The combination of mode coupling matrix and filter transfer function is found to be stable across the debiasing of 160 simulated sky spectra coming from 4 different cosmology models. Only 1 filter transfer function was created for this test and found to introduce insignificant errors regardless of the input cosmology for the simulate sky. Another module to create the filter transfer function has been written, and the two modules are found to yield pose-debiasing errors consistent with each other. The whole power spectrum estimation pipeline is validated with the consistency between noise bandpowers from 2-dimensional PSD noise generations and from the signflip noise configuration.

Validation of selected POLARBEAR data has been done with a suite of 19 null tests where data are split into 2 halves using several criteria. Each 2 halves are used to take a null spectrum which consists only of noise in case there is no bias in signal estimation. I have applied established passing criteria on the null spectra and have found that the all the criteria are safely passed, indicating no problematic data. Before the unveiling of E-mode bandpowers, systematic errors have been estimated for the our chosen bandpower binning. This is done primarily by injecting the systematic effects into the noiseless simulated TOD during the simulated mapmaking production. The biases caused by systematics are taken to be the absolute difference between a reference bias-free spectrum and the spectra with systematics-injected TOD. Pointing miscalibration is found to contribute a major part to the total systematic errors. However, the total systematic errors are estimated for a conservative upper limit and found to be sufficiently below the statistical errors.

8.2 Main results

Chapter 7 marks the main results of this work. I have presented a measurement of the CMB E-mode power spectrum on angular multipoles $500 \leq \ell \leq 3000$ from $670\,\mathrm{deg}^2$ surveyed with the POLARBEAR instrument. E-mode is detected at high significance across the third through the seventh acoustic peaks of the E-mode power spectrum.

No evidence for significant systematic biases is found in the data, and place limits on known systematic terms that are well below the statistical uncertainties. I combine the POLARBEAR E-mode bandpowers with other, recent CMB measurements [16, 15, 6] to explore the current state of CMB cosmological constraints.

Adding the ground-based CMB bandpowers does not reduce the Hubble constant tension between the *Planck* inferred value and direct local measurements (4.3 vs 4.5 σ). I find no significant preference in the data for any of the extensions considered: $N_{\rm eff}$, $Y_{\rm He}$, $n_{\rm run}$, $N_{\rm eff}$+$Y_{\rm He}$.

For the ΛCDM+$n_{\rm run}$ model extension, the running of the spectral index is varied. Adding ground-based CMB datasets and/or BAO datasets slightly reduces both the primordial amplitude and the optical depth by less than 0.5σ. The more evident decrease in the spectral index n_s estimated by the all CMB dataset is correlated to the n_{run} heading further in the negative direction. Since adding BAO data brings the central value of n_s back to the value constrained using *Planck*-only, the damping tail measured by other CMB experiments might be slightly over-estimated, which can be due to miscalibration. The result from this constraint also does not favor inflationary models with large $n_{\rm run}$.

For the ΛCDM+$Y_{\rm He}$ model extension, adding the ground-based CMB power spectrum measurements brings the Helium abundance towards the BBN expectation of 0.2467. With *Planck*-only, the data prefer 0.239 ± 0.013, shifting to 0.246 ± 0.012 when the other power spectrum measurements are added. As expected, the non-CMB-power-spectrum data does little for $Y_{\rm He}$.

I also look at varying the effective number of relativistic species, $N_{\rm eff}$. I find only minor improvements and shifts from adding data beyond the *Planck* bandpowers. For the combined CMBext dataset, the data favor 2.90 ± 0.17 which is within 1 σ of the expected value of 3.046. The slight decrease of the central values of $N_{\rm eff}$ across subsequent adding of datasets is consistent with the slight decrease in the optical depth central values due to that both decrements mean the acoustic peaks in the damping tail are less 'damped'.

Finally, I allow both $Y_{\rm He}$ and $N_{\rm eff}$ to vary to study the degeneracies between the two. Here, the full CMB dataset slightly pulls $Y_{\rm He}$ upwards and $N_{\rm eff}$ downwards relative to the *Planck*constraints and expected values. For all CMB data combined with BAO data, I find $N_{\rm eff} = 2.70 \pm 0.26$ and $Y_{\rm He} = 0.261 \pm 0.016$. However, the actual improvement in the quality of fit from adding these two parameters is small ($\Delta\chi^2 = 1.2$) suggesting that these shifts are not significant. Overall, some parameters see mixed changes to standard errors of the fitting with additional datasets or extended models. One of those parameters is the angular size of sound horizon at scattering, for which some shifts in the central values are observed across models and data combinations while the standard deviation for this parameter does not see any specific improvements. This is expected because the low multipole range data should be more sensitive to this parameter than the high multipole range data i.e the included additional datasets are.

8.3 Outlook

While the POLARBEAR survey has finished, its successor, the Simons Array, had first light in 2019. The complete Simons Array will have 3 telescopes with a total of 15 times more detectors than POLARBEAR and will survey a large fraction of the Southern sky [122, 123]. The E-mode power spectrum measurement from the Simons Array survey will dramatically improve upon current E-mode constraints and enable new tests of cosmology such as probes of alternate theories of gravity on large scales through constraints of $N_{\rm eff}$ and the sum of neutrino masses [124].

Due to the effect of the density of helium present at the time of recombination on the damping tail of the CMB, a significantly improved E-mode measurement by the Simons Array is expected to shed light on the degeneracy between $Y_{\rm He}$ and N_{eff}. Constraints on N_{eff} are forecasted to improve by order of magnitude from the current best constraints. Measurement of $Y_{\rm He}$ should also be advanced from the best astrophysical measurements at present. Distinguishably, measuring $Y_{\rm He}$ using CMB observations is relatively free from astrophysical systematics which contribute majorly to current error bars. The systematics can be the bias due to extragalactic sources in temperature-based CMB lensing estimates [124]. With leaping improvements in measurements of $Y_{\rm He}$ and N_{eff}, the Simons Array will give high precision estimations of the baryon-to-photon ratio and the expansion rate, which are essential to our knowledge of the early Universe. High precision constraints of the primordial helium means a promising probe of the neutrino sector and, in general, physics beyond the Standard Model.

The Simons Array Survey is expected to be sensitive to the relation between $N_{\rm eff}$ and the total neutrino mass $\sum m_\nu$. Any deviation in constraints of $N_{\rm eff}$, known as ΔN_{eff}, can be relevant to the time of mass generation for neutrinos or different neutrino decay mechanisms. A case of $\Delta N_{eff} = 0$ might need an inventive explanation for the dilution of the neutrinos to cancel out the additional dark energy.

The nature of dark matter (DM) is certainly an outstanding target of the Simons Array. High precision measurements of the E-mode power spectrum by the Simons Array should help inspect different mechanisms of DM annihilation and other models of DM interaction. With its improved sensitivity and sky coverage, the Simons Array will place the bounds on DM annihilation at least better by a factor of 2. Many non-standard DM interactions, Axions and axion-like particles can be ruled out with improved measurements of CMB spectra. In addition, the Simons Array will be capable of probing from the energy scale of inflation, the tensor modes, to axion isocurvature [124].

The Simons Array will also be capable of distinguishing different models of dark energy with exponentially improved measurement of the CMB power spectrum and lensing of the CMB. These measurements can yield predictions of the contents of the cluster and kinetic SunyaevZel'dovich (kSZ) observables when considered with dark energy models. The Simons Array can target the cluster and kSZ observables independently or through cross-correlation with other dark energy probes. The yielded predictions are essential to inspection of dark matter parameters and models. Violations of these predictions would mean the paradigms of these parameters and models need modifications. Verification of these predictions would be another milestone in the quest of the physics of dark energy [124].

Bibliography

[1] E. Hubble. A relation between distance and radial velocity among extragalactic nebulae. *Proceedings of the National Academy of Science*, 15:168–173, Mar. 1929.

[2] M. Colless et al. URL http://www.2dfgrs.net/Public/Pics/2dFzcone_big.jpg.

[3] D. Baumann. Tasi lectures on inflation. *arXiv preprint*, arXiv:0907.5424, 2009.

[4] N. Ponthieu. The cmb, its polarisation, et al, 2011. URL http://ipag.osug.fr/IMG/pdf/ponthieu_IPAG_111201_v2.pdf.

[5] C. Bischoff. URL https://www.cfa.harvard.edu/~cbischoff/cmb/.

[6] J. W. Henning, J.T. Sayre, C. L. Reichardt, P. A. R. Ade, A. J. Anderson, J. E. Austermann, J. A. Beall, A. N. Bender, B. A. Benson, and L. E. Bleem. Measurements of the temperature and e-mode polarization of the cmb from 500 square degrees of sptpol data. *The Astrophysical Journal*, 852:97, Jan 2018.

[7] Z. D. Kermish, P. Ade, A. Anthony, and K. Arnold et al. The polarbear experiment. *In SPIE Astronomical Telescopes+Instrumentation*, 8452 of Society of PhotoOptical Instrumentation Engineers (SPIE) Conference Series:84521C–84521C, Sep. 2012.

[8] D. J. Benford, C. A. Allen, A. S. Kutyrev, S. H. Mosely, R. A. Shafer, J. A. Chervenak, E. Grossman, K. D. Irwin, J. M. Martinis, and C. D. Reintsema. Superconducting transition edge sensor bolometer arrays for submillimeter astronomy. 2000.

[9] D. J. Schlegel, D. P. Finkbeiner, and M. Davis. Maps of dust infrared emission for use in estimation of reddening and cosmic microwave background radiation foregrounds. *The Astrophysical Journal*, 500:525–553, June 1998.

[10] Z. D. Kermish. *The POLARBEAR Experiment: Design and Characterization.* PhD thesis, University of California, Berkeley, 2012.

[11] B. Steinbach. *Measurement of the B-mode power spectrum with POLARBEAR.* PhD thesis, University of California, Berkeley, 2014.

[12] J. R. Pardo, J. Cernicharo, and E. Serabyn. Atmospheric transmission at microwaves (atm): an improved model for millimeter/submillimeter applications. *IEEE Transactions on Antennas and Propagation*, 49(12):1683–1694, Dec 2001.

[13] J. Aumont, L. Conversi, C. Thum, H. Wiesemeyer, E. Falgarone, J. F. Macías-Pérez, F. Piacentini, E. Pointecouteau, N. Ponthieu, and J. L. Puget et al. Measurement of the crab nebula polarization at 90 ghz as a calibrator for cmb experiments. *Astronomy & Astrophysics*, 514:A70, 2010.

[14] Planck Collaboration. Planck 2015 results. xiii. cosmological parameters. *Astronomy & Astrophysics*, 594:A13, June 2016.

[15] Planck Collaboration et al. Planck 2018 results. v. cmb power spectra and likelihoods. *Astronomy & Astrophysics*, July 2019.

[16] ACT Collaboration et al. The atacama cosmology telescope: two-season actpol spectra and parameters. *Journal of Cosmology and Astro-Particle Physics*, 2017 (6):031, June 2017.

[17] BICEP2 Collaboration and Keck Array Collaboration et al. Constraints on primordial gravitational waves using planck, wmap, and new bicep2/keck observations through the 2015 season. *Physical review letters*, 121(22):221301, Nov. 2018.

[18] A. Einstein. Die feldgleichungen der gravitation. *Sitzungsberichte der Koniglich Preussischen Akademie der Wissenschaften (Berlin)*, pages 844–847, 1915.

[19] A. Friedmann. On the curvature of space. *General Relativity and Gravitation*, 31: 1991, Dec 1999.

[20] P.P. Coles and F. Lucchin. *Cosmology: The Origin and Evolution of Cosmic Structure*. Number ISBN 9780470852996. Wiley, 2003. URL https://books.google.fr/books?id=BGYcivB1EtMC.

[21] G. Gamow. The evolution of the universe. *Nature*, 162:680–682, Oct. 1948.

[22] R. A. Alpher and R. Herman. Evolution of the universe. *Nature*, 162:774–775, Nov. 1948.

[23] A. G. Doroshkevich and I. D. Novikov. Mean density of radiation in the metagalaxy and certain problems in relativistic cosmology. *Soviet Physics Doklady*, 9(1991): 680–682, Aug. 1964.

[24] A. A. Penzias and R. W. Wilson. A measurement of excess antenna temperature at 4080 mc/x. *The Astrophysical Journal*, 142:419–421, July 1965.

[25] G. F. Smoot, C. L. Bennett, A. Kogut, and E. L. Wright et al. Structure in the cobe differential microwave radiometer first-year maps. *The Astrophysical Journal Letters*, 396:L1–L5, Sep. 1992.

[26] J. C. Mather, E. S. Cheng, D. A. Cottingham, and R. E. Eplee et al. Measurement of the cosmic microwave background spectrum by the cobe firas instrument. *The Astrophysical Journal*, 420:439–444, Jan. 1994.

[27] D. J. Fixsen, E. S. Cheng, J. M. Gales, J. C. Mather, R. A. Shafer, and E. L. Wright. The cosmic microwave background spectrum from the full cobe firas data set. *The Astrophysical Journal*, 473:576, Dec. 1996.

[28] R. H. Dicke, P. J. E. Peebles, P. G. Roll, and D. T. Wilkinson. Cosmic black-body radiation. *The Astrophysical Journal*, 142:414–419, July 1965.

[29] R. K. Sachs and A. M. Wolfe. Perturbations of a cosmological model and angular variations of the microwave background. *The Astrophysical Journal*, 147, Jan. 1967.

[30] S. Dodelson. *Modern cosmology.* 2003.

[31] Daniel Baumann. Tasi lectures on primordial cosmology, 2018.

[32] Wayne Hu. *Wandering in the Background: A CMB Explorer.* PhD thesis, University of California, Berkeley, 1995.

[33] J. A. Peacock. *Cosmological Physics.* Number ISBN 052141072X. Cambridge, Jan 1999.

[34] S. Bashinsky and E. Bertschinger. Dynamics of cosmological perturbations in position space. *Physical Review D*, 65:123008, Jun. 2002.

[35] C.P. Ma and E. Bertschinger. Cosmological perturbation theory in the synchronous and conformal newtonian gauges. *The Astrophysical Journal*, 455:7, Dec. 1995.

[36] U. Seljak and M. Zaldarriaga. A line-of-sight integration approach to cosmic microwave background anisotropies. *The Astrophysical Journal*, 469:437, Oct. 1996.

[37] C.L. Bennett, D. Larson, J.L. Weiland, N. Jarosik, G. Hinshaw, N. Odegard, K.M. Smith, R.S. Hill, B. Gold, and M Halpern et al. Nine-year wilkinson microwave anisotropy probe (wmap) observations: final maps and results. *The Astrophysical Journal Supplement Series*, 208(2):20, Oct. 2013.

[38] I Planck Collaboration. Planck 2013 results. i. overview of products and scientific results. *Astronomy & Astrophysics*, 571:A1, Oct. 2014.

[39] P. de Bernardis, P. A. R. Ade, J. J. Bock, and J. R. Bond. A flat universe from high-resolution maps of the cosmic microwave background radiation. *Nature*, 404: 955–959, Oct. 2000.

[40] S. Hanany, P. Ade, A. Balbi, J. Bock, J. Borrill, A. Boscaleri, P. De Bernardis, P. G. Ferreira, V. V. Hristov, and A. H. Jaffe et al. Maxima-1: a measurement of the cosmic microwave background anisotropy on angular scales of 10' -5. *The Astrophysical Journal Letters*, 545(1):L5, Oct. 2000.

[41] Planck Collaboration. Planck 2013 results. xvi. cosmological parameters. *Astronomy & Astrophysics*, 571(A16), Oct. 2014.

[42] G. G. Stokes. Ueber die veranderung der brechbarkeit des lichts. *The Astrophysical Journal Letters*, 163:480–490, 1852.

[43] A. Kosowsky. Cosmic microwave background polarization. *Annals of Physics (New York)*, 246(1), Oct. 1996.

[44] J. M. Kovac, E. M. Leitch, C. Pryke, J. E. Carlstrom, N. W. Halverson, and W. L. Holzapfel. Detection of polarization in the cosmic microwave background using dasi. *Nature*, 420:772–787, Dec. 2002.

[45] M. Zaldarriaga and U. Seljak. Gravitational lensing effect on cosmic microwave background polarization. *Physical Review D*, 58:023003, July 1998.

[46] W. Hu and T. Okamoto. Mass reconstruction with cosmic microwave background polarization. *The Astrophysical Journal*, 574:566–574, Aug. 2002.

[47] P. A. R. Ade, R. W. Aikin, and D. Barkats et al. Bicep2-i: Detection of b-mode polarization at degree angular scales. *ArXiv e-prints*, Mar. 2014.

[48] P. A. R. Ade, N. Aghanim, Z. Ahmed, and R.W. Aikin. Joint analysis of bicep 2/keck array and planck data. *Physical review letters*, 114(10):101301, Oct. 2015.

[49] J. H. P. Wu, J. Zuntz, M. E. Abroe, and P. A. R. Ade et al. Maxipol: Data analysis and results. *The Astrophysical Journal*, 665(1), 2007.

[50] Z. Hou, R. Keisler, L. Knox, M. Millea, and C. Reichardt. How massless neutrinos affect the cosmic microwave background damping tail. *Physical Review D 87*, 87: 083008, Apr. 2011.

[51] K. M. Smith, A. Cooray, and S. Das et al. Gravitational lensing. *AIP Conference Proceedings*, 1141:121, 2009.

[52] D. N. Limber. The analysis of counts of the extragalactic nebulae in terms of a fluctuating density field. *The Astrophysical Journal*, 117:134, 1953.

[53] K. M. Smith, O. Zahn, and O. Doré et al. Detection of gravitational lensing in the cosmic microwave background. *Physical Review D*, 76:043510, 2007.

[54] C. M. Hirata, S. Ho, N. Padmanabhan, U. Seljak, and N.A. Bahcall. Correlation of cmb with large-scale structure. ii. weak lensing. *Physical Review D*, 78:043520, Sep. 2008.

[55] C. Feng, G. Aslanyan, and A. V. Manohar et al. The evolution of the universe. *Physical Review D*, 86:063519, Sep. 2012.

[56] L. E. Bleem, A. van Engelen, and G. P. Holder et al. A measurement of the correlation of garlaxy surveys with cmb lensing convergence maps from the south pole telescope. *The Astrophysical Journal Letter*, 753:L9, 2012.

[57] S. Das, T. Louis, and M. R. Nolta et al. The atacama cosmology telescope: temperature and gravitational lensing power spectrum measurements from three seasons of data. *Journal of Cosmology and Astroparticle Physics*, 4:14, Feb. 2013.

[58] A. van Engelen, R. Keisler, and O. Zahn et al. A measurement of gravitational lensing of the microwave background using south pole telescope data. *The Astrophysical Journal*, 756:142, Feb. 2012.

[59] F. Bianchini, P. Bielewicz, A. Lapi, J. González-Nuevo, C. Baccigalupi, G. de Zotti, L Danese, N. Bourne, A. Cooray, and L. Dunne et al. Cross-correlation between the cmb lensing potential measured by planck and high-z sub-mm galaxies detected by the herschel-atlas survey. *The Astrophysical Journal*, 802:64, 2014.

[60] D. J. H. Chung, G. Shiu, and M. Trodden. Running of the scalar spectral index from inflationary models. *Physical Review D*, 68(6), Sep 2003. ISSN 1089-4918.

[61] B. Wallisch. *Cosmological Probes of Light Relics.* PhD thesis, University of Cambridge, 2018.

[62] A. Lewis and A. Challinor. Weak gravitational lensing of the cmb. *Physics Reports*, 429, 2006.

[63] J. Carron, A. Lewis, and A. Challinor. Internal delensing of planck cmb temperature and polarization. *Journal of Cosmology and Astroparticle Physics*, 035, May 2017.

[64] B. Follin, L. Knox, M. Millea, and Z. Pan. First detection of the acoustic oscillation phase shift expected from the cosmic neutrino background. *Physical review letters*, 115:091301, Aug. 2015.

[65] G. Mangano, G. Miele, S. Pastor, T. Pinto, O. Pisanti, and P. Serpico. Relic neutrino decoupling including flavour oscillations. *Nuclear Physics B*, 729:221–234, 2005.

[66] S. Bashinsky and U. Seljak. Neutrino perturbations in cmb anisotropy and matter clustering. *Physical Review D*, 69:083002, 2004.

[67] The ALMA organisation. Atmosphere model. URL https://almascience.nrao.edu/about-alma/atmosphere-model.

[68] Y. Mizugutchi, M. Akagawa, and H. Yokoi. Offset dual reflector antenna. *in Antennas and Propagation Society International Symposium*, 14:2–5, 1976.

[69] C. Dragone. Offset multireflector antennas with perfect pattern symmetry and polarization discrimination. *Bell System Technical Journal*, 57(7):2663–2684, 1978.

[70] H. Tran, A. Lee, S. Hanany, M. Milligan, and T. Renbarger. Comparison of the crossed and the gregorian mizuguchi-dragone for wide-field millimeterwave astronomy. *Applied Optics*, 47:103–109, Jan. 2008.

[71] J. Zmuidzinas. Thermal noise and correlations in photon detection. *Applied Optics*, 42:4989–5008, Oct. 2003.

[72] P. A. R. Ade, G. Pisano, C. Tucker, and S. Weaver. A review of metal mesh filters. *in Proceedings of SPIE*, 6275, 2006.

[73] K. Arnold, P. A. R. Ade, A. E. Anthony, and D. Barron et al. The bolometric focal plane array of the polarbear cmb experiment. *in Society of Photo-Optical Instrumentation Engineers (SPIE) Conference Series*, 8452 of Society of Photo-Optical Instrumentation Engineers (SPIE) Conference Series, Sep. 2012.

[74] J. A. Chervenak, K. D. Irwin, E. N. Grossman, J. M. Martinis, and C. D. Reintsema. Superconducting multiplexer for arrays of transition edge sensors. *Applied Physics Letters*, page 4043, 1999.

[75] G. Smecher, F. Aubin, E. Bissonnette, M. Dobbs, P. Hyland, and K. MacDermid. Biasing and demodulation firmware for kilopixel tes bolometer arrays. *ArXiv e-prints*, Aug. 2010.

[76] S. Takakura et al. Performance of a continuously rotating half-wave plate on the polarbear telescope. *Journal of Cosmology and Astroparticle Physics*, 2017:008, May 2017.

[77] H. B. Callen and T. A. Welton. Performance of a continuously rotating half-wave plate on the polarbear telescope. *Physical Review*, 83:34–40, 1951.

[78] S. Takakura. *Characterization of a continuous polarization modulator using a half-wave plate for measurements of degree-scale cosmic microwave background with the POLARBEAR experiment.* PhD thesis, Osaka University, 2017.

[79] S. A. Bryan, T. E. Montroy, and J. E. Ruhl. Modeling dielectric half-wave plates for cosmic microwave background polarimetry using a mueller matrix formalism. *Applied Optics*, 49(32):6313, Nov 2010. ISSN 1539-4522.

[80] Lay O. P. and N. W. Halverson. The impact of atmospheric fluctuations on degreescale imaging of the cosmic microwave background. *The Astrophysical Journal*, 543:787–798, 2000.

[81] S. Hanany and P. Rosenkranz. Polarization of the atmosphere as a foreground for cosmic microwave background polarization experiments. *New astrophysics Review*, 47:1159–1165, 2003.

[82] S. Takakura et al. Measurements of tropospheric ice clouds with a ground-based cmb polarization experiment, polarbear. *The Astrophysical Journal*, 870(2), Jan. 2019.

[83] J. Errard, P. A. R. Ade, Y. Akiba, K. Arnold, M. Atlas, C. Baccigalupi, D. Barron, D. Boettger, J. Borrill, S. Chapman, and et al. Modeling atmospheric emission for cmb ground-based observations. *The Astrophysical Journal*, 809(1):63, Aug 2015. ISSN 1538-4357.

[84] B. R. Johnson et al. Maxipol: Cosmic microwave background polarimetry using a rotating half-wave plate. *The Astrophysical Journal*, 665:42–54, 2007.

[85] A. Kusaka et al. Modulation of cosmic microwave background polarization with a warm rapidly rotating half-wave plate on the atacama b-mode search instrument. *Review of Scientific Instruments*, 85:024501, 2014.

[86] The POLARBEAR Collaboration et al. A measurement of the cosmic microwave background b-mode polarization power spectrum at sub-degree scales with polarbear. *The Astrophysical Journal*, 794(2):171, 2014.

[87] S. Adachi, M. A. O. Aguilar Faúndez, and K. Arnold et al. A measurement of the degree-scale CMB b-mode angular power spectrum with polarbear. *The Astrophysical Journal*, 897(1):55, jul 2020.

[88] J. M. Wrobel, A. R. Patnaik, I. W. A. Browne, and P. N. Wilkinson. A catalog of 2118 compact radio sources in the northern sky. *Bulletin of the American Astronomical Society*, 30:1308, 1998.

[89] T. Murphy, E. M. Sadler, R. D. Ekers, M. Massardi, P. J. Hancock, E. Mahony, R. Ricci, S. Burke-Spolaor, M. Calabretta, and R. Chhetri et al. The australia telescope 20 ghz survey: the source catalogue. *Monthly Notices of the Royal Astronomical Society*, 402:24032423, Apr. 2010.

[90] J. G. Mangum. A telescope pointing algorithm for alma. *Rapport technique, ALMA memo*, 366, 2001.

[91] A. B. Goldin, M. S. Kowitt, E. S. Cheng, D. A. Cottingham, D. J. Fixsen, C. A. Inman, S. S. Meyer, J. L. Puchalla, J. E. Ruhl, and R. F. Silverberg. Whole-disk observations of jupiter, saturn, and mars in millimeter/submillimeter bands. *The Astrophysical Journal*, 488(2):L161L164, Oct 1997. ISSN 0004-637X.

[92] J. R. Pardo and M. A. Holdaway. Mma memo 187: Modeling of the submillimeter opacity on chajnantor. URL http://legacy.nrao.edu/alma/memos/html-memos/alma187/memo187.html.

[93] G. C. Jaehnig. *Measuring Cosmic Microwave Background Polarization with POLARBEAR and Simons Array*. PhD thesis, University of Colorado at Boulder, 2018.

[94] A. Finzi and R. A. Wolf. Possible conversion of rotational energy of the neutron star in the crab nebula into energy of relativistic electrons. *The Astrophysical Journal*, 155:L107, 1969.

[95] M. J. Rees and J. E. Gunn. The origin of the magnetic field and relativistic particles in the crab nebula. *Monthly Notices of the Royal Astronomical Society*, 167(1):1–12, Apr. 1974.

[96] J. F. Macias-Perez, F. Mayet, J. Aumont, and F-X Désert. Global spectral energy distribution of the crab nebula in the prospect of the planck satellite polarization calibration. *The Astrophysical Journal*, 711(1):417, 2010.

[97] A. Ritacco, J. F. Macías-Pérez, N. Ponthieu, R. Adam, P. Ade, P. André, J. Aumont, A. Beelen, A. Benoît, A. Bideaud, and et al. Nika 150 ghz polarization observations of the crab nebula and its spectral energy distribution. *Astronomy Astrophysics*, 616:A35, Aug 2018. ISSN 1432-0746.

[98] L. Weiland, N. Odegard, R. S. Hill, E. Wollack, G. Hinshaw, M. R. Greason, N. Jarosik, L. Page, C. L. Bennett, and J. Dunkley et al. Seven-year wilkinson microwave anisotropy probe (wmap) observations: planets and celestial calibration sources. *The Astrophysical Journal Supplement Series*, 192(2):19, 2011.

[99] P. A. R. Ade, N. Aghanim, F. Argüeso, M. Arnaud, M. Ashdown, J. Aumont, C. Baccigalupi, A. J. Banday, R. B. Barreiro, and N. Bartolo et al. Planck 2015 results-xxvi. the second planck catalogue of compact sources. *Astronomy & Astrophysics*, 594:A26, 2016.

[100] A. S. Wilson. The structure of the crab nebula at 2.7 and 5 ghz - i. the observations. *Monthly Notices of the Royal Astronomical Society*, 157(3):229253, May 1972.

[101] B. G. Keating, M. Shimon, and A. P. S. Yadav. Self-calibration of cosmic microwave background polarization experiments. *The Astrophysical Journal*, 762(2): L23, Dec 2012. ISSN 2041-8213.

[102] N. Goeckner-Wald. *A Measurement of the Degree Scale B-mode CMB Angular Power Spectrum from the POLARBEAR Experiment*. PhD thesis, University of California, Berkeley, 2019.

[103] The POLARBEAR Collaboration et al. A measurement of the cosmic microwave back- ground b-mode polarization power spectrum at subdegree scales from two years of polarbear data. *The Astrophysical Journal*, 848(2):121, Oct. 2017.

[104] M. M. Tristram, J. F. Macías-Pérez, C. Renault, and D. Santos. Xspect, estimation of the angular power spectrum by computing cross-power spectra with analytical error bars. *Monthly Notices of the Royal Astronomical Society*, 358:833–842, Apr. 2005.

[105] E. Hivon, K. M. Górski, C. B. Netterfield, B. P. Crill, S. Prunet, and F. Hansen. Master of the cosmic microwave background anisotropy power spectrum: A fast method for statistical analysis of large and complex cosmic microwave background data sets. *The Astrophysical Journal*, 567:2–17, Mar. 2002.

[106] K. M. Gorski, E. Hivon, A. J. Banday, B. D. Wandelt, F. K. Hansen, M. Reinecke, and M. Bartelmann. Healpix – a framework for high resolution discretization, and fast analysis of data distributed on the sphere. *The Astrophysical Journal*, 622(2): 759771, Apr. 2005.

[107] A. Lewis and A. Challinor. Code for anisotropies in the microwave background (camb), 2011. URL https://camb.info/.

[108] C. Bischoff. *Observing the Cosmic Microwave Background Polarization Anisotropy at 40 GHz with QUIET*. PhD thesis, University of Chicago, 2010.

[109] A. Lewis and S. Bridle. Cosmological parameters from cmb and other data: A monte carlo approach. *Physical Review D*, 66(10):103511–+, Nov. 2002.

[110] A. Manzotti, W. Hu, and A. Benoit-Lévy. Super-sample cmb lensing. *Physical Review D*, 90(2):023003, July 2014.

[111] W. Cardona, R. Durrer, M. Kunz, and F. Montanari. Lensing convergence and the neutrino mass scale in galaxy redshift surveys. *Physical Review D*, 94:043007, Mar. 2016.

[112] The SPT Collaboration and K. Story et al. A measurement of the cosmic microwave background damping tail from the 2500-square-degree spt-sz survey. *The Astrophysical Journal*, 779:86, Dec. 2013.

[113] Planck Collaboration et al. Planck 2018 results. viii. gravitational lensing. *Astronomy & Astrophysics*, July 2018.

[114] The SPT collaboration and W. L. K. Wu et al. A measurement of the cosmic microwave background lensing potential and power spectrum from 500 deg$\hat{2}$ of sptpol temperature and polarization data. *The Astrophysical Journal*, 884, May 2019.

[115] A. G. Riess, S. Casertano, W. Yuan, L. M. Macri, and D. Scolnic. Large magellanic cloud cepheid standards provide a 1% foundation for the determination of the hubble constant and stronger evidence for physics beyond Λcdm. *The Astrophysical Journal*, 876:85, May 2019.

[116] The SDSS Collaboration et al. The clustering of galaxies in the completed sdss-iii baryon oscillation spectroscopic survey: cosmological analysis of the dr12 galaxy sample. *Monthly Notices of the Royal Astronomical Society*, 470(3):85, Sep. 2017.

[117] A. J. Ross, L. Samushia, C. Howlett, W. J. Percival, A. Burden, and M. Manera. The clustering of the sdss dr7 main galaxy sample - i. a 4 per cent distance measure at z = 0.15. *Monthly Notices of the Royal Astronomical Society*, 449(1):835–847, May 2015.

[118] F. Beutler, C. Blake, M. Colless, D. H. Jones, L. Staveley-Smith, L. Campbell, Q. Parker, W. Saunders, and F. Watson. The 6df galaxy survey: baryon acoustic oscillations and the local hubble constant. *Monthly Notices of the Royal Astronomical Society*, 416:3017–3032, Oct. 2011.

[119] S. Taubenberger, S. H. Suyu, E. Komatsu, I. Jee, S. Birrer, V. Bonvin, F. Courbin, C. E. Rusu, A. J. Shajib, and K. C. Wong. The hubble constant determined through an inverse distance ladder including quasar time delays and type ia supernovae. *Astronomy & Astrophysics*, 628:L7, July 2019.

[120] J. Bernstein, L. S. Brown, and G. Feinberg. Cosmological helium production simplified. *Rev. Mod. Phys.*, 61:25–39, Jan 1989.

[121] V. Mukhanov. Nucleosynthesis without computer. *International Journal of Theoretical Physics*, 43(3):669693, Mar 2004. ISSN 0020-7748.

[122] A. Suzuki and POLAREBAR Collaboration et al. The POLARBEAR-2 and the Simons Array experiments. *Journal of Low Temperature Physics*, 184:805–810, Aug. 2016.

[123] M. Hasegawa and POLARBEAR Collaboration et al. Polarbear-2: a new cmb polarization receiver system for the simons array. *in Proceedings of SPIE*, 10708, July 2018.

[124] K. Abazajian and CMB-S4 Collaboration et al. Cmb-s4 science book, first edition. *arXiv: 1610.02743*, 2016.